Phase equilibria and permanent magnets in the Ce-Fe-Co-B system

Tian Wang

A Thesis

In the Department

Of

Mechanical, Industrial & Aerospace Engineering

Presented in Partial Fulfillment of the Requirements

For the Degree of

Doctor of Philosophy (Mechanical Engineering) at

Concordia University

Montreal, Quebec, Canada

May 2018

CONCORDIA UNIVERSITY

SCHOOL OF GRADUATE STUDIES

This is to certify that the thesis prepared,

By: **Tian Wang**

Entitled: **Phase equilibria and permanent magnets in the Ce-Fe-Co-B system**

and submitted in partial fulfillment of the requirements for the degree of

Doctor Of Philosophy (Mechanical Engineering)

complies with the regulations of this University and meets the accepted standards with respect to originality and quality.

Signed by the final examining committee:

_____ Chair
Dr. Xiaolei Wang

_____ External Examiner
Dr. Nicole Demarquette

_____ External to Program
Dr. Alex De Visscher

_____ Examiner
Dr. Robin Drew

_____ Examiner
Dr. Paula Wood-Adams

_____ Thesis Supervisor
Dr. Mamoun Medraj

Approved by _____
Dr. Ali Dolatabadi, Graduate Program Director

August, 29th, 2018
Date of Defence

_____
Dr. Amir Asif, Dean, Faculty of Engineering and Computer Science

Abstract

Phase equilibria and permanent magnets in the Ce-Fe-Co-B system

Tian Wang, Ph.D.

Concordia University, 2018

Ce-Fe-Co-B is a promising system for permanent magnets. A high-throughput screening method combining diffusion couples, key alloys, Scanning Electron Microscope/ Wavelength Dispersive X-ray Spectroscope (SEM/WDS), and Magnetic Force Microscope (MFM) is used in this research to understand the phase equilibria and to explore promising magnetic phases in this system. Three magnetic phases are detected and their homogeneity ranges are determined at 900°C, which are presented by the formulae: $Ce_2Fe_{14-x}Co_xB$ ($0\leq x\leq 4.76$), $CeCo_{4-x}Fe_xB$ ($0\leq x\leq 3.18$) and $Ce_3Co_{11-x}Fe_xB_4$ ($0\leq x\leq 6.66$). The phase relations among the magnetic phases in this system have been studied. $Ce_2(Fe, Co)_{14}B$ appears to have stronger magnetization than $Ce(Co, Fe)_4B$ and $Ce_3(Co, Fe)_{11}B_4$ based on MFM analysis when comparing the magnetic interactions of selected key alloys. Two non-magnetic compounds have been detected in this system, a Co-rich with $CeCo_{12-x}Fe_xB_6$ ($0\leq x\leq 8.74$) formula; and a B-rich with $Ce_{13}Fe_xCo_yB_{45}$ ($32\leq x\leq 39$, $3\leq y\leq 10$) formula. The crystal structure of this B-rich phase could not be found in the literature and its XRD pattern is extracted in the current study. Moreover, ternary solid solutions ε_1 ($Ce_2Fe_{17-x}Co_x$ ($0\leq x\leq 12.35$)) and ε_2 ($Ce_2Co_{17-x}Fe_x$ ($0\leq x\leq 3.57$)) are found to form between Ce_2Fe_{17} and Ce_2Co_{17} in the Ce-Fe-Co ternary system at 900°C.

The intrinsic magnetic properties of $Ce_2Fe_{14-x}Co_xB$ ($0\leq x\leq 4.76$) are studied at 25°C using key alloys annealed at 900°C for 25 days. The saturation magnetization (M_s) and the Curie temperature (T_c) of $Ce_2Fe_{14-x}Co_xB$ increase with Co content. However, the anisotropy field (H_a) of $Ce_2Fe_{14-x}Co_xB$ diminishes precipitously with Co content. The process of crystal structure refinement indicates that the saturation magnetization of $Ce_2Fe_{14-x}Co_xB$ is related to the site occupancy of Co atoms at different Fe atomic sites. Co atoms prefer to occupy 8*j2* site, followed by 16*k2*, 4*e* and 16*k1* sites sequentially. Moreover, Co atoms occupying 8*j2* site are more effective leading to an increase in the M_s. The individual effects of Ni or Cu on the intrinsic magnetic properties of $Ce_2Fe_{12.98-x}Co_{1.02}Ni_xB$ and $Ce_2Fe_{12.98-y}Co_{1.02}Cu_yB$ are evaluated. The maximum solid solubilities

of Ni and Cu in $Ce_2Fe_{12.98}Co_{1.02}B$ at 900ºC are found to be 8 at.% and 0.8 at.%, respectively. Ni or Cu enhances T_c, but decreases both M_s and H_a of $Ce_2Fe_{12.98}Co_{1.02}B$. This work also discussed the combined effects of Ni and Cu on the intrinsic magnetic properties of $Ce_2Fe_{12.98}Co_{1.02}B$. The M_s of $Ce_2Fe_{12.98-x-y}Co_{1.02}Ni_xCu_yB$ ($0 \leq x \leq 0.41$, $y \approx 0.119$) increases after doping with both Ni and Cu, reaching around 155 emu/g. Meanwhile, the H_a and the T_c are measured to be near 24 kOe and 280°C, respectively.

The domain width and domain wall energy of the $Ce_2Fe_{14-x}Co_xB$ solid solution are studied for the first time in this work. The influence of Co content on these properties has been analyzed with the aid of magnetic force microscopy using diffusion couple and key alloys. The domain widths of $Ce_2Fe_{14-x}Co_xB$ decrease with increasing Co content at about 0.02 μm per 1 at.% Co. In $Ce_2Fe_{14-x}Co_xB$, phase shift, domain width and saturation magnetization are related in a way that lower average domain width is associated with higher phase shift and higher saturation magnetization. The highest domain wall energy of $Ce_2Fe_{14-x}Co_xB$ is measured as 31.7 erg/cm^2 after dissolving 14 at.% Co (x=2.38). The effects of Ni and Cu on the domain width and domain wall energy of $Ce_2Fe_{14-x}Co_xB$ (x=1.02) are also studied and reported using response surfaces. The domain width and domain wall energy of this solid solution increase after doping with 1 at.% Ni at constant Co content of 6 at.%, measuring 1.39 μm for domain width and 33.4 erg/cm^2 for domain wall energy. Both properties are determined as 0.71 μm and 18.6 erg/cm^2, respectively, after doping with 0.8 at.% Cu, while keeping Co content constant at 6 at.%. When $Ce_2Fe_{14-x}Co_xB$ (x=1.02) is doped with both Ni (1 at.%) and Cu (0.8 at.%), the domain width and domain wall energy measured 0.99 μm and 33.8 erg/cm^2, respectively.

Acknowledgements

I would like to express my sincere gratitude and appreciation to my supervisor Dr. Mamoun Medraj for his constant advice, support and encouragement during my study at Concordia University. Without his cooperation and continuous inspiration, it would not be possible to carry out this work.

I would like to recognize Dr. Paula Wood-Adams for giving us the access to AFM/MFM and Ms. Patricia Moraille from Université de Montréal for her AFM/MFM tutorials. I would also like to acknowledge Dr. Dominic Ryan from McGill University and Dr. Maxime Dion from Université de Sherbrooke for their assistances of operating PPMS and discussions about the experimental results; as well as Mr. Heng Wang from Concordia University for his guidance on operating TGA.

Additionally, I am grateful to be part of the TMG group. I would like to thank all former and current TMG members for their continuous support. Especially, Dr. Dmytro Kevorkov, for his support and concise advice throughout my entire doctorate program; Mr. Mazen Samara for his technical support for my research; Mr. Kayode Orimoloye for his friendship and constant help during my research. Special thanks to Dr. Frederick Pinkerton from GM motors for his discussions at the beginning of this project; and the former TMG member Dr. Ahmad Mostafa for his valuable suggestions for my experiments. In addition, financial support from General Motors Canada Ltd. and NSERC through the CRD grant program is gratefully acknowledged.

Last but not least, I would like to extend my warm and sincere thanks to my parents and my wife. I could never have been able to stand at this point of my life without their unconditional love and endless support.

Dedicated with much love and gratitude

to my parents and my wife

感谢你们

Table of Contents

List of Figures

List of Tables

Chapter 1: Introduction

1.1 Background

Permanent magnets retain their magnetism after being magnetized. They are widely used in power, electrical, automotive and mechanical applications. Nowadays, manufacturing of hybrid and electric cars has escalated the demand for strong and low cost permanent magnets [1]. In order to reduce the fossil fuel consumption, electric motors in combination with an internal combustion engine or all electric vehicles are considered as the primary technologies, as alternatives to petrol-guzzling transportation [2].

The development of permanent magnetic materials started around the beginning of 20th century as shown in Figure 1.1 [3]. Since 1930s, the permanent magnet industry has led to the progress of ferrite and Alnico magnets. However, during the last few decades, the development of hard magnetic materials has rapidly progressed with the advent of rare-earth (RE) permanent magnets [3]. Compared to KS (Kichizaemon Sumitomo) steel which was invented in 1916, the maximum energy product $(BH)_{max}$ was improved almost 60 times. Modern permanent magnet devices require the presence of large coercivity (material's resistance to become demagnetized). Most favorable candidates for sufficiently large anisotropy are RE based materials which exhibit considerably higher coercivity and energy product than the traditional Alnico alloys and hard ferrites [1]. Two common RE permanent magnets are from the Sm-Co and Nd-Fe-B systems. Sm-Co permanent magnets were introduced in the 1960s. The compound $SmCo_5$ was found to have suitable magnetic properties with a high Curie temperature (T_c=750°C). The $(BH)_{max}$ of this type of magnet reached 22 MGOe [3]. Another Sm-Co type magnet which has even higher magnetizations was developed based on the Sm_2Co_{17} compound. The Sm_2Co_{17} compound has a higher T_c (820°C) than $SmCo_5$, and the $(BH)_{max}$ was measured up to 32 MGOe with smaller anisotropy field [3]. Due to the comparatively high cost of Sm and Co, researchers focused on finding new Fe-based permanent magnets with similar properties. This eventually led to the joint announcement of the development of magnets based on the body centred tetragonal $Nd_2Fe_{14}B$ [4] by Sagawa *et al.* [6] and Croat *et al.* [5]. $Nd_2Fe_{14}B$ is found to have high coercivity at room temperature with $(BH)_{max}$ greater than 36.2 MGOe [6]. However, the Curie temperature of $Nd_2Fe_{14}B$ is around 310°C, which causes significant drops in magnetic properties as the temperature increases [6]. The Sm-Co magnets have the highest Curie temperature (up to 800°C) among the magnets with RE content [5]. They can maintain good magnetic properties up to a

temperature of 350°C [5, 6] as opposed to 150°C for $Nd_2Fe_{14}B$ [4]. Nevertheless, their very high cost and very low mechanical strength have limited their use in high mass and low cost industries such as the automotive industry.

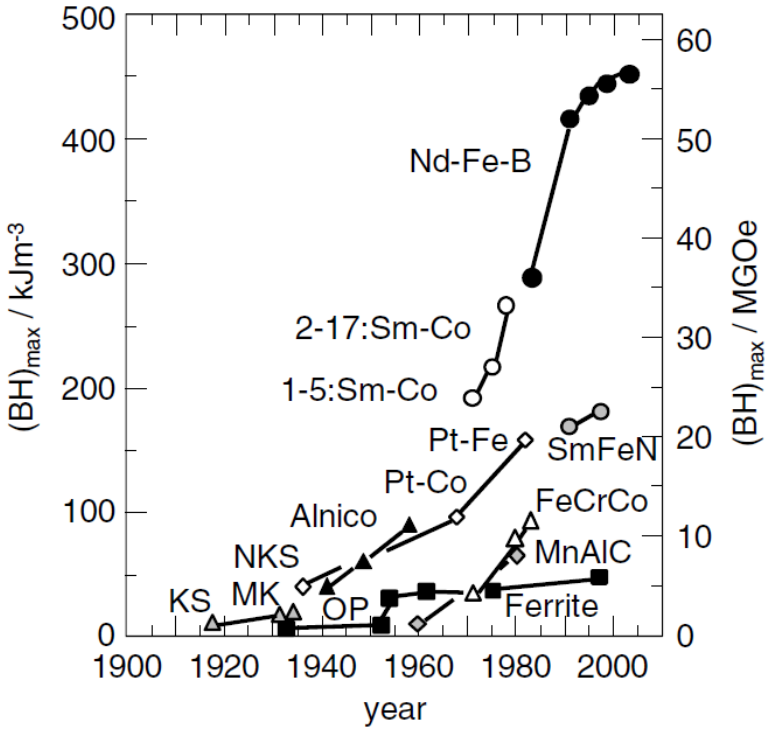

Figure 1.1. Development of permanent magnets [3].

The remarkable increase in motor applications started in 1995, where Nd-Fe-B sintered magnets were used in servo motors, compressor motors, lifting motors, electric power steering (EPS) motors of automobiles and driving motors of hybrid-type automobiles [3]. The limit of 50 MGOe has been passed at room temperature in sintered Nd-Fe-B magnet. However, as mentioned earlier, due to the low Curie temperature of Nd-Fe-B magnets, the upper working temperature of the Nd-Fe-B magnets is limited to around 150°C [4]. Other drawbacks are their higher cost, low mechanical strength and low corrosion resistance [3]. Higher temperature stability of Nd-Fe-B have been achieved by adding Dy and Co [4, 7]. The addition of Dy decreases the $(BH)_{max}$, but increases the coercivity and the thermal stability [7]. Co also improves corrosion resistance of these magnets [4]. The discovery of $Nd_2Fe_{14}B$-based permanent magnets made possible the advent of crucial energy efficient technologies such as wind turbines, hybrid vehicle motors and others. So far, the price considerations are important, as none of the main components (e.g. Sm, Dy and Nd) is particularly inexpensive. From the USGS (United States Geological Survey) scientific

report of 2010 as shown in Figure 1.2 (a), Ce is the most abundant RE element with relatively the lowest price [8]. The price fluctuations of Sm and Dy are much more severe, as can be seen in Figure 1.2 (b). Especially in the case of Dy, its price has climbed sharply over the past few years and reached USD 1000 per kg in 2012. Unlike Nd whose price increases significantly and reached USD 40 per kg in 2016, Ce is twenty times cheaper, with the price of only USD 2 per kg in 2016. The growing global demand for permanent magnets and rising costs of the less abundant RE metals (e.g. Nd, Sm and Dy) necessitates the development of new Fe-based magnets with the addition of relatively abundant RE metals (e.g. Ce).

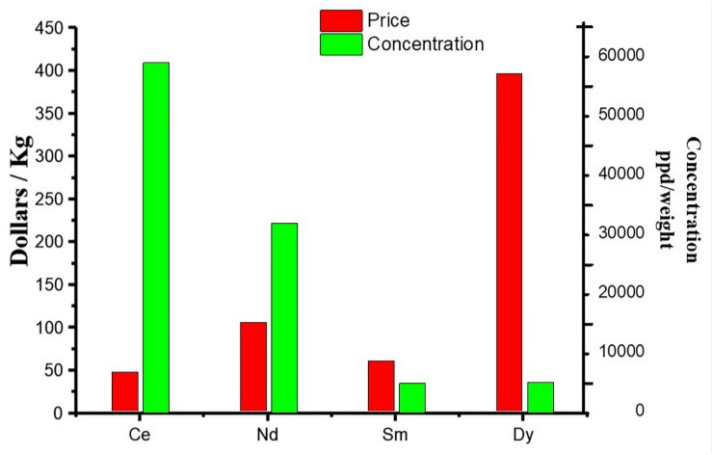

(a)

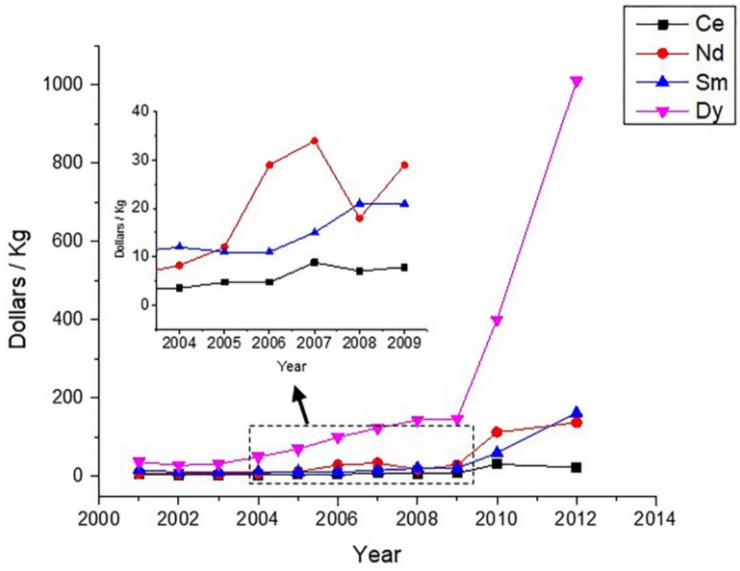

(b)

Figure 1.2. (a) Price of rare earth elements with the concentrations in 2010 [8]; (b) price fluctuations of rare earth elements [8].

Pinkerton and Herbst [9] used melt-spinning for the magnetic hardening of the phases in the Ce-Fe-B system. They found that magnetic properties of 6.2 kOe coercivity (H_c), 4.9 kG remanence (B_r), and 4.1 MGOe maximum energy product $(BH)_{max}$ could be achieved in ribbons comprised principally of $Ce_2Fe_{14}B$. Although $(BH)_{max}$ of $Ce_2Fe_{14}B$ is comparatively inferior to that of $Nd_2Fe_{14}B$ ($(BH)_{max}$ =14 MGOe), it is still sufficient to offer the potential for producing Ce-Fe-B magnets having hard magnet characteristics suitable for less-demanding applications. Currently, ferrite magnets ($(BH)_{max}$ =3 MGOe) are still widely used in the industry [3]. Ce-based magnets could fill the gap between ferrite and Nd-based magnets. The Curie temperature (T_c) of $Ce_2Fe_{14}B$ magnet is 151°C which is lower than that of $Nd_2Fe_{14}B$ (T_c=312°C). Skoug *et al.* [10] pointed out that replacement of Fe by Co could improve the elevated-temperature magnetic properties and significantly increase the Curie temperature of $Ce_2Fe_{14}B$ magnet. Thus, the Ce-Fe-Co-B system is promising for magnetic phases, especially in the Fe-rich corner, with superior to those of ferrite. For example, the M_s should be higher than 80 emu/g which is the M_s value of $CoFe_2O_4$ [111], and the Curie temperature should be high enough to maintain magnetic performance with increasing temperature as well as having low cost for the automotive or electromechanical applications. RE systems of a higher order such as the quaternary system have not been investigated systematically. In many systems, phase equilibria related to the formation of magnetic phases are still uncertain. Besides exploring promising magnetic compounds in the Ce-Fe-Co-B system, understanding their phase relations is another objective of this research.

To introduce a practical hard magnet, three basic steps must be followed [11]. First and foremost is the determination of the intrinsic magnetic properties (saturation magnetization, anisotropy field and Curie temperature) of the material [11]. If the results are promising, the next step is to determine the magnetic structure [11]. This step is important in improving the magnetic properties through elemental substitutions. The last step is the enhancement of the extrinsic magnetic properties, such as remanence and coercivity, through control of the microstructure [11]. However, limited information can be found regarding the intrinsic magnetic properties of magnetic Ce-Fe-Co-B compounds in the literature. Moreover, it is very essential to understand how the magnetic properties change with varied solid solubility. Hence, in this study, intrinsic properties of the promising Ce-Fe-Co-B compounds are determined through the analysis of bulk homogenized alloys.

Ni and Cu were reported to be beneficial to the magnetic properties of the $Nd_2Fe_{14}B$ magnets, in particular for improving the thermal stability [12-14]. However, only limited literature data can be found regarding the effects of these additives on the Ce-Fe-Co-B solid solutions. In order to help developing Ce-containing permanent magnets, this research will attempt to understand the effects of Ni and Cu along with Co on the intrinsic magnetic properties of the Ce-Fe-Co-B solid solutions.

1.2 Research objectives

The main objective of this work is to screen the new Fe-rich magnetic phases in the Ce-Fe-Co-B system and modify their magnetic properties using Ni and Cu. Combined diffusion couple and key alloys techniques is used to investigate the phase relationships in this quaternary system. Scanning Electron Microscope (SEM) coupled with Energy/Wavelength Dispersive X-ray Spectroscopes (EDS/WDS), X-ray Diffraction (XRD) and Magnetic Force Microscope (MFM) are used to identify phase compositions and study the domain structure of the magnetic phases. Thermogravimetric Analyzer (TGA) and Physical Property Measurement System (PPMS) are used to evaluate the intrinsic magnetic properties of magnetic phases. Specific research objectives include:

1. Searching for magnetic phases in the Ce-Fe-Co-B quaternary system.
2. Studying the phase relationships in the Ce-Fe-Co-B system through diffusion couples and key alloys.
3. Identification of the composition of the potential magnetic phases and studying their magnetic domain structure using SEM/EDS/WDS, XRD and MFM.
4. Determination of the intrinsic magnetic properties of the promising magnetic phases using TGA and PPMS.
5. Understanding the effects of additives on the intrinsic magnetic properties of the promising magnetic phases.

Chapter 2: Literature review

2.1 Magnetic properties

Magnetic properties of a permanent magnet are divided into intrinsic properties and extrinsic properties. Intrinsic properties include saturation magnetization (M_s), anisotropy field (H_a) and Curie temperature (T_c). They depend on the crystal structure and the chemical composition [15]. M_s is a measure of the maximum amount of magnetic field that can be generated by a magnetic material. It depends on the strength of the atomic dipole moments and the crystal structure [15]. Magnetocrystalline anisotropy which is denoted as H_a is the energy necessary to deflect the magnetic moment in a single crystal from the easy to the hard axis [15]. It depends on temperature, grain size and crystal shape [15]. T_c is the transition temperature at which magnets lose their magnetism because the alignment of the atomic magnetic moments falls to zero [15]. Above T_c, ferro- or ferrimagnetic material become paramagnetic. Extrinsic magnetic properties depend on processing factors such as heat-treatment and the associated microstructures. When permanent magnets are placed in an applied field opposed to its magnetization, they resist demagnetization over a significant range of field values. The extrinsic properties are quantified by the remanence B_r and coercivity H_c [15].

Certain magnetic properties of ferromagnets can be determined through hysteresis loop measurements. A hysteresis loop represents the variation of the magnetic induction (B) of ferromagnetic materials with an applied magnetic field (H). Figure 2.1 shows a hysteresis loop of ferromagnet [16], with the initial magnetization curve presented by a dotted line.

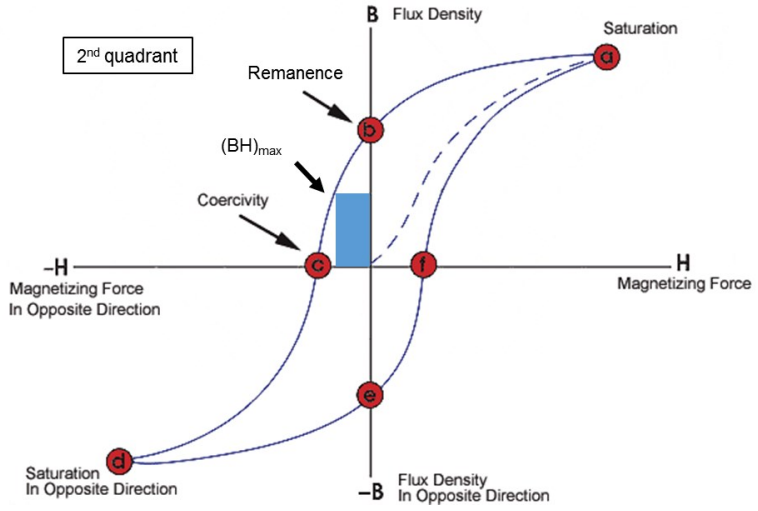

Figure 2.1. A hysteresis curve of ferromagnet, redrawn from [16].

In the figure above, H_c, also known as coercive force, is the demagnetizing field required to reduce the magnetic induction B to zero [17]. For example, magnets used for motors and generators are normally subjected to strong demagnetizing fields, which may lead to demagnetization if the coercivity is not sufficiently high. Maximum energy product $(BH)_{max}$ corresponds to the area of the largest B-H rectangle that can be constructed within the second quadrant of the hysteresis curve [17]. The value of the energy product is representative of the energy required to demagnetize a permanent magnet. The larger $(BH)_{max}$ is, the harder is the material in terms of its magnetic characteristics [17].

Magnetism of an alloy is related to the formation of certain magnetic phases, and is also affected by the precipitates in the alloy. Thus, in order to study the Ce-Fe-Co-B magnets, the phase relationships of the Ce-Fe-Co-B quaternary system must be understood first. Knowledge of phase equilibria is necessary for new magnets development and for the optimization of magnets composition as well as establishing the heat-treatment conditions. In next section, experimental data from available literature on constituent binary and ternary systems are presented. Phase relationships of binary and ternary sub systems are described first, followed by the literature data on the magnetic compounds.

2.2 Binary sub systems

2.2.1 B-Co system

The binary phase diagram of the B-Co system was established by Schobel *et al.* [18]. Liao *et al.* [19] redrew the B-Co phase diagram based on the work of [18] and incorporated solubility data of B in Co reported by Lerner *et al.* [20] as illustrated in Figure 2.2. The B-Co system consists of three intermediate compounds Co_3B, Co_2B and CoB, the terminal solid solutions (α-Co), (ε-Co) and (β-B), as well as the liquid phase L. The solubility limits of the terminal solid solutions are negligible. CoB is a diamagnetic compound, while Co_2B and Co_3B are reported to be soft ferromagnetic compounds with Curie temperature of 429 K and 727 K, respectively [21].

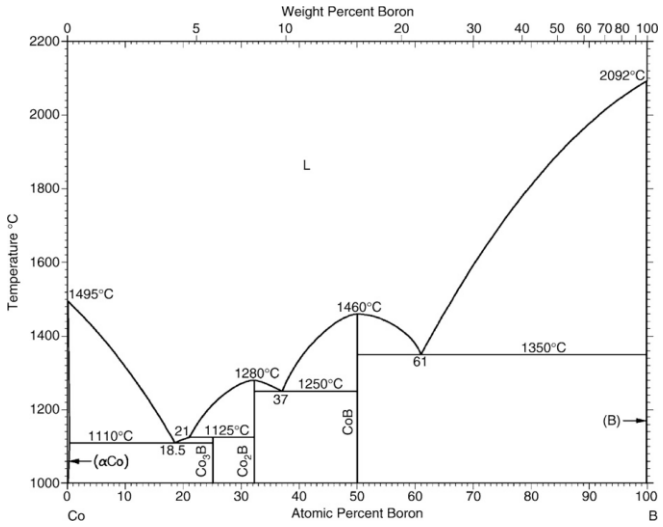

Figure 2.2. B-Co phase diagram [19].

2.2.2 B-Fe system

B-Fe binary system is important for several materials such as Nd-Fe-B magnets [22-23]. Thermodynamic optimization of this system has been performed by several researchers [24-27]. Ohtani *et al.* [26] calculated the Fe-B-C ternary system and considered bcc-Fe and fcc-Fe as interstitial solid solutions. Rompaey *et al.* [27] optimized this binary system, using CALPHAD method as presented in Figure 2.3. Both interstitial and substitutional models have been used for the solid solubility of B in bcc-Fe and fcc-Fe. And thermodynamic calculations based on the two models were in good agreement with experimental results from the literature. The Curie temperature of BFe_2 was reported as 823 K [28]. No literature data can be found regarding the magnetic properties of other B-Fe phases.

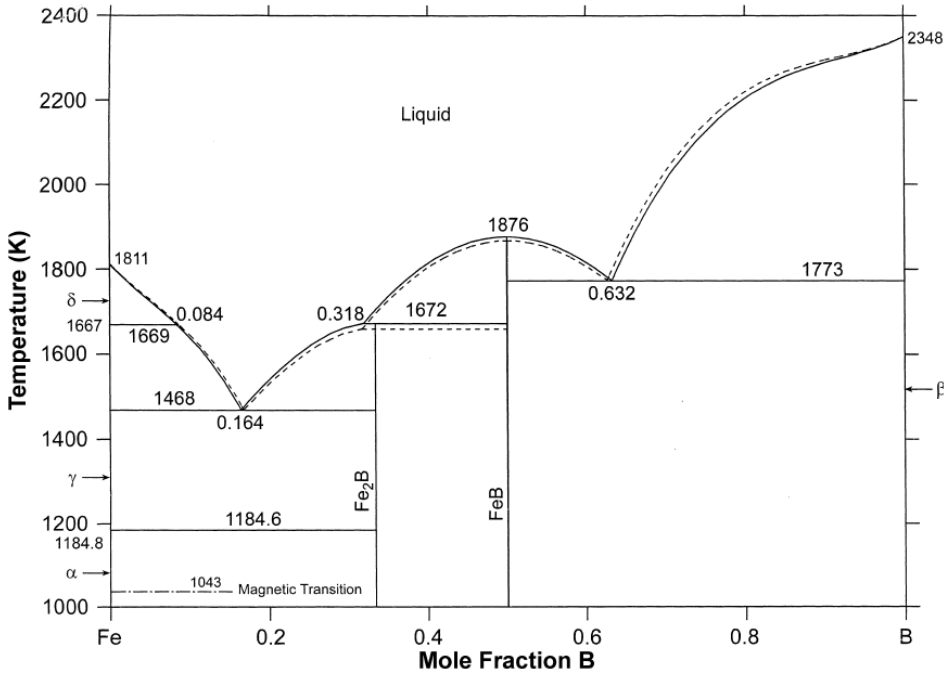

Figure 2.3. Calculated B-Fe phase diagram according to the description of interstitial model (full lines) and substitutional model (dashed line). Numerical values are taken from the interstitial model [27].

2.2.3 B-Ce system

The B-Ce phase diagram reviewed by Liao *et al.* [29] is illustrated in Figure 2.4. This system includes terminal boron phase (β-B), B_4Ce and B_6Ce compounds, three stable cerium polymorphs (β-Ce, γ-Ce and δ-Ce), and limited experimental data for liquidus temperature and composition. Later on, Wang *et al.* [35] thermodynamically reassessed this system considering the experimental results of [29, 31, 32, 34] as shown in Figure 2.5. The calculated phase diagram is in good agreement with most of the experimental data of [29-34]. However, they [35] mistakenly considered the eutectic reaction L↔B_6Ce + β-B as a eutectoid reaction in their thermodynamic model. Based on the calculation of Wang *et al.* [35], the eutectic reaction of L↔ B_6Ce + β-B occurred at 2000°C which is lower than the results of [30]. Yet, their [35] results are consistent with [34]. In addition, the calculated liquidus between the liquid and B_4Ce phase as well as the phase region between the liquid and B_6Ce phase [35] are slightly different from the experimental diagram of [30]. So far, inconsistences from various works indicate that further investigations are needed for this system, especially to confirm the liquidus temperature. More importantly, reports on the magnetic properties of the B-Ce compounds could not be found in the literature.

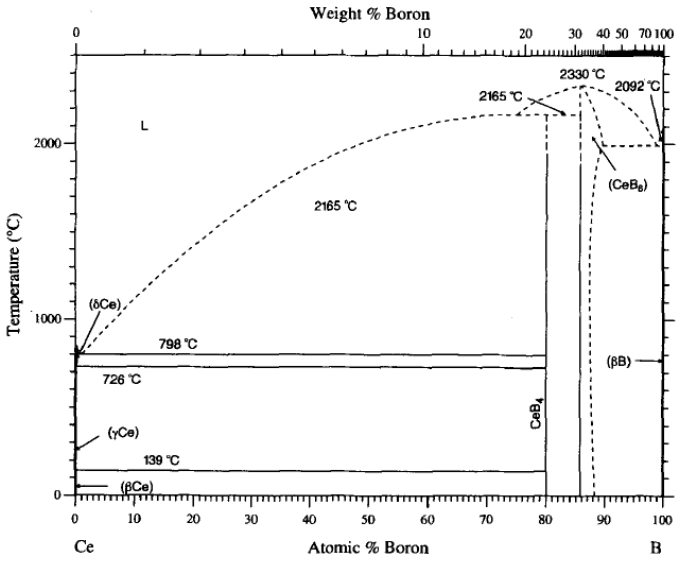

Figure 2.4. B-Ce phase diagram [29].

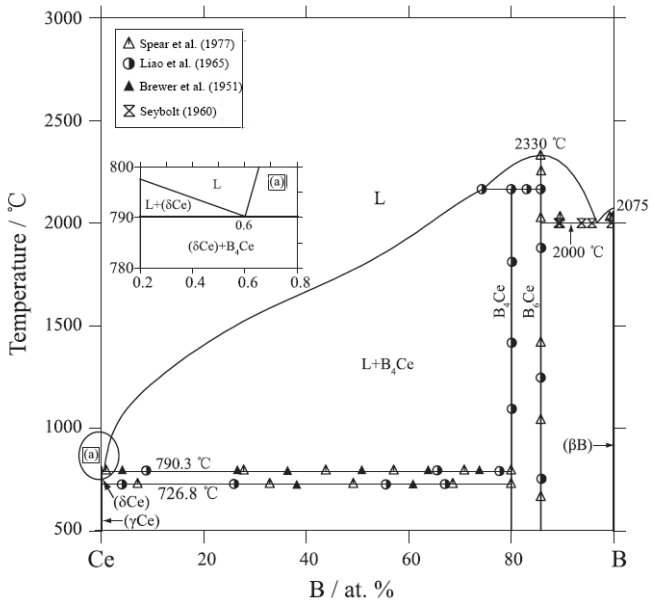

Figure 2.5. Calculated phase diagram of the B-Ce system compared with experimental data from the literature [35].

2.2.4 Ce-Co system

Several efforts [36-41] have been made to calculate the Ce-Co phase diagram. This system contains several intermetallics and their crystal structures are reported by Massalski *et al.* [40] as $Ce_{24}Co_{11}$ ($Ce_{24}Co_{11}$-type hexagonal), $CeCo_2$ (C15, $MgCu_2$-type cubic), $CeCo_3$ (Be_3Nb-type rhombohedral), Ce_2Co_7 (Ce_2Ni_7-type hexagonal), Ce_5Co_{19} (rhombohedral), $CeCo_5$ ($CaCu_5$-type

hexagonal), β-Ce_2Co_{17} ($ThNi_{17}$-type hexagonal), and α-Ce_2Co_{17} (Th_2Zn_{17}-type rhombohedral). Su *et al.* [41] critically assessed and thermodynamically modeled this system. The calculated phase diagram [41] shown in Figure 2.6 is in good agreement with the calculations and experimental results of [37, 39]. The Curie temperatures of Co_2Ce, Co_3Ce, Co_7Ce_2, $Co_{19}Ce_5$, Co_5Ce and $Co_{17}Ce_2$ were reported as 0, 78, 123, 293, 737, 1078 K, respectively by [42]. However, the magnetic orderings of binary Ce-Co compounds could not be found from the literature.

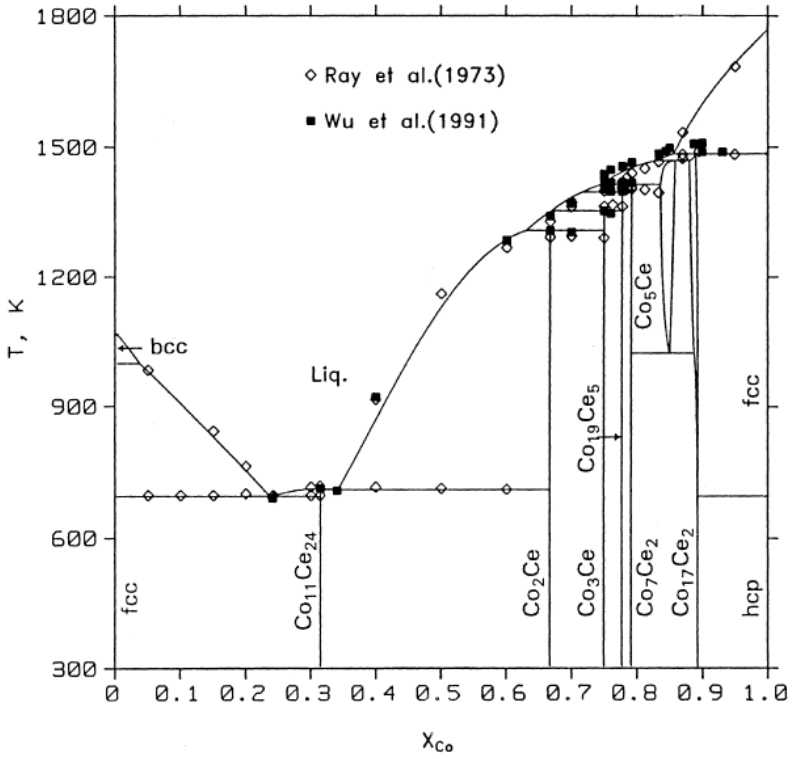

Figure 2.6. Calculated phase diagram according to the second treatment with the experimental measurements [41].

2.2.5 Ce-Fe system

Gschneidner *et al.* [43] reviewed the Ce-Fe system and proposed two stable intermetallics $CeFe_2$ and Ce_2Fe_{17} in this system. This finding was also confirmed by Chuang *et al.* [44] using thermal and microscopic analyses. The Ce-Fe system contains liquid, two peritectic compounds Ce_2Fe_{17} and $CeFe_2$, and six terminal phases α-Fe (bcc-A2), δ-Fe (bcc-A2), γ-Fe (fcc-A1), δ-Ce (bcc-A2), γ-Ce (fcc-A1) and β-Ce (hcp) [43]. Su *et al.* [45] reassessed this system considering the experimental data of [44] and optimized the thermodynamic properties of the compounds. The binary phase diagram calculated by Su *et al.* [45] is shown in Figure 2.7.

Ferromagnetic $CeFe_2$ is reported to have Curie temperature of around 230 K [46], whereas Ce_2Fe_{17} is antiferromagnetic and has two ordering temperatures at 94 K and 206 K [46-47]. Below 94 K, Ce_2Fe_{17} has ferromagnetic magnetic ordering [48]. Above 94 K and below its Néel temperature, 206 K, Ce_2Fe_{17} is antiferromagnetic and it is paramagnetic above the Néel temperature [48]. Gschneidner *et al.* [43] mentioned that Ce_2Fe_{17} occurred in two modifications which have hexagonal and rhombohedral structures. Such variation in crystal structures is the reason for the different ordering temperatures of Ce_2Fe_{17}.

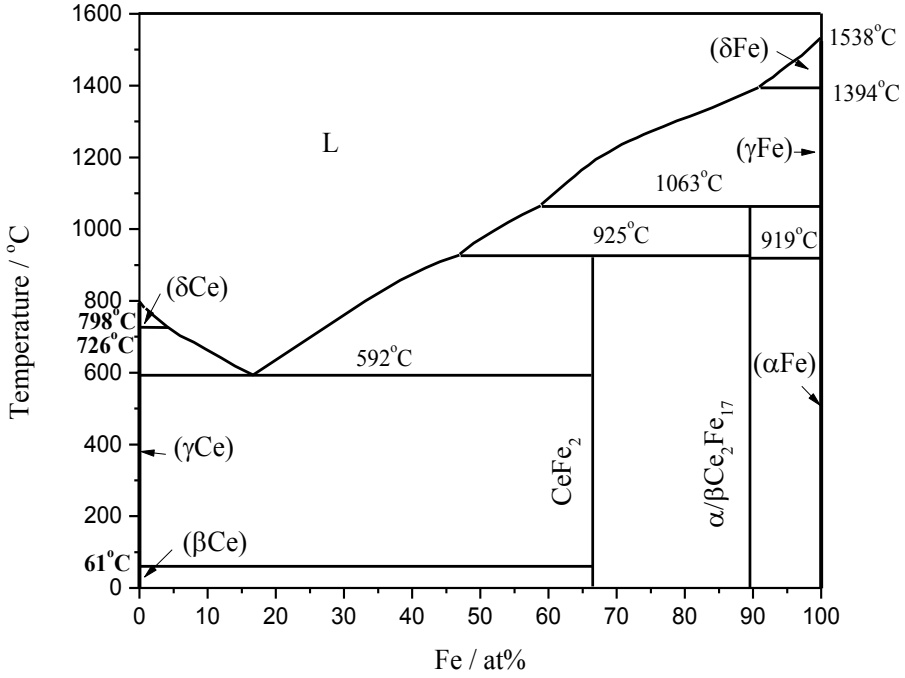

Figure 2.7. Ce-Fe binary phase diagram [45].

2.2.6 Co-Fe system

Co-Fe system has been investigated extensively because of its practical importance in structural and functional alloys, especially in magnetic materials. This system is characterized by α-Fe, γ-Fe, δ-Fe and ε-Co binary solid solutions. Nishizawa *et al.* [49] studied this system and suggested a peculiar shape of the α-Fe (A2)/ γ-Fe (A1) phase boundary which is shown in Figure 2.8. They [49] claimed that the formation of such shape was mainly due to the magnetic contribution. Ohnuma *et al.* [50] reassessed this system by means of X-ray diffraction and thermodynamic analysis as presented in Figure 2.9. They [50] mentioned that the α+γ two-phase region was expected to extend below the temperature at where the disordered α (A2)/the ordered α' (B2) transition met the α/α+γ boundary. They [50] also pointed out that the previous assessment

of this system by Guillermet *et al.* [51] was incomplete, because they [51] did not consider the α (A2)/ α' (B2) order-disorder transition. Later, Ustinovshikov *et al.* [52] studied this system using X-ray diffraction and transmission electron microscopy. However, their [52] calculated phase diagram violated the phase rule which cannot be accepted as an equilibrium diagram, based on the review of this system by Okamoto [53].

In this system, bcc-Fe (α and α') exhibits high saturation magnetization (205-225 emu/g [54]) and Curie temperatures (920-985ºC [55]), and good permeability, good mechanical strength with weak anisotropy field which are ideally suitable for soft magnets [55].

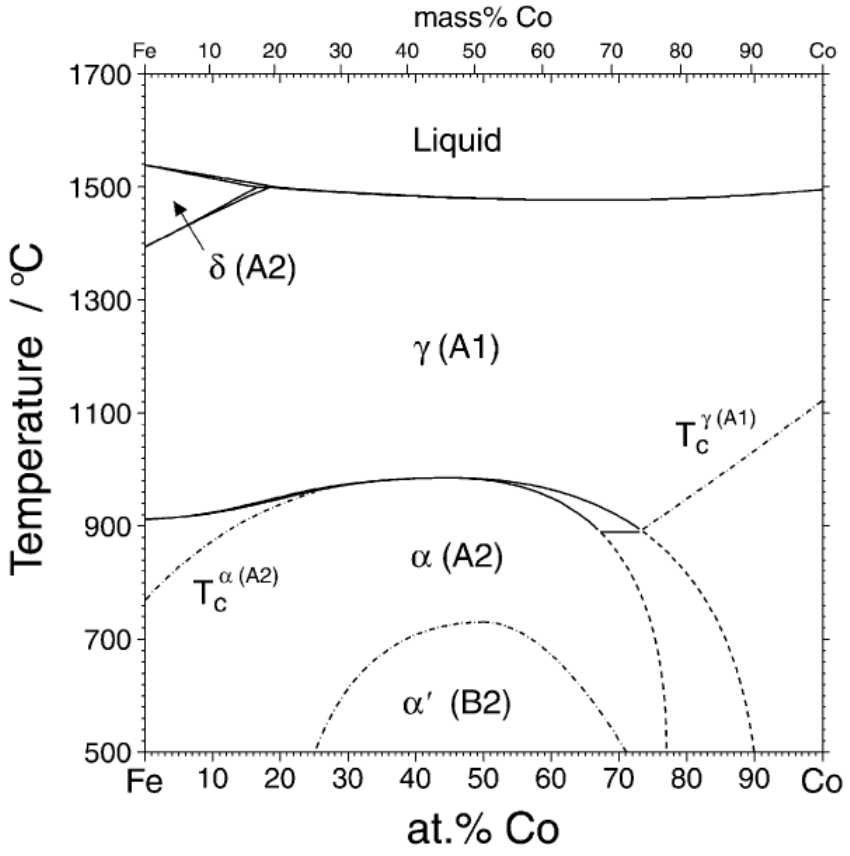

Figure 2.8. Co-Fe binary system [49].

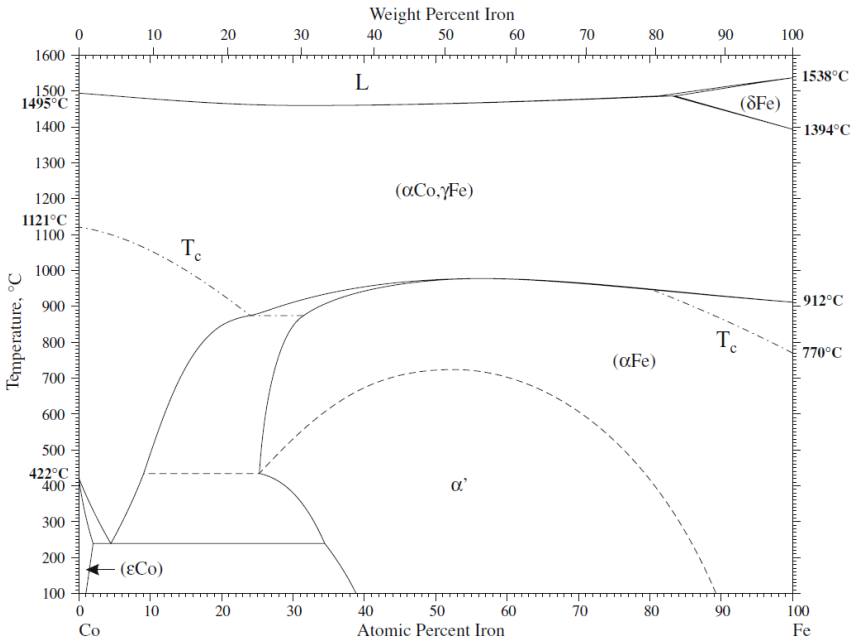

Figure 2.9. Co-Fe binary system [50].

2.3 Ternary sub systems

2.3.1 Ce-Fe-B system

Ce-Fe-B ternary system was first studied by Bilonizhko *et al.* [56]. Three ternary compounds, $Ce_3Fe_{16}B$, $CeFe_2B_2$ and Ce_2FeB_3, were reported. No ternary solubility of binary phases was observed. Later, the crystal structure of $Ce_3Fe_{16}B$ compound was reported by Dub *et al.* [57] and its composition was corrected to $Ce_2Fe_{14}B$. Bezinge *et al.* [58] reported that $CeFe_2B_2$ compound has the $Ce_{1.1}Fe_4B_4$ composition and has a tetragonal $NdCo_4B_4$ structure type. The crystal structure of Ce_2FeB_3 compound was determined by Dub *et al.* [59] and its composition was represented by the formula $Ce_5Fe_2B_6$. Later on, Raghavan *et al.* [60] summarized the previous works [56-59] on this system and redrew the isothermal section at 700°C as shown in Figure 2.10. The compositions of the three ternary compounds were modified by different researchers as follows $Ce_2Fe_{14}B$ [57], $CeFe_4B_4$ [58] and $Ce_5Fe_2B_6$ [59]. The crystal structures of the ternary compounds are taken from Pearson's crystal database [61] and presented in Table 2.1.

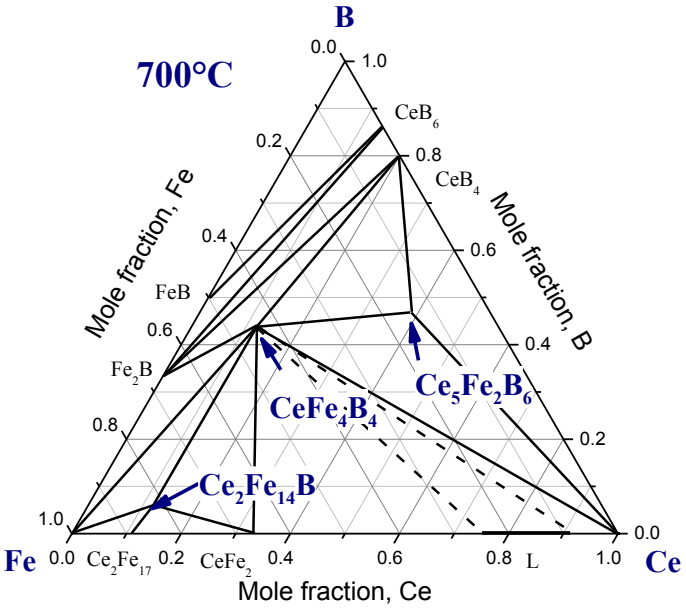

Figure 2.10. Isothermal section of Ce-Fe-B system at 700°C [60].

Table 2.1. Crystal structures of ternary phases in Ce-Fe-B system [61].

Compound	Space group/ Structure type	Lattice parameters, nm		
		a	*b*	*c*
$CeFe_4B_4$	$P4_2/n$ $NdCo_4B_4$	0.7702	0.7702	0.3898
$Ce_5Fe_2B_6$	$R\text{-}3m$ $Pr_5Co_2B_6$	0.5482	0.5482	2.4433
$Ce_2Fe_{14}B$	$P4_2/mnm$ $Nd_2Fe_{14}B$	0.8726	0.8726	1.2057

Magnetic studies of this system were mainly focused on $Ce_2Fe_{14}B$ compound. Neutron diffraction studies of $Ce_2Fe_{14}B$ were performed by Herbst *et al.* [62]. From their observations, the localized *4f* electron of atomic Ce was evidently hybridized into the conduction bands of $Ce_2Fe_{14}B$. The magnetocrystalline anisotropy associated with that component of the Fe (*j2*) moment was

responsible for the 2 kOe coercivity which was also measured from melt-spun Ce-Fe-B ribbons [5]. Another study was carried out by Herbst *et al.* [9], who analyzed twenty two Ce-Fe-B melt-spun samples. They found that $Ce_2Fe_{14}B$ is the only phase among all the alloys offering potential magnetic properties. The intrinsic magnetic properties of $Ce_2Fe_{14}B$ (M_s=11.7 kG, H_a=26 kOe and T_c=151°C) were inferior to those of $Nd_2Fe_{14}B$ (M_s=16 kG, H_a=73 kOe and T_c=312°C) [4]. However, they were also sufficient to offer the potential for producing Ce-Fe-B magnets that have hard magnetic characteristics between those of ferrites (M_s=5.3 kG, H_a=17 kOe and T_c=400°C [2]) and Nd-Fe-B [62]. Considering the lower price of Ce compared to Nd, $Ce_2Fe_{14}B$ may still offer a suitable candidate for less-demanding applications.

2.3.2 Co-Fe-B system

The early experimental studies of this ternary system were published by [4, 9, 63]. Both Rogl *et al.* [63] and Pradelli *et al.* [64] reported isothermal sections at 1000°C. The isothermal section reported by Pradelli *et al.* [64] reasonably agrees with the work of Rogl *et al.* [63] except for the $(Co, Fe)_3B$+$(Co, Fe)_2B$+fcc-A1 three-phase region. Loo *et al.* [65] reported a partial isothermal section at 900ºC. They revealed that Co_2B and Fe_2B form a continuous solid solution $(Co, Fe)_2B$ and Fe substitutes large amount of Co in the Co_3B compound.

Raghavan [66] reviewed the previous experimental works on this ternary system and provided a comparison with the calculated isothermal sections reported by Liu *et al.* [67]. Figure 2.11 (a) demonstrates a reasonable agreement between the isothermal section at 900ºC calculated by Liu *et al.* [67] and the experimental data provided by Loo *et al.* [65]. Figure 2.11 (b) shows an agreement between the Co-Fe-B isothermal section at 1000ºC calculated by Liu *et al.* [67] and the experimental data provided by Rogl *et al.* [63].

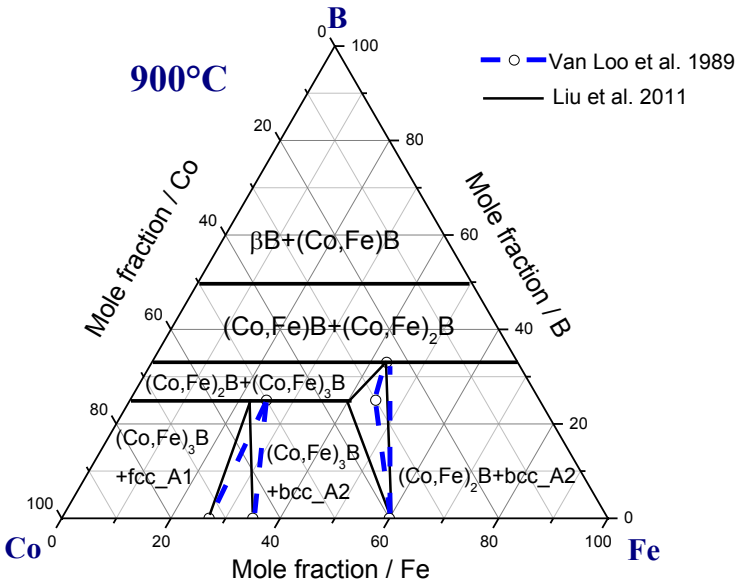

(a)

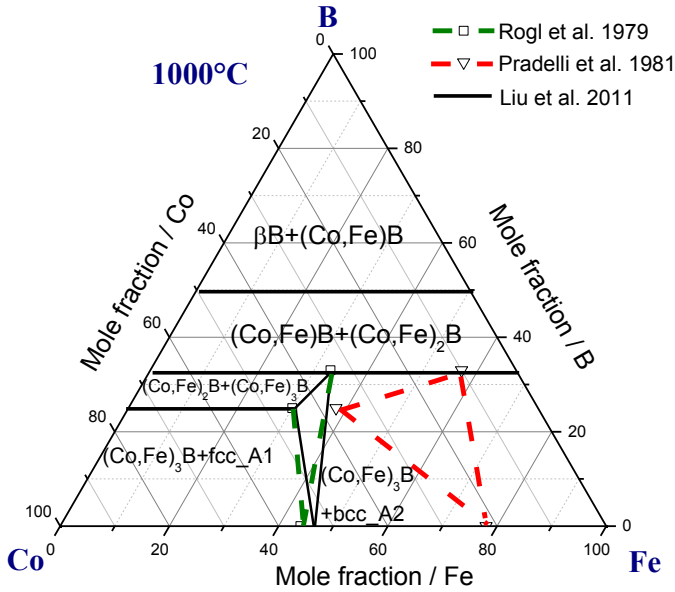

(b)

Figure 2.11. Isothermal section of Co-Fe-B ternary system at (a) 900°C [67]; and (b) 1000°C [67].

The Co-B-Fe system attracted attention because of the formation of magnetic amorphous phases in this system. Such magnetic metallic glass can be used in various applications such as

power devices and information technology [68]. However, the magnetic properties of potential magnetic compounds in this system are still unclear. Recent work was done by Concha *et al.* [69] who studied the $(Fe_xCo_{1-x})_{0.6}B_{0.4}$ ($0 \leq x \leq 1$) amorphous nanoparticles dispersed in a non-magnetic matrix. The results of magnetization measurements as a function of magnetic field for powder sample at room temperature are shown in Figure 2.12. It has been found that the maximum room temperature saturation magnetization is obtained when Co content was at 31 at.%.

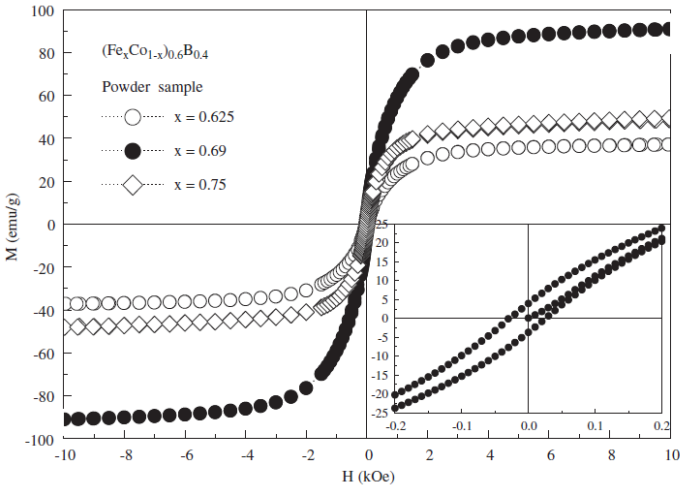

Figure 2.12. Magnetization versus magnetic field at room temperature for $(Fe_xCo_{1-x})_{0.6}B_{0.4}$ powder samples (x=0.625, 0.69 and 0.75) [69].

2.3.3 Ce-Co-Fe system

The available data on the experimental phase equilibria in the Ce-Co-Fe ternary system is limited to the work of Critchley [70], who reported a partial liquidus projection as shown in Figure 2.13 and partial triangulation of the isothermal section at 450ºC (Figure 2.14 (a)). These figures are redrawn from the ASM Alloy Phased Diagram Database [71]. It should be mentioned that the triangulation of the L+Ce+$CeFe_2$ three phase region in Figure 2.14 (a) is incorrect, because $CeFe_2$ compound must not extend beyond 33 at. % Ce at the Ce-Fe side, according to the chemical composition of the compound. Also, the liquid region in the Ce-Co system should be limited to the range of 22–34 at. % Co, based on the most recent Ce-Co binary phase diagram [41]. After the revision, the estimated isothermal section at 450ºC is shown Figure 2.14 (b). Later, Mansey *et al.* [72] studied the change of lattice parameters of the $CeFe_2$-$CeCo_2$ quasibinary section. They reported a continuous solid solution between $CeFe_2$ and $CeCo_2$ compounds. These results were confirmed later by Harris and Longworth [73], and Longworth and Harris [74], who reported that the $CeFe_2$-$CeCo_2$ solid solution at 1173K is a cubic C15 Laves phase. From the description of

Mansey *et al.* [72], $CeCo_2$ and $CeFe_2$ form a continuous solid solution $Ce(Fe, Co)_2$, which is plotted by bold line in Figure 2.14 (b). In this ternary system, the phase equilibria in the Co-Fe side is still unclear. Especially, the phase relationships between Ce_2Co_{17} and Ce_2Fe_{17} are missing in the literature. These two compounds are isostructural with a hexagonal Th_2Zn_{17} crystal structure prototype [61]. Therefore, they are expected to form solid solutions between them. In this work, ternary solid solutions ε_1 ($Ce_2Fe_{17-x}Co_x$ ($0 \leq x \leq 12.35$)) and ε_2 ($Ce_2Co_{17-x}Fe_x$ ($0 \leq x \leq 3.57$)) were found to form between Ce_2Fe_{17} and Ce_2Co_{17} in the Ce-Fe-Co ternary system at 900°C.

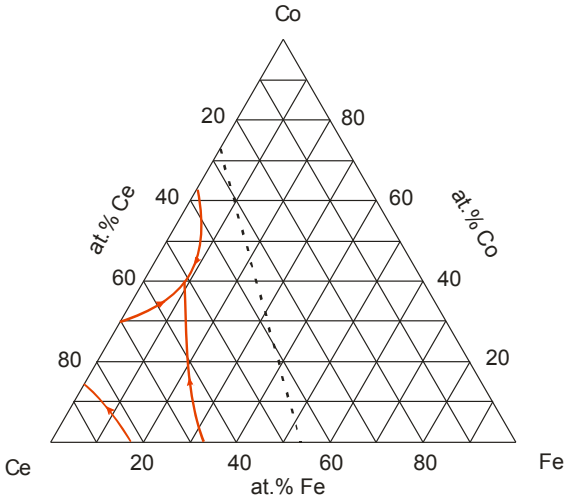

Figure 2.13. Partial liquidus projection of Ce-Co-Fe system [70].

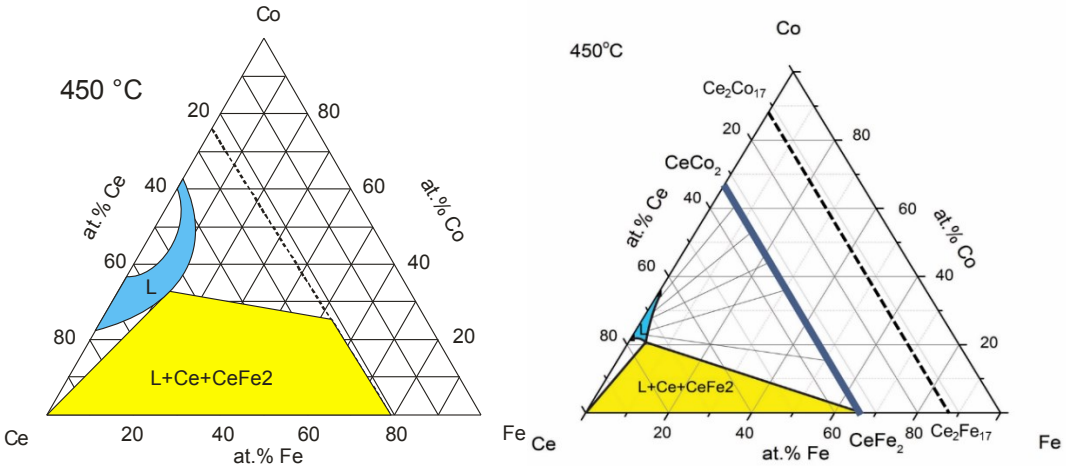

(a) (b)

Figure 2.14. (a) Partial isothermal section of Ce-Co-Fe system at 450ºC [70]; (b) Estimated isothermal section of Ce-Co-Fe system at 450ºC.

Fernández *et al.* [75] pointed out that Curie temperature of $Ce(Fe_{1-x}Co_x)_2$ varied with different Co content. According to [73-76], a small amount of Co substitution in $CeFe_2$ can lead to ferro-antiferromagnetic transition at lower temperatures.

One important magnetic phase in this system is $Ce_2(Fe_{1-x}Co_x)_{17}$ ($x \leq 0.3$). As mentioned in the previous chapter, Ce_2Fe_{17} has high saturation magnetic moments but its Curie temperature is low and does not exhibit uniaxial magnetocrystaline anisotropy at room temperature. However, it has been demonstrated that uniaxial anisotropy was observed in a few pesudobinary $R_2(Fe_{1-x}Co_x)_{17}$ compounds [76]. Xu *et al.* [77] found that the anisotropy of $Ce_2(Fe_{0.9}Co_{0.1})_{17}$ can be modified by nitrogenation. The saturation magnetization in the $Ce_2(Fe_{1-x}Co_x)_{17}$ nitride samples attain a maximum value of 147 emu/g at x=0.2 (18 at.% Co), as compared to the maximum value of 140 emu/g at x=0.3 (27 at.% Co) in the nitrogen-free $Ce_2(Fe_{1-x}Co_x)_{17}$.

2.3.4 Ce-Co-B system

Two partial isothermal sections of the Ce-Co-B ternary system investigated by Bilonizhko *et al.* [78] are shown in Figure 2.15. Thirteen ternary compounds (B_2CeCo_3, B_3CeCo_8, BCeCo, BCe_2Co_4, $BCeCo_4$, $B_3Ce_2Co_7$, B_4CeCo_4, $B_4Ce_3Co_{11}$, BCe_2Co_3, $BCeCo_2$, B_4CeCo, B_3CeCo and B_2Ce_2Co) were found and the crystal structures were determined for seven of them. It was reported that BCeCo is a high-temperature compound that forms at 800ºC and decomposes at 400ºC. Later, four additional ternary compounds were reported: $B_2Ce_2Co_5$ [79], BCe_3Co_{20} [80], B_6CeCo_{12} [81] and $B_6Ce_5Co_2$ [82]. However, the thermal stability of these compounds and their phase relationships are still unknown. Having sixteen ternary compounds makes Ce-Co-B a very complex system. Therefore, a significant amount of experimental and thermodynamic modelling research on this system is still needed. The crystal structures of these ternary compounds are summarized in Table 2.2.

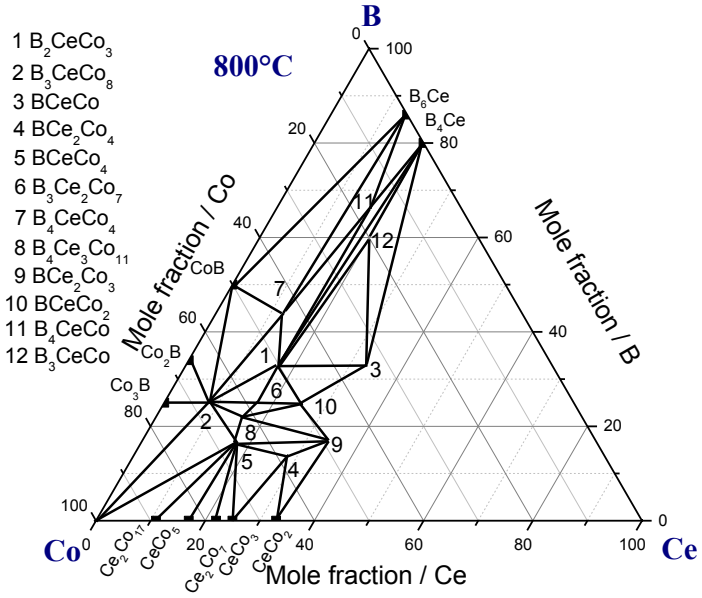

(a)

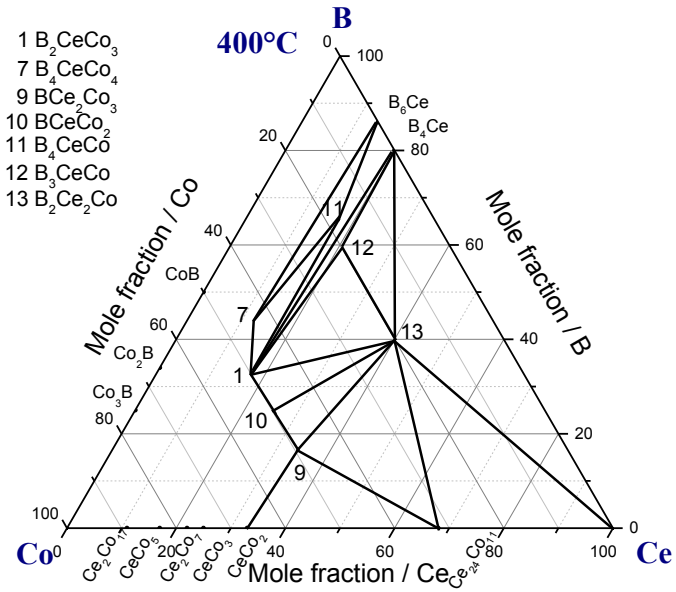

(b)

Figure 2.15. Isothermal section of Ce-Co-B ternary system at (a) 800ºC and (b) 400ºC redrawn from [78].

Table 2.2. Crystal structures of ternary phases in Ce-Co-B system.

Compound	Space group/ Structure type	Lattice parameters, nm			Reference
		a	*b*	*c*	
BCeCo	Trigonal	0.8610	0.8610	0.5540	[78]
$BCeCo_2$	N/A				
$BCeCo_4$	*P*6/*mmm* $CeCo_4B$	0.5011	0.5011	0.6944	[61]
BCe_2Co_3	N/A				
BCe_2Co_4	N/A				
BCe_3Co_{20}	tetragonal	0.8740	0.8740	1.1791	[80]
B_2CeCo_3	*P*6/*mmm* $CeCo_3B_2$	0.5057	0.5057	0.3036	[61]
B_2Ce_2Co	N/A				
$B_2Ce_2Co_5$	$P6_3/mmc$ $Ce_2Co_5B_2$	0.5060	0.5060	2.0430	[79]
B_3CeCo	N/A				
B_3CeCo_8	Monoclinic	1.1840	0.9470	0.7690	[78]
$B_3Ce_2Co_7$	*P*6/*mmm* $Ce_2Co_7B_3$	0.5053	0.5053	1.2970	[61]
B_4CeCo	N/A				
B_4CeCo_4	$P4_2/nmc$ $CeCo_4B_4$	0.5059	0.5059	0.7063	[61]
$B_4Ce_3Co_{11}$	*P*6/*mmm* $Ce_3Co_{11}B_4$	0.5020	0.5020	0.9850	[61]
B_6CeCo_{12}	*R*-3*m* $SrNi_{12}B_6$	0.9479	0.9479	0.7426	[61]
$B_6Ce_5Co_2$	*R*-3*m* $Pr_5Co_2B_6$	0.5478	0.5478	2.4470	[61]

Ce-Co-B system is also a potential magnetic system with several magnetic phases. One important compound is $CeCo_4B$ which was reported to have ferrimagnetic properties. Gencer *et al.* [83] found that $CeCo_4B$ was ferrimagnetically ordered. The Curie temperature of this compound was determined as 293K. If the value of Curie temperature is considered, the $CeCo_4B$ compound appears to be an appropriate candidate for room temperature magnetic refrigerators [83]. Another magnetic compound $Ce_2Co_7B_3$ was reported as ferromagnetically ordered below 250K [84]. Ido *et al.* [84] pointed out that this compound has a high ratio of anisotropy and its Curie temperature was measured around 240K [84]. $CeCo_{12}B_6$ was studied by Jurczyk *et al.* and its Curie temperature was determined as 154K [85]. This temperature was low as compared to $CeCo_4B$ and $Ce_2Co_7B_3$ which indicated a weaker Co-Co exchange interaction [85].

2.4 Ce-Fe-Co-B system

$Ce_2Fe_{14}B$ has been reported as a potential replacement for $Nd_2Fe_{14}B$ [4] for less-demanding applications. Co is an important additive to increase the Curie temperature of $Ce_2Fe_{14}B$ magnets, which could allow for applications requiring thermal stability such as electric motors and wind turbines. Limited experimental results regarding the phase equilibria in the Ce-Fe-Co-B system can be found in the literature. Recently, Skoug *et al.* [10] reported two series of $Ce_3Fe_{14-x}Co_xB$ and $Ce_{2.55}Fe_{14-x}Co_xB_{1.27}$ melt-spun ribbons and their magnetic properties were also studied. They found that the coercivity (H_c) was greater in the $Ce_3Fe_{14-x}Co_xB$ except when x=5 (27 at.% Co). However, H_c decreased monotonically with x in both series. This behavior also reflected the reduction of the magnetocrystalline anisotropy [10]. The values of the remanence (B_r) were comparable in both alloy groups. The details are presented in Table 2.3. Based on their findings [10], B_r was maximum at x=2 (11 at.% Co) and decreased uniformly with lower and higher than x=2 Co content. The maximum value of energy product $(BH)_{max}$ was found to be 4.4 MGOe at x=2 (11 at.% Co) in the $Ce_3Fe_{14-x}Co_xB$ alloy. Curie temperature (T_c) increased almost linearly with x in the range of $0 \leq x \leq 5$. For the sample containing 27 at.% Co (x=5), T_c was measured as 660K, which is similar to the T_c reported for the $Nd_2Fe_{14-x}Co_xB$ and $Pr_2Fe_{14-x}Co_xB$ systems in [4, 12]. It is worth noticing that $Ce_3Fe_{14-x}Co_xB$ (series A) sample x=2 (11 at.% Co) possesses T_c 90K higher than when x=0 with improved values of B_r and $(BH)_{max}$. Therefore, it is important to study the effect of Co on the magnetic properties of $Ce_2Fe_{14}B$ which is the major goal of this thesis.

Table 2.3. Remanence (B_r), coercivity (H_c), maximum energy product $(BH)_{max}$, and Curie temperature (T_c) of annealed ribbons melt-spun from $Ce_3Fe_{14-x}Co_xB$ (series A) and $Ce_{2.55}Fe_{14-x}Co_xB_{1.27}$ (series B) alloys [10].

x	B_r(kG)		H_c (kOe)		$(BH)_{max}$ (MGOe)		T_c (K)	
	Series A	Series B	Series A	Series B	Series A	Series B	Series A	Series B
0	4.6	5.4	6.3	4.6	3.7	3.8	429	433
1	5.1	5.1	5.4	4.5	4.2	3.6	474	484
2	5.2	5.1	4.9	3.7	4.4	3.1	516	539
3	5.0	5.2	4.2	2.9	3.9	2.8	560	585
4	4.7	4.8	3.3	2.5	2.7	2.3	607	624
5	3.6	4.5	1.7	2.2	0.9	1.7	658	666

Co was found to dissolve in $Ce_2Fe_{14}B$ and form magnetic $Ce_2(Fe, Co)_{14}B$ compound. However, the maximum solid solubility of Co in $Ce_2Fe_{14}B$ is still unknown, and the phase relationships need to be understood. Also, the presence of other magnetic phases in this system should be verified. Thus, it is necessary to carry out research to understand the phase equilibria as well as to screen other promising magnetic phases in the Ce-Fe-Co-B system. This is the focus of the current thesis.

2.5 Effects of Ni and Cu on improvement of the magnetic properties

In magnet development, additives are always introduced to improve the magnetic properties as well as thermal stability [13]. However, in many cases, certain properties of permanent magnets are improved by the additives while other properties may become worse. For most of the permanent magnets, a secondary phase is required to prevent the formation of reverse magnetic domains that demagnetize the material [13]. The additives modify the nature of the dominating magnetic phases and the compositions of secondary phases which influence the microstructure and the properties. Additives are also needed to form precipitate on the grain boundaries, slow down the grain growth, and prevent the domain wall movement [14].

In the literature, the study of the effects of Ni and Cu are limited to the magnetic properties of Nd-Fe-B magnets. Bolzoni *et al.* [86] studied the effect of Ni on the intrinsic magnetic properties

of the $Nd_2Fe_{14}B$ compound. They found that both M_s and H_a of $Nd_2(Fe, Ni)_{14}B$ at 293K substantially decreased with Ni substitution. However, Ni substitution gave rise to a slight increase in T_c of $Nd_2(Fe, Ni)_{14}B$. Similar results were also obtained from the study of [88]. Podmiljsak *et al.* [89] concluded that Ni increased the Curie temperature due to the contribution of Fe-Ni interaction which is considered to be larger than the Fe-Fe interaction. It has been revealed that combined substitution of Co and Ni atoms for Fe atoms in Nd-Fe-B sintered magnets improved their corrosion resistance while maintaining their good magnetic properties [90].

In the research of Fukuda *et al.* [91], they found that unlike the individual substitution of Ni for Fe which could lead to decreasing magnetic properties, both saturation magnetization and anisotropy field of $Nd_2Fe_{14}B$ can be restored by combined substitution of Co and Ni for Fe. Ni also influenced coercivity by modifying the microstructure of the alloys. Tang *et al.* [82] compared the Ni- and Cu-substituted $Sm(Co, Fe, Zr)_{8.5}$ magnets. They found that both Ni- and Cu-substituted magnets have similar microstructure. However Cu dissolved in phases in the boundaries, while Ni substituted Co in the matrix phase. The $Sm(Co_{bal}, Fe_{0.1}, Ni_y, Zr_{0.04})_{8.5}$ magnets have very low coercivity at room temperature. With increasing Ni content from y=0.04 (3.5 at.% Ni) to 0.24 (21.5 at.% Ni), the coercivity increased from 0.4 to 1.5 kOe. Then it decreased with a further increase of Ni content as described by Tang *et al.* [92].

Cu addition is found to be an effective way to enhance thermal stability and coercivity. As described by Ragg *et al.* [87], very small additions of Cu from 0.1 to 0.5 at.% were beneficial to Curie temperature, coercivity and corrosion resistance of sintered (Nd, Dy)-Fe-B type magnets, especially when it is added with Co [93]. Similar results were also obtained by Herbst *et al.* [13]. They [13] found that the added Cu in the melt-spun ribbons formed compounds which were concentrated at the grain boundaries. At low concentration, around 0.5 at.%, copper raised the coercivity by 20% relative to copper free ribbons. This enhancement was possible at such low concentrations because the boundary phase accounts for only a small fraction of the bulk magnet. However, excess additives are detrimental to the magnetic properties. Thus, in order to have the optimum magnetic properties, the concentration of the additives have to be carefully controlled. Yet again, this demonstrates that understanding the phase equilibria in this magnetic system is crucial.

The Cu-Fe and Cu-Co binary systems are characterized by metastable liquid miscibility gaps that limit the amount of Cu that can dissolve Fe or Co as can be seen in Figure 2.16 [94, 95]. In

this work, very small quantity of Cu was found to dissolve in matrix magnetic phases such as $Ce_2(Fe, Co)_{14}B$. The existing literature data focuses on the effects of additives (e.g. Ni and Cu) on the magnetic properties of the $Nd_2Fe_{14}B$ compound. The effects of these additives or different ones on the Ce-Fe-Co-B magnetic compounds have not been studied. This project will attempt to fill the above mentioned research gaps.

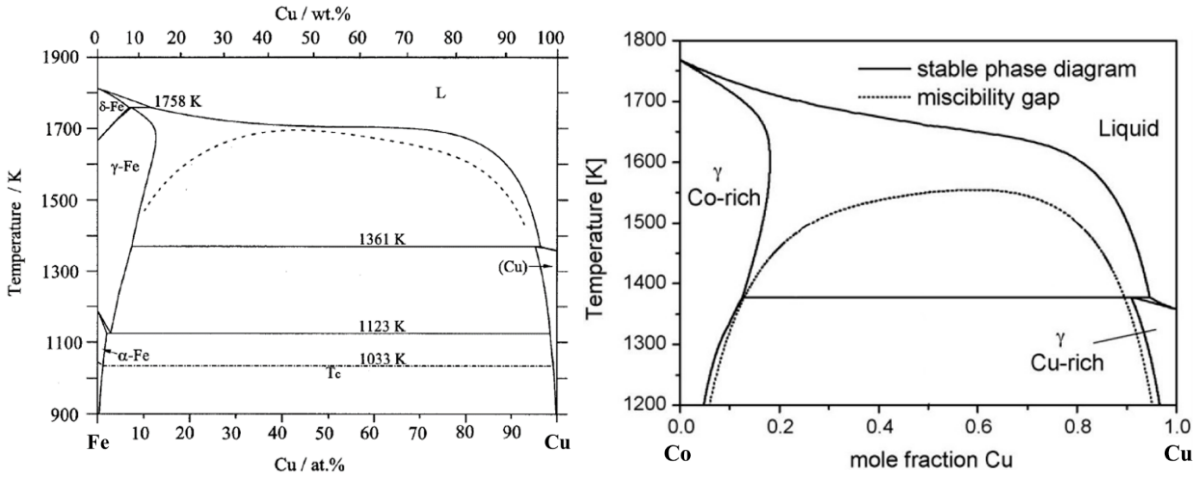

(a) (b)

Figure 2.16. (a) Phase diagram of Cu-Fe binary system [94]; (b) Phase diagram of Cu-Co binary system [95].

Chapter 3: Methodology

Combining diffusion couples and key alloys, with the aid of the Scanning Electron Microscope (SEM) and Magnetic Force Microscope (MFM), forms a high throughput screening (HTS) method that is more efficient to understand the phase equilibria and to screen magnetic compounds in a multi-component system. HTS is used to screen magnetic phases in the Ce-Fe-Co-B multi-component system combining microstructural, micro-elemental, and magnetic domain analyses of diffusion couples and key alloys. Magnetic phases could be identified through their domain interactions with the magnetic tip of the MFM. The analysis of one successful diffusion couple can potentially give complete information on a large number of intermetallic phases in the system at a specific temperature. Based on the diffusion couples results, key alloys are prepared and studied further by X-ray diffraction (XRD) for phase identification and by MFM to confirm the presence of a magnetic phase in a significant amount. Importantly, the key alloys can be used to measure intrinsic magnetic properties, such as saturation magnetization, anisotropy field, and Curie temperature. HTS significantly reduces the number of experiments and the timeframe. However, ternary or quaternary diffusion couples have unpredictable diffusion paths, which could lead to omitting some phases. Besides, slow kinetic formation of some phases may cause the formation of thin layers that might be difficult to be successfully analyzed [96]. Therefore, key alloys are used to verify the results obtained from diffusion couples.

3.1 Experimental procedure

Elements with 99 wt.% purity or higher are used as the starting materials. All the elements were supplied by Alfa Aesar® (Haverhill, MA, USA). Samples of known composition are prepared from the pure metals using an arc melting furnace under argon atmosphere. The arc-melting furnace is equipped with a water-cooled copper crucible and a non-consumable tungsten electrode. Every alloy was melted several times to ensure homogeneity. The actual global composition is determined by EDS area analysis. The prepared samples are used as key alloys or as end-members for diffusion couples experiments. For annealing process, samples are encapsulated inside quartz tubes under vacuum. After sufficient annealing time (at least 25 days), the alloys are quenched in a cold-water bath, to obtain the high-temperature structure. Quenched samples or diffusion couples were grinded and polished down to 1 μm in order to be analyzed using SEM coupled with Energy/Wavelength Dispersive X-ray Spectroscopes (EDS/WDS) and

MFM. The microstructure and phase composition of the samples were analyzed by SEM/WDS (HITACHI S-3400N, HITACHI, Tokyo, Japan). Pure boron standard was used for calibration. Optimum 2500 cps for correctly measuring low boron content in WDS was attained using 20 kV accelerating voltage, around 92 nA probe current and 30 nA beam current. XRD was performed for the key alloys using PANAnalytical Xpert Pro X-ray diffractometer (PANAnalytical, Almelo, The Netherlands) with a CuKα radiation at 45 kV and 40 mA. The XRD spectrum is acquired from 20 to 90° 2θ with a 0.02° step size. XRD patterns were analyzed using X'Pert Highscore plus software [97] and the Rietveld method. The crystal structure prototypes of the detected phases were obtained from Pearson's Database [61] and used in XRD analysis. The magnetic domain structures of samples were investigated for MFM imaging using Digital Instruments Multimode Atomic Force Microscope (Digital Instruments, Billerica, MA, USA) in LiftMode.

3.2 Characterization of magnetic compounds

3.2.1 Magnetic force microscopy

The magnetic force microscope is a variant of the atomic force microscope which is capable of revealing the domain structure of magnetic samples in real space. The magnetic contrast is achieved through the magnetostatic interaction between a ferromagnetic tip and the stray fields from a sample. The stray field or field gradient close to the domain wall is different from that inside a domain. By mapping the stray field or field gradient, the magnetic domain structures can be obtained [98].

The basic principle of MFM is illustrated in Figure 3.1. A flexible cantilever beam with a sharp magnetic probe on its end, is used as a force sensor [99]. If the tip is brought close enough to the sample surface, typically between ten to a few hundred nanometers. The magnetic interaction between the tip and sample can give rise to a change of the cantilever status, such as static deflection or resonant frequency [99]. As the MFM tip scans across the sample, a two dimensional magnetic image can be obtained from the change in the cantilever status. In magnetic force microscopy, the cantilever status is monitored with respect to the tip-sample separation [99].

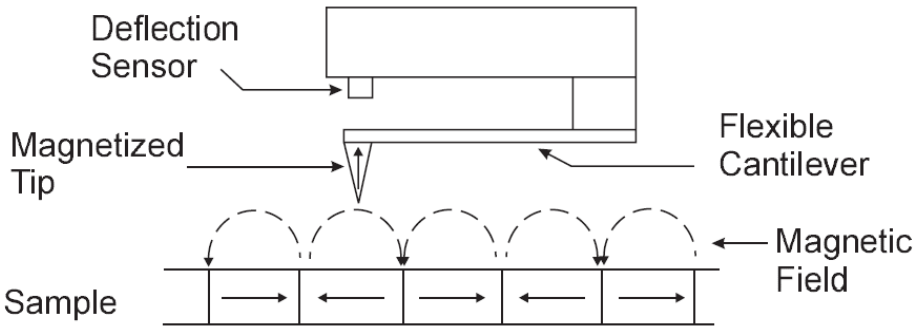

Figure 3.1. A magnetically sensitive cantilever interacts with the magnetic stray field of the sample. Resulting changes in the status of the cantilever are measured by the deflection sensor, and recorded to produce an image [99].

In this work, a 225 μm long silicon cantilever having a magnetic pyramidal tip was used to acquire the magnetic gradient images. The MFM tip, supplied by Appnano Ltd., (Mountain View, CA, USA), was coated with an approximately 50 nm CoCr layer. The magnetized MFM tip is perpendicular to the sample surface and points downward during the measurement. The parameters used to obtain the MFM images are 1 H_z scan rate, 0.2 integral gain and 0.4 proportional gain. The cantilevers have resonant frequency between 47 and 76 kHz. This frequency is shifted by an amount proportional to the vertical gradient of the magnetic forces on the tip [100]. The frequency shifts can be detected by the phase detection capability of the MFM. The drive frequency of the cantilever for the phase detection was set to be the center of the cantilever resonance. The signal was measured as the cantilever's phase of oscillation relative to the piezo drive. And the magnetic contrast can be achieved through the magnetostatic interaction between the MFM tip and the stray fields from the sample which is measured via a laser beam reflecting off the back of the cantilever [100]. Figure 3.2 illustrates the magnetic domain of $Ce(Co, Fe, Ni)_4B$ through MFM test via Tapping/Lift mode. When attractive interactions occur, negative phase shift and dark image contrast can be observed in the MFM images. Whereas, positive phase shift and bright image contrast result when repulsive interactions take place [100]. When imaging with MFM, one concern is that stray fields from the magnetic tip modifies the micromagnetic structure of the sample [101]. A test for this is usually performed by observing the dependence of the micromagnetic structure on the MFM tip scan height [102]. For the samples studied in this work, there was no variation of the sample micromagnetic structure when the tip scan height was varied

between 30 and 200 nm. Thus, we assume that modification of the micromagnetic structure of the samples by the tip is assumed to be negligible.

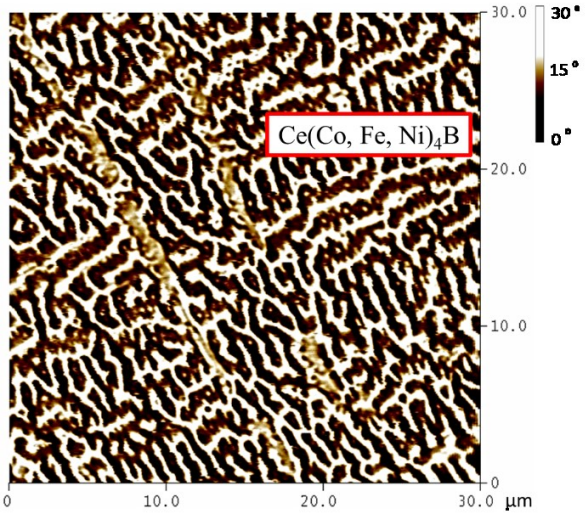

Figure 3.2. Magnetic force image of a $Ce(Co, Fe, Ni)_4B$.

3.2.2 Intrinsic magnetic properties measurements

Rare earth permanent magnets exhibit a complex, multiphase microstructure which considerably influences the coercivity and the remanence of the magnets. The magnetic interactions consist of long range dipolar interaction and short range exchange coupling between misaligned grains [103]. The contribution of exchange couple between misaligned grains becomes more dominant with decreasing grain size. Large coercivity is always associated with small and strongly coupled grains [103]. The processing route of magnet strongly influences the grain size. Therefore in this work the extrinsic properties are not studied, only intrinsic magnetic properties of promising compounds are discussed.

Saturation magnetization and anisotropy field were measured using the Quantum Design Physical Property Measurement System (PPMS-9T, San Diego, CA, USA) at 298 K. The samples were cut into cubic shapes of approximately 25 mg weight. The saturation magnetization was obtained in external field up to 50 kOe. Since Ce-Fe-Co-B is a complex multi-component system, it is extremely difficult to obtain a single phase sample, especially because certain magnetic phases such as $Ce_2(Fe, Co)_{14}B$ form through a peritectic reaction [104]. Practically, in order for the magnetic properties of the alloys to be attributed to the magnetic phase, samples should contain at least seventy mass percent of the magnetic phase of interest with certain amounts of secondary phases which could help impeding domain wall motion [9]. In this research, over 80 wt.% of the

magnetic phase was obtained in all the samples after the annealing process. However, to describe the saturation magnetization precisely, all the M_s results of the magnetic Ce-Fe-Co-B solid solutions (e.g. $M_s^{Ce2Fe14\text{-}xCoxB}$) reported in this research have been corrected based on the following equation [113]:

$$M_s^{sample} = (w_i^{Ce2Fe14\text{-}xCoxB} \times M_s^{Ce2Fe14\text{-}xCoxB} + w_i^{imp} \times M_s^{imp}) / 100 \qquad (1)$$

where M_s^{sample} is the saturation magnetization of the sample obtained using PPMS; $w_i^{Ce2Fe14\text{-}xCoxB}$ and w_i^{imp} are the weight percentages of $Ce_2Fe_{14\text{-}x}Co_xB$ and impurity respectively, obtained using XRD through Rietveld analysis; M_s^{imp} is the saturation magnetization of the impurity taken from the literature.

The magnetic anisotropy field was determined by the Singular Point Detection (SPD) method, using the second derivative of magnetization (d^2M/dH^2) [105-107]. Curie temperature was measured by TA instruments Q50 (New Castle, DE, USA) thermogravimetric analysis (TGA) with a constant magnetic field applied to the sample. Pure Ni was used as a calibration standard. The error in Curie temperature measurement of Ni was observed to be ±3°C. The Curie temperature of the magnetic compound and its dependence on compositions are studied and discussed. All the intrinsic magnetic property measurements were repeated two or four times. The differences between two measurements were noted to be less than 3.2 emu/g for M_s, 2.7 kOe for H_a, and 4.1 °C for T_c and the average values were reported.

Chapter 4: Phase equilibria and magnetic phases in the Ce-Fe-Co-B system

The results of this work are divided into three chapters: Chapter 4 covers the investigation of phase equilibria in the Ce-Fe-Co-B system and the determination of magnetic phases; three magnetic phases, $Ce_2(Fe, Co)_{14}B$, $Ce(Co, Fe)_4B$ and $Ce_3(Co, Fe)_{11}B_4$, are identified. Among them, $Ce(Co, Fe)_4B$ and $Ce_3(Co, Fe)_{11}B_4$ are Co-rich compounds which are not the main objectives in this work. Therefore, only the intrinsic magnetic properties of $Ce_2(Fe, Co)_{14}B$, and its modifications by Ni and Cu are reported in Chapter 5; the magnetic force microscopic study of $Ce_2(Fe, Co)_{14}B$, and its modifications by Ni and Cu are summarized in Chapter 6.

4.1 Diffusion couples results

In order to understand the phase equilibria in the Ce-Fe-Co-B system, four diffusion couples were prepared. The chemical compositions across the diffusion couples and the corresponding phases that formed in the diffusion layers are listed in Table 4.1. Diffusion couples were all annealed at 900 °C for 4 weeks.

Table 4.1. Chemical compositions across the diffusion couples and the corresponding phases.

Diffusion Couple	Layer	Composition (at. %)				Corresponding Phase
		Ce	Fe	Co	B	
DC1 ($Ce_2Fe_{14}B$/Co)	1	12	82-73	0-9	6	$Ce_2(Fe, Co)_{14}B$
		0	100-93	0-7	0	α-(Fe, Co)
	2	11	79-34	10-55	0	$Ce_2(Fe, Co)_{17}$
		0	93-57	7-43	0	α-(Fe, Co)
	3	16	9	59	16	$Ce(Co, Fe)_4B$
		0	57-39	43-61	0	α-(Fe, Co)
	4	11	19	70	0	$Ce_2(Co, Fe)_{17}$
		0	39	61	0	α-(Fe, Co)
	5	0	35-30	65-70	0	α-(Fe, Co)
	6	0	12	88	0	γ-(Fe, Co)
		11	2	87	0	$Ce_2(Co, Fe)_{17}$
DC2	1	12	82-60	0-22	6	$Ce_2(Fe, Co)_{14}B$

$(Ce_{13}Fe_{80}B_7/Co_{90}Ce_{10})$		0	100-82	0-18	0	α-(Fe, Co)
	2	15	27-17	42-52	16	$Ce(Co, Fe)_4B$
		0	82-37	18-63	0	α-(Fe, Co)
	3	0	35-33	65-67	0	α-(Fe, Co)
	4	16	6-1	63-68	15	$Ce(Co, Fe)_4B$
		11	14	75	0	$Ce_2(Co, Fe)_{17}$
	5	0	11-0	89-100	0	γ-(Fe, Co)
		11	14-0	75-89	0	$Ce_2(Co, Fe)_{17}$
DC3 $(Ce_{10}Fe_{75}B_{15}/Co)$	1	12	82-65	0-17	6	$Ce_2(Fe, Co)_{14}B$
		0	100-70	0-30	0	α-(Fe, Co)
		13	38	4	45	$Ce_{13}Fe_{38}Co_4B_{45}$
	2	16	21-5	40-56	23	$Ce_3(Co, Fe)_{11}B_4$
		0	70-44	30-56	0	α-(Fe, Co)
	3	6	11	53	30	$Ce(Co, Fe)_{12}B_6$
	4	0	33-30	67-70	0	α-(Fe, Co)
DC4 $(Ce_{15}Fe_{43}Co_{19}B_{23}/Co)$	1	16	45-40	23-28	16	$Ce(Co, Fe)_4B$
		0	17	83	0	α-(Fe, Co)
		13	32	10	45	$Ce_{13}Fe_{32}Co_{10}B_{45}$
	2	17	23-9	37-51	23	$Ce_3(Co, Fe)_{11}B_4$
		0	65-53	35-47	0	α-(Fe, Co)
	3	6	18-9	46-55	30	$Ce(Co, Fe)_{12}B_6$
		0	53	47	0	α-(Fe, Co)
	4	0	31	69	0	α-(Fe, Co)
	5	0	14-11	86-89	0	γ-(Fe, Co)

The backscattered electron (BSE) image of DC1 is presented in Figure 4.1 (a). As a result of diffusion between $Ce_2Fe_{14}B$ and Co, six diffusion layers formed. The compositions of the formed phases were determined using WDS point analysis. The solubility ranges were measured by WDS line scan. In the first layer, the end-member $Ce_2Fe_{14}B$ (white) was in equilibrium with the α-(Fe, Co) phase (black). Fe was substituted by Co in both phases during the diffusion process. A WDS

compositional profile of $Ce_2(Fe, Co)_{14}B$ is shown in Figure 4.1 (b). The quaternary solid solubility of $Ce_2Fe_{14}B$ was determined as 9 at. % Co, which was presented by the formula $Ce_2Fe_{14-x}Co_xB$ ($0 \leq x \leq 1.54$). Co in α-Fe in layer 1 was found to be 6 at. %. The grey phase in layer 2 was identified as $Ce_2(Fe, Co)_{17}$ with $Ce_{11}Fe_{34-79}Co_{10-55}$ composition and named as ε_1 in this study. The WDS compositional profile of $Ce_2(Fe, Co)_{17}$ is plotted in Figure 4.1 (c). At the boundary between layers 1 and 2, three phase equilibrium ($Ce_2(Fe, Co)_{14}B$/α-(Fe, Co)/ε_1) was observed. Moreover, the concentration of dissolved Co in α-Fe phase (black) also gradually increased from 6 to 44 at. % in layer 2. White phase in layer 3 was found to be a stoichiometric compound with $Ce_{16}Fe_9Co_{59}B_{16}$ composition. This new quaternary compound is in equilibrium with α-(Fe, Co) (black) and had similar composition to $CeCo_4B$, considering the Fe-Co substitution which was also confirmed by key alloys. A three-phase region was established between ε_1, α-(Fe, Co), and $Ce(Co, Fe)_4B$. Co-rich $Ce_2(Co, Fe)_{17}$ with $Ce_{11}Fe_{19}Co_{70}$ chemical composition was detected in layer 4, where it is in equilibrium with α-(Fe, Co). Substitution of Fe by Co was found to be up to 61 at. %. Another three-phase region was obtained among α-(Fe, Co), $Ce(Co, Fe)_4B$, and $Ce_2(Co, Fe)_{17}$. Through WDS analysis, layer 5 has been analyzed as α-(Fe, Co) and its homogeneity range was measured as 65-70 at. % Co. The dominating black phase in the thin layer 6 was determined to be γ-(Fe, Co) with a relatively small Fe amount of about 8-12 at. %. This phase is in equilibrium with $Ce_2(Co, Fe)_{17}$ (white), which was measured to have $Ce_{11}Fe_2Co_{87}$ chemical composition. This two-phase equilibrium is also confirmed by DC2.

The experimental results of DC1 are summarized in the 3D view, as shown in Figure 4.2 (a). The phases which were detected in this diffusion couple are denoted by different colors. The ε_1 and α-(Fe, Co) are illustrated on the Fe-Co-Ce ternary system in Figure 4.2 (b). Two pseudo ternary sections at 12 at. % and 16 at. % Ce are plotted in Figure 4.2 (c,d) to enable better understanding of the phase relations in DC1. The phase relations obtained from DC1 are summarized in Figure 4.2 (e). Three three-phase regions, $Ce_2(Fe, Co)_{14}B$/α-(Fe, Co)/ε_1, α-(Fe, Co)/ε_1/$Ce(Co, Fe)_4B$, and $Ce(Co, Fe)_4B$/α-(Fe, Co)/$CeFe_2Co_7$, are established at the interfaces from layers 1 to 4 of DC1.

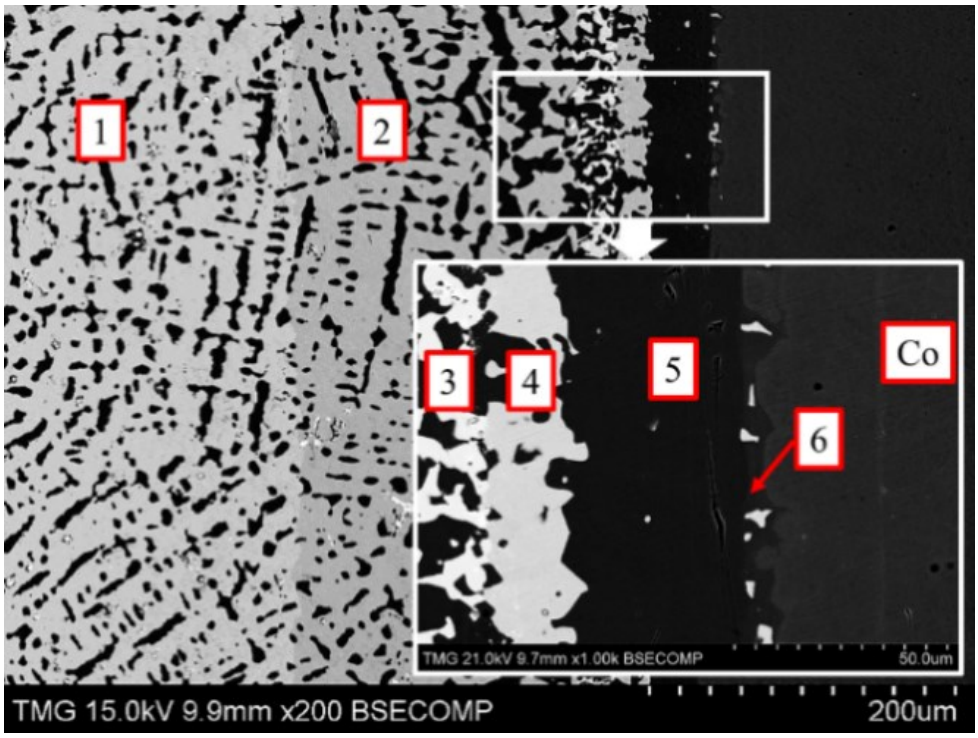

(a)

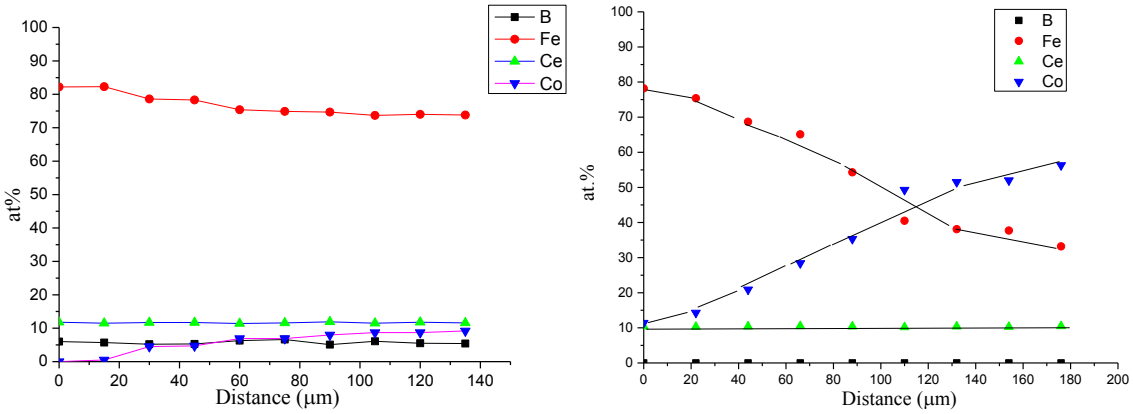

(b) (c)

Figure 4.1. (a) BSE image of DC1; (b) WDS compositional profile of $Ce_2(Fe, Co)_{14}B$ in layer 1; (c) WDS compositional profile of $Ce_2(Fe, Co)_{17}$ in layer 2.

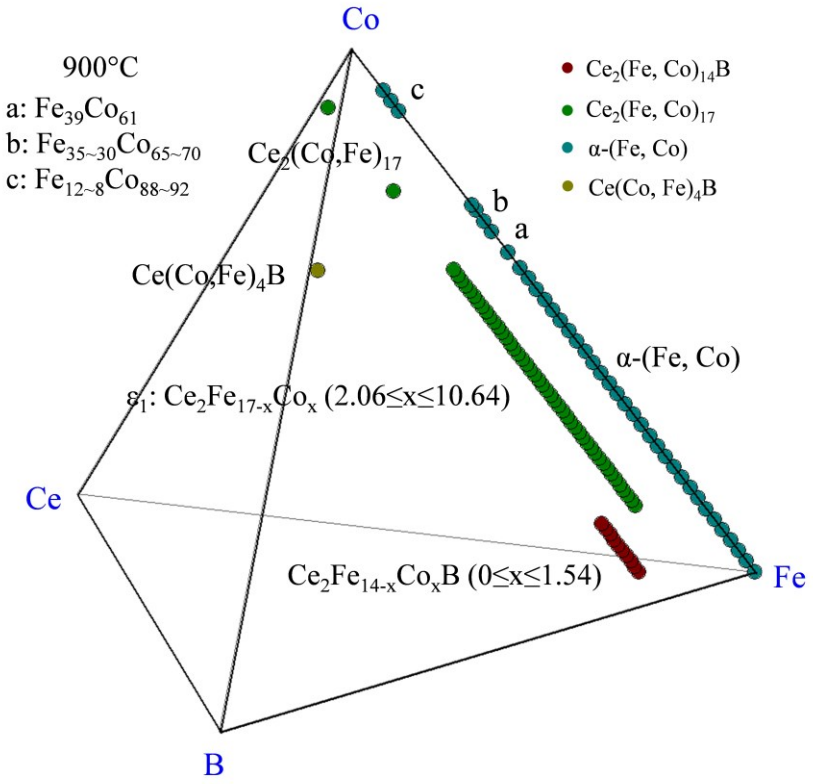
Co
900°C
a: $Fe_{39}Co_{61}$
b: $Fe_{35\sim30}Co_{65\sim70}$
c: $Fe_{12\sim8}Co_{88\sim92}$
$Ce_2(Co,Fe)_{17}$
$Ce(Co,Fe)_4B$
ε_1: $Ce_2Fe_{17-x}Co_x$ (2.06≤x≤10.64)
$Ce_2Fe_{14-x}Co_xB$ (0≤x≤1.54)
α-(Fe, Co)
$Ce_2(Fe, Co)_{14}B$
$Ce_2(Fe, Co)_{17}$
α-(Fe, Co)
$Ce(Co, Fe)_4B$
a
b
c
Ce
Fe
B

(a)

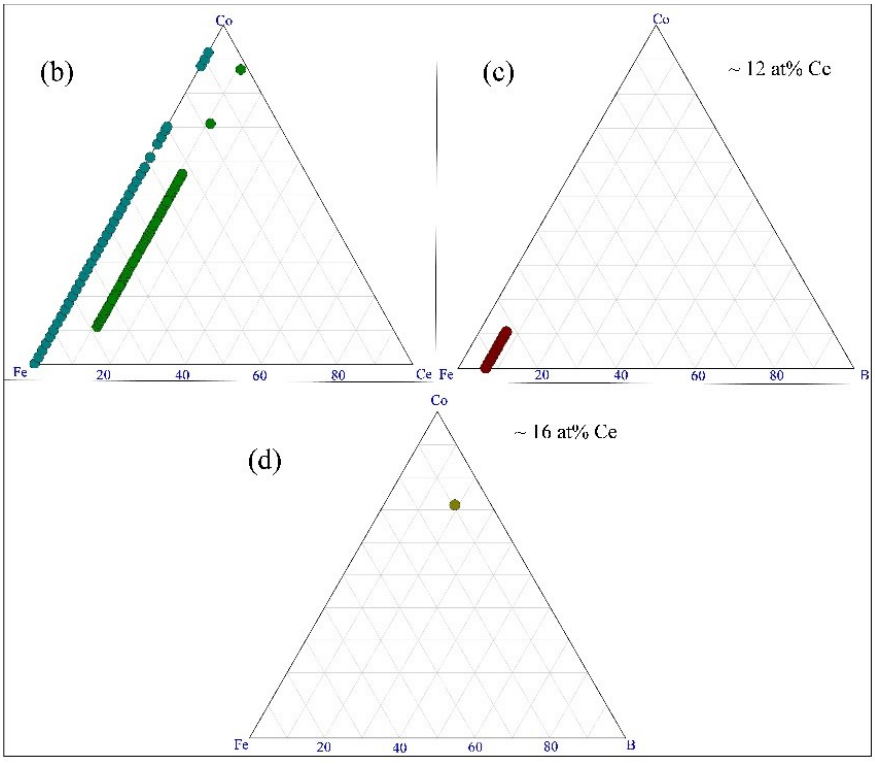
(b)
Co
Fe
Ce
20
40
60
80
(c)
~ 12 at% Ce
Co
Fe
B
20
40
60
80
(d)
~ 16 at% Ce
Co
Fe
B
20
40
60
80

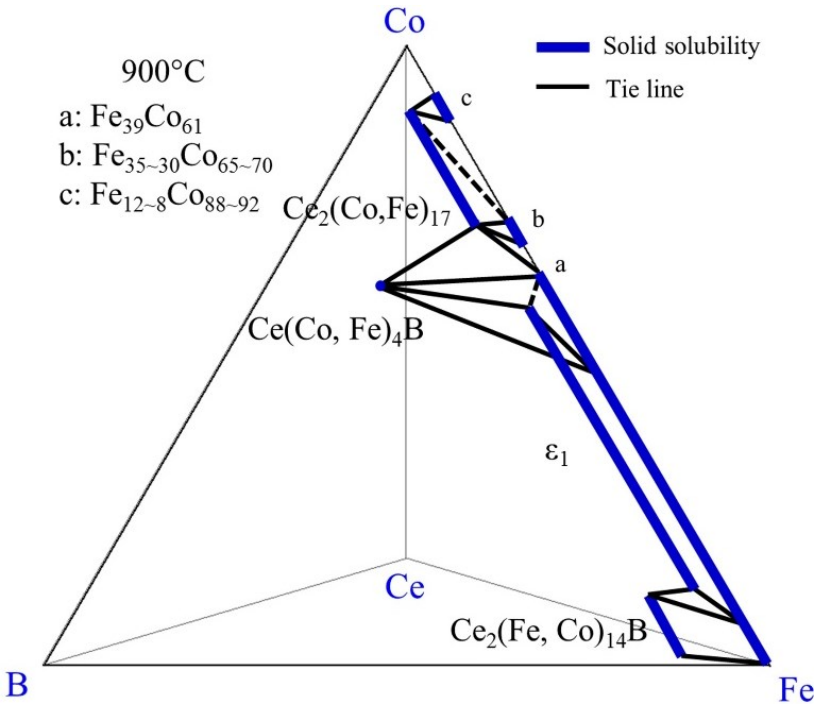

(e)

Figure 4.2. The results of the diffusion couple 1 at 900 °C: (a) 3D presentation of the experimental results; (b) Fe-Ce-Co ternary system; (c) pseudo ternary section at ~12 at. % Ce; (d) pseudo ternary section at ~16 at. % Ce; (e) phase relations obtained from DC1.

$Ce_{13}Fe_{80}B_7$ and $Co_{90}Ce_{10}$ were selected as the end-members of DC2. By doing so, the diffusion path may cross several phase regions, and Fe/Co atomic exchange in $Ce_2(Fe, Co)_{14}B$ can be further understood. The $Ce_2(Fe, Co)_{14}B$ phase was confirmed in DC2 and its solid solubility was measured as 22 at. % Co which was greater than the value obtained from DC1. Two layers of $Ce(Co, Fe)_4B$ were observed in DC2, with solid solubility of 17-27 at. % Fe and 1-6 at. % Fe. From SEM/WDS analysis, as listed in Table 1, a single α-(Fe, Co) layer (layer 3) formed in between the two $Ce(Co, Fe)_4B$ layers (layers 2 and 4) which could hinder the Co/Fe atomic exchange in $Ce(Co, Fe)_4B$. This is why two layers of this solid solution were obtained instead of a continuous $Ce(Co, Fe)_4B$ layer. $Ce_2(Co, Fe)_{17}$ and γ-(Fe, Co) two-phase equilibrium was observed and confirmed in layer 5 of DC2, as presented in Table 1. By analyzing DC3, $Ce_3(Co, Fe)_{11}B_4$ and $Ce(Co, Fe)_{12}B_6$ were found to form in this quaternary system at 900 °C and their solid solubilities were measured as 5-21 at. % Fe and 11 at. % Fe, respectively, as can be seen in Table 1. Later, these two phases were all confirmed by DC4.

DC4 was designed by combining relatively high Co content $Ce_{15}Fe_{43}Co_{19}B_{23}$ alloy with a pure Co piece. It is impossible to control the diffusion path of diffusion couples. Therefore, it is very essential to select the proper end-members of diffusion couples in order to cross a large number of phase regions, so that more phase equilibria results could be revealed. The BSE image of DC4 is presented in Figure 4.3 (a), the $Ce_{15}Fe_{43}Co_{19}B_{23}$ end-member was found to be in the $Ce_{13}Fe_{32}Co_{10}B_{45}$/Ce(Co, Fe)$_4$B/α-(Fe, Co) three-phase region. The homogeneity range of Ce(Co, Fe)$_4$B was determined as 40–45 at. % Fe. A new boron-rich compound, $Ce_{13}Fe_{32}Co_{10}B_{45}$, was found and more studies have been performed by key alloys to further analyze this compound which will be discussed in the next section. As shown in the enlarged inset of Figure 4.3 (a), four diffusion layers are present. From WDS analysis, the composition of the white phase in layer 2 was measured as $Ce_{17}Fe_{23-9}Co_{37-51}B_{23}$, as presented in the WDS compositional profile in Figure 4.3 (b). Similar to DC3, this phase was identified as Ce_3(Co, Fe)$_{11}B_4$, which was also confirmed by key alloys. Layer 3 mainly contained a Ce(Co, Fe)$_{12}B_6$ phase which had $Ce_6Fe_{18-9}Co_{46-55}B_{30}$ composition. The results of WDS compositional analysis of layer 3 are plotted in Figure 4.3 (c). From DC3 and DC4, a Ce(Co, Fe)$_{12}B_6$ phase is confirmed. Key alloys are used to measure its maximum solubility at 900 °C. A thick layer number 4, which contained α-(Fe, Co) with $Fe_{31}Co_{69}$ composition, formed in this diffusion couple.

The experimental results of DC4 are summarized in the 3D view shown in Figure 4.4 (a). Different phases are demonstrated by different colors. The α-(Fe, Co) phase is projected on a Fe-Co-Ce ternary system in Figure 4.4 (b). The phases detected from this diffusion couple are illustrated by three pseudo ternary sections at 6 at. %, 12 at. %, and 16 at. % Ce, which are shown in Figure 4.4 (c-e). The phase relations in DC4 are plotted in Figure 4.4 (f). Solid lines represent the phase regions established from DC4 and dotted lines indicate possible phase equilibria among detected phases.

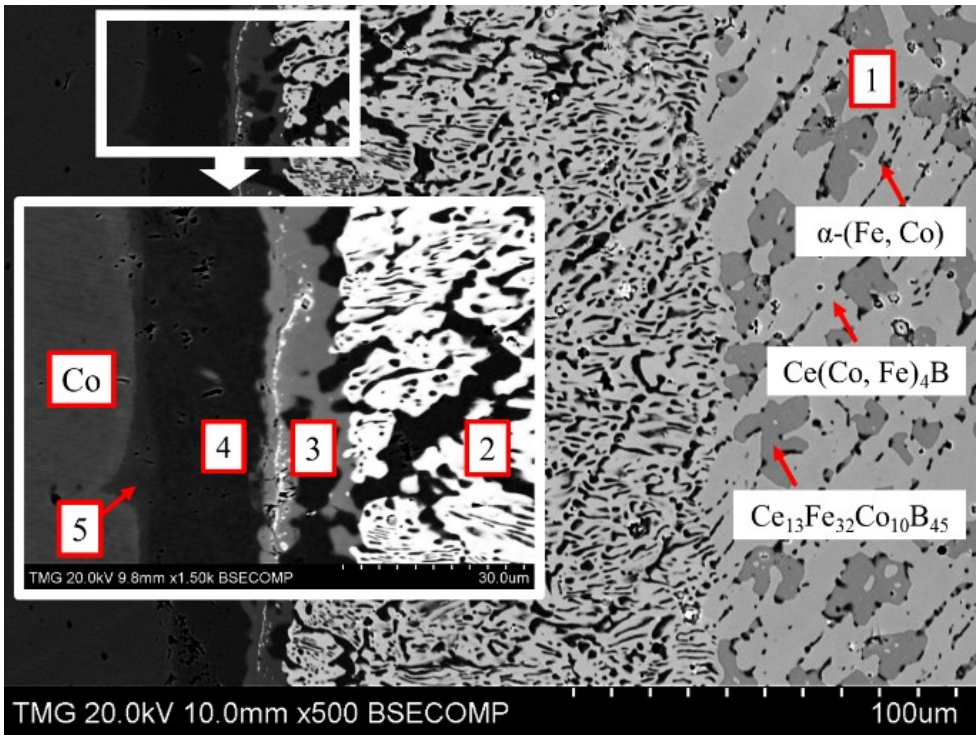

(a)

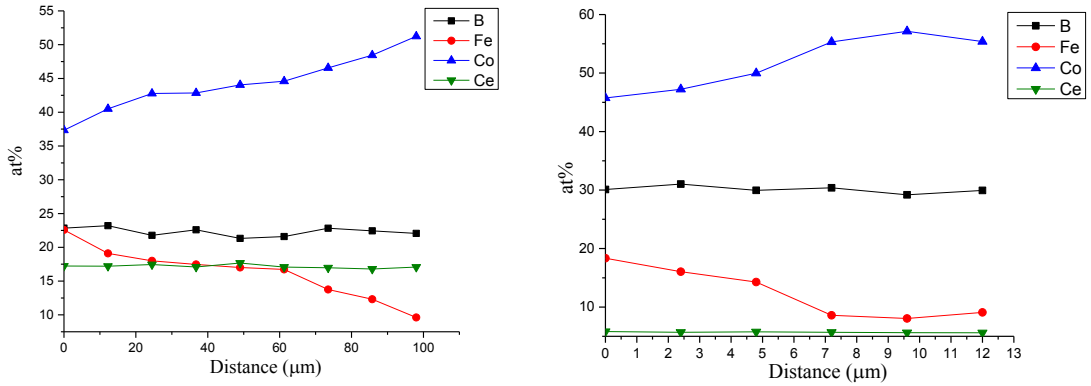

(b) (c)

Figure 4.3. (a) BSE image of DC4; (b) WDS compositional profile of $Ce_3(Co, Fe)_{11}B_4$ in layer 2; (c) WDS compositional profile of $Ce(Co, Fe)_{12}B_6$ in layer 3.

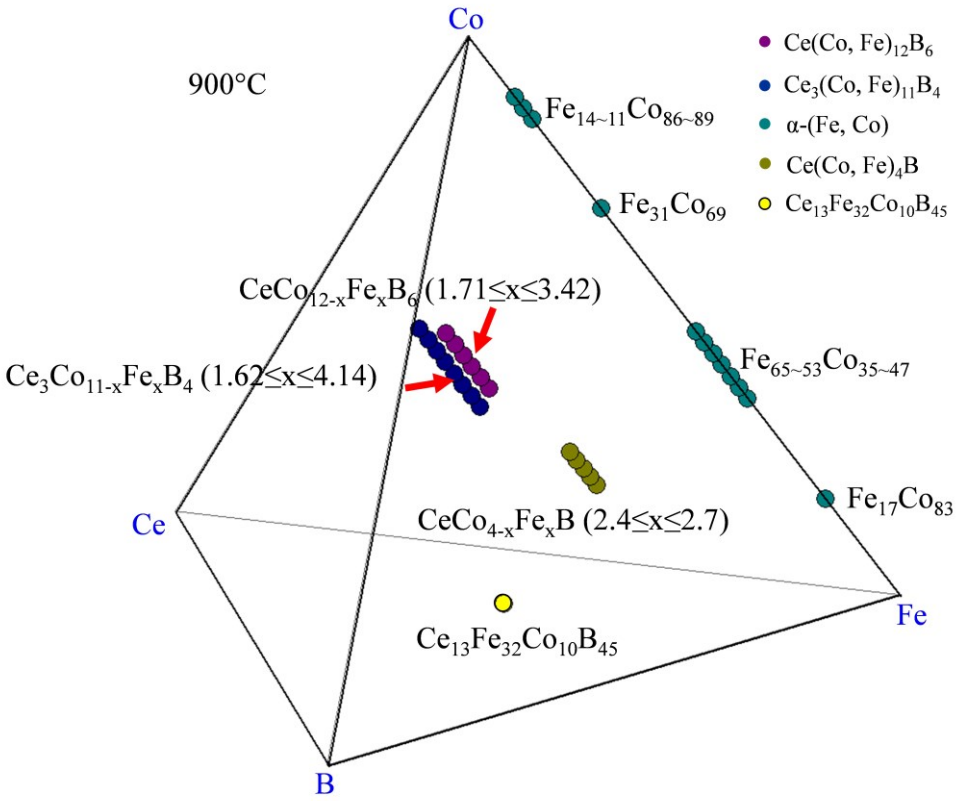
Co
900°C
Ce(Co, Fe)12B6
Ce3(Co, Fe)11B4
α-(Fe, Co)
Ce(Co, Fe)4B
Ce13Fe32Co10B45
Fe14~11Co86~89
Fe31Co69
CeCo12-xFexB6 (1.71≤x≤3.42)
Ce3Co11-xFexB4 (1.62≤x≤4.14)
Fe65~53Co35~47
Fe17Co83
Ce
CeCo4-xFexB (2.4≤x≤2.7)
Fe
Ce13Fe32Co10B45
B

(a)

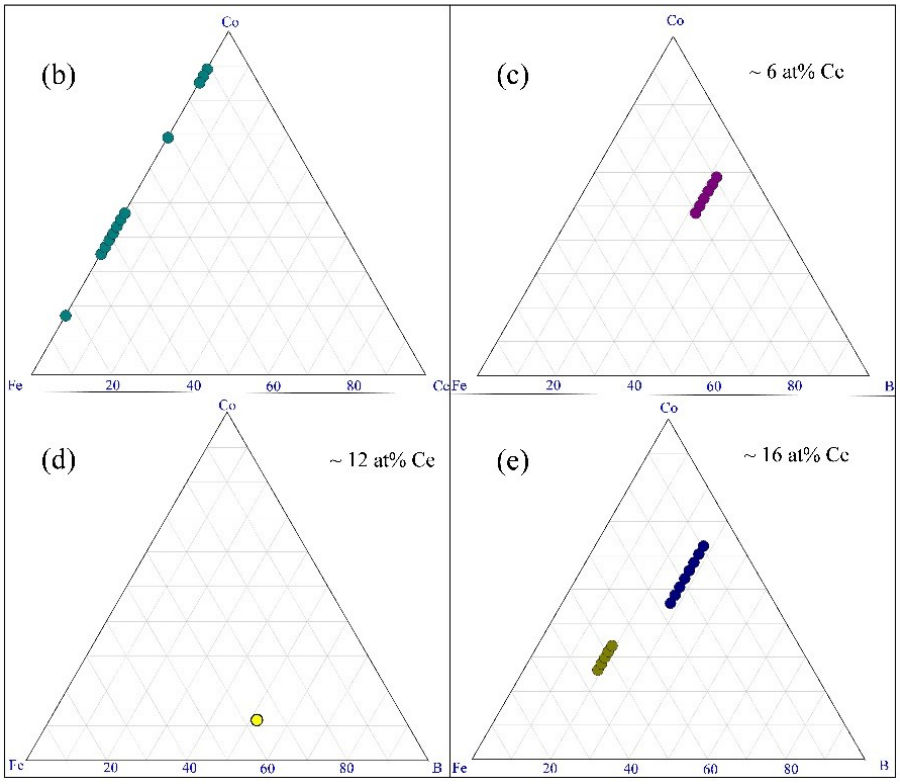
(b)
(c)
~ 6 at% Ce
(d)
~ 12 at% Ce
(e)
~ 16 at% Ce
Co
Fe
Ce
B
20
40
60
80

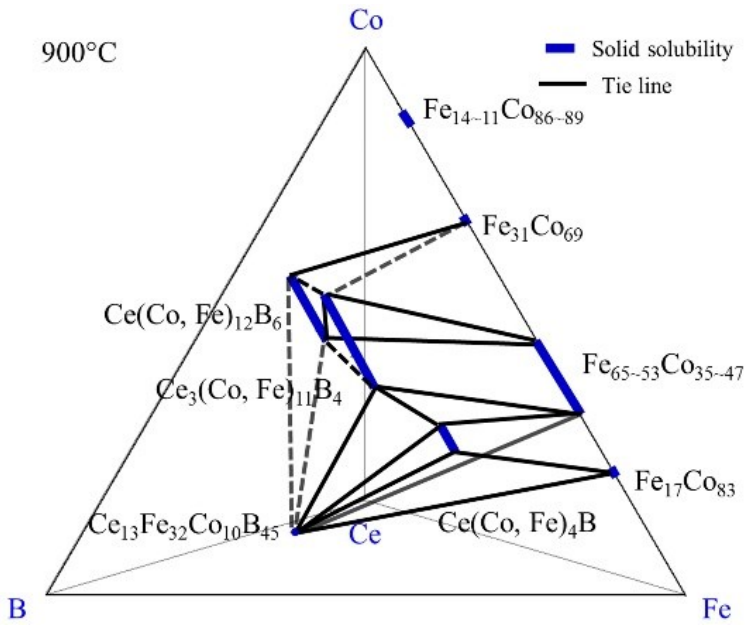

(f)

Figure 4.4. The results of the diffusion couple 4 at 900 °C: (a) 3D presentation of the experimental results; (b) Fe-Ce-Co ternary system; (c) pseudo ternary section at ~6 at. % Ce; (d) pseudo ternary section at ~12 at. % Ce; (e) pseudo ternary section at ~16 at. % Ce; (f) phase relations obtained from DC4.

By combining the results of all the diffusion couples, the detected phases in the Ce-Fe-Co-B system at 900 °C are plotted in Figure 4.5 (a). The phases present in the Fe-Co-Ce system are shown in Figure 4.5 (b). Three pseudo ternary sections at around 6 at. %, 12 at. %, and 16 at. % Ce are also shown in Figure 4.5 (c-e), respectively. So far, $Ce_2(Fe, Co)_{14}B$ was found to have solid solubility of 22 at. % Co and presented as $Ce_2Fe_{14-x}Co_xB$ ($0 \leq x \leq 3.78$). Solid solubility of $Ce(Co, Fe)_4B$ was measured from the diffusion couples. Further analysis has been performed using key alloys to measure its solubility limit and is discussed below. $Ce(Co, Fe)_{12}B_6$ and $Ce_3(Co, Fe)_{11}B_4$ were found to form in the Ce-Fe-Co-B system at 900 °C. They are denoted as $CeCo_{12-x}Fe_xB_6$ ($1.7 \leq x \leq 3.42$) and $Ce_3Co_{11-x}Fe_xB_4$ ($0.9 \leq x \leq 4.14$), respectively. Two solid solutions, namely, ε_1 and ε_2, with the same crystal structure, were found to form between Ce_2Co_{17} and Ce_2Fe_{17} in the Ce-Fe-Co ternary system at 900 °C, as shown in Figure 4.5 (a,b). Fujii et al. [75] studied the Ce-Fe-Co system and reported the $Ce_2Co_{13}Fe_4$ compound. Although this compound is not observed in the current work, its composition is very close to the solubility limit of ε_2 that has the $Ce_2Co_{13.4}Fe_{3.6}$

formula. Therefore, it could be that the compound reported in the work of Fujii et al. [75] refers to the solubility limit of ε_2.

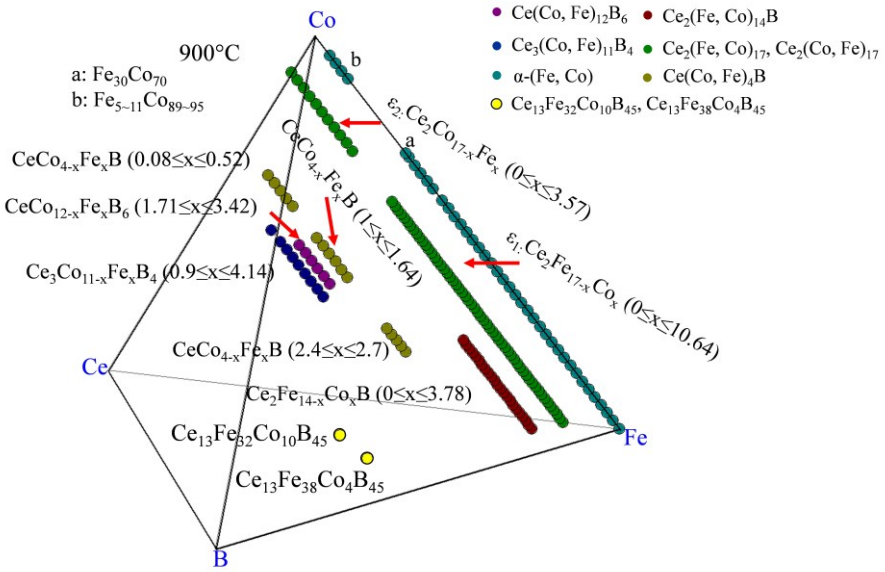

(a)

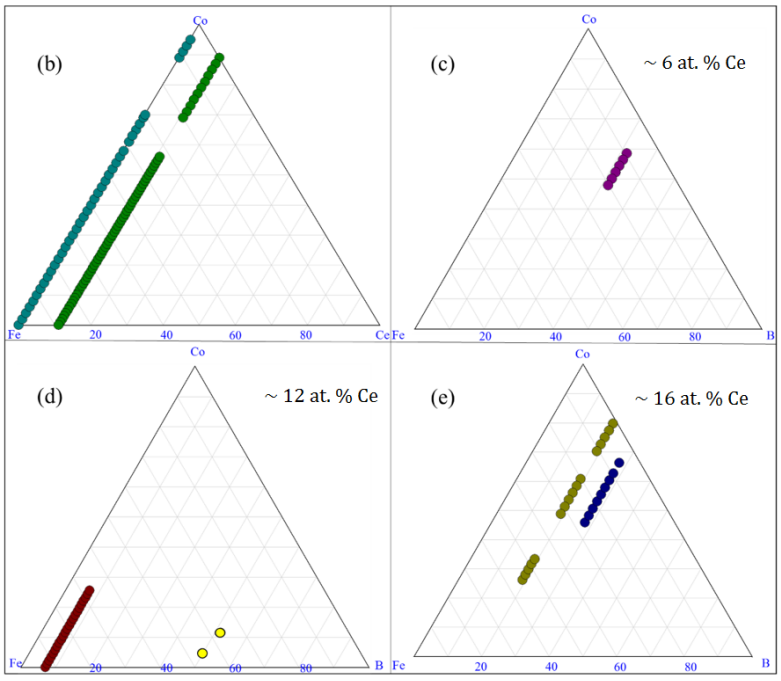

Figure 4.5. The diffusion couples results of the Ce-Fe-Co-B system at 900 °C: (a) 3D presentation of the experimental results; (b) Fe-Ce-Co ternary system; (c) pseudo ternary section at ~6 at. % Ce; (d) pseudo ternary section at ~12 at. % Ce; (e) pseudo ternary section at ~16 at. % Ce.

4.2 MFM study on diffusion couples

The strength of the near-surface stray fields is sensitive to the crystal orientation [109]. Since the investigated samples are non-oriented, various types of domain patterns are present. Diffusion layers of diffusion couple 1 were investigated using MFM. A stripe domain pattern of $Ce_2Fe_{14-x}Co_xB$ ($0 \leq x \leq 1.54$) in layer 1 was obtained and shown in Figure 4.6. Three tests were performed starting from the edge of layer 1 to the interface between layers 1 and 2. As presented in Figure 4.6, three MFM images positively indicate that $Ce_2Fe_{14-x}Co_xB$ ($0 \leq x \leq 1.54$) is magnetic along its homogeneity range. Figure 4.6 (c) shows the MFM image taken at the interface of layers 1 and 2. The magnetic domain pattern of $Ce_{12}Fe_{73}Co_9B_6$ ($Ce_2Fe_{14-x}Co_xB$ (x =1.54)) is shown on the left side of Figure 4.6 (c); strong magnetic contrast is detected. Comparatively, magnetic interaction of ε_1 was weak and no strong magnetic contrast can be seen on the right side of Figure 4.6 (c).

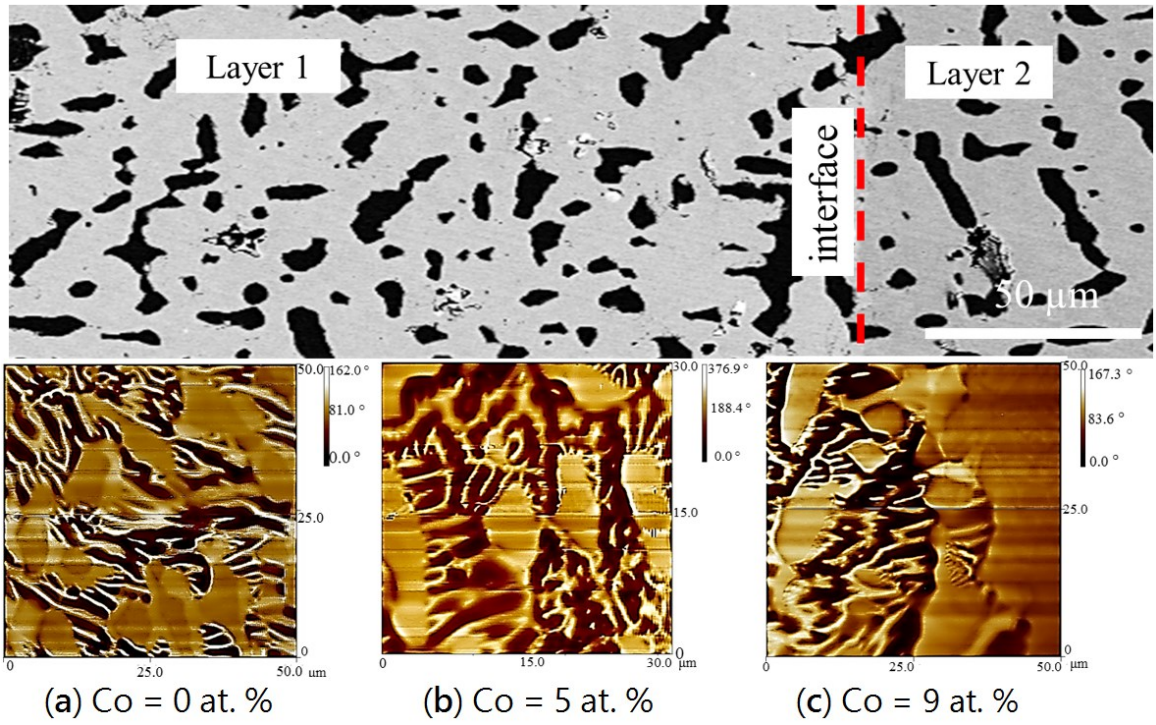

Figure 4.6. Microstructure (top) and three MFM images (a-c) obtained from layer 1 to the interface with layer 2 of DC1.

An MFM study was also performed on DC4. Two tests were selected to examine the regions of layers 1 and 2, and layers 2-4 as shown in Figure 4.7. From the MFM results illustrated in Figure 4.7 (a), magnetic contrasts of layers 2-4 were captured. On the left side, α-(Fe, Co) with the

$Fe_{31}Co_{69}$ composition is found to be magnetic and the stripe domain pattern is clearly observed. Also, $Ce(Co, Fe)_{12}B_6$ in layer 3 is non-magnetic, because no magnetic contrast can be seen in the MFM analysis. Figure 4.7 (b) is the MFM image at the interface between the end-member ($Ce_{15}Fe_{43}Co_{19}B_{23}$) and layer 2; stronger magnetic contrast was observed at the end-member side ($Ce(Co, Fe)_4B$), which has a mixture of stripe and closure magnetic domain patterns. Comparatively, a similar domain pattern is observed in layer 2 ($Ce_3(Co, Fe)_{11}B_4$), but the magnetic interaction is weaker. The boron-rich phase, $Ce_{13}Fe_{32}Co_{10}B_{45}$, in the end-member is non-magnetic.

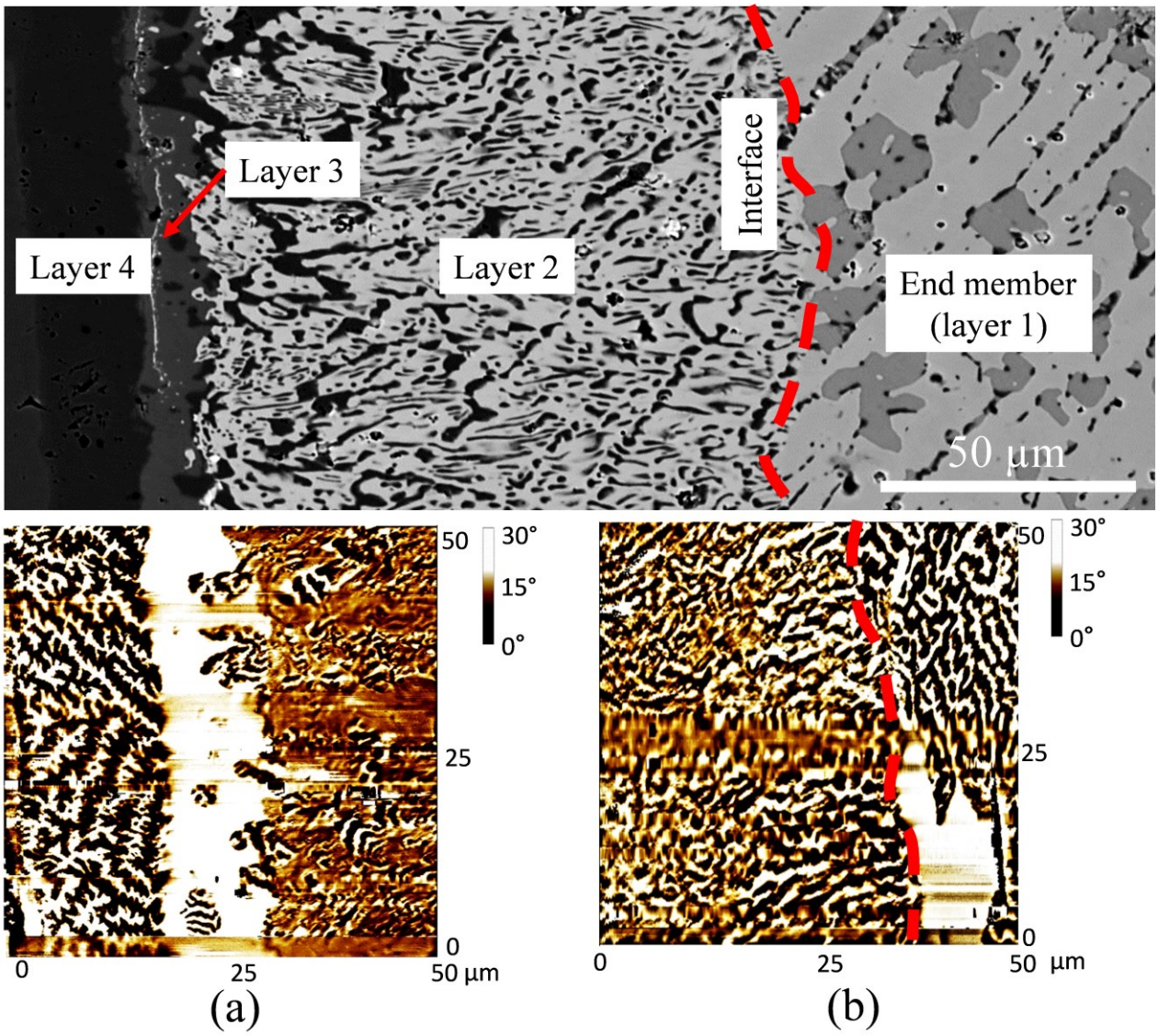

Figure 4.7. Microstructure (top) and two MFM images: (a) MFM test on layers 2-4 of DC4; (b) MFM test on the interface between layers 1 and 2 of DC4.

4.3 Key alloys study

4.3.1. Homogeneity ranges of $Ce_2(Fe, Co)_{14}B$ and $Ce(Co, Fe)_4B$

From diffusion couple studies, $Ce_2(Fe, Co)_{14}B$ and $Ce(Co, Fe)_4B$ exhibited extended solubility in the Ce-Fe-Co-B system at 900 °C. Eight key alloys were prepared along the homogeneity range of $Ce_2(Fe, Co)_{14}B$ by substituting a different amount of Fe with Co, as listed in Table 4.2. The actual global compositions of the samples were determined by EDS area mapping. Three maps were taken for each sample. The differences in the three scans were less than 2 at. % for all the elements. All key alloys were annealed at 900 °C for 25 days. Phase equilibria obtained from the key alloys are also presented in Table 4.2.

Table 4.2. Chemical composition of key alloys and detected phases.

Key Alloys Number	Actual Global Composition (at. %)				WDS Composition (at. %)				Corresponding Phases	
	Ce	Fe	Co	B	Ce	Fe	Co	B	By WDS	By XRD
KA 1	14	73	7	6	12	76	6	6	$Ce_2(Fe, Co)_{14}B$	$Ce_2(Fe, Co)_{14}B$
					13	39	3	45	$Ce_{13}Fe_{39}Co_3B_{45}$	N/A *
KA 2	15	66	12	7	12	71	11	6	$Ce_2(Fe, Co)_{14}B$	$Ce_2(Fe, Co)_{14}B$
					16	54	15	15	$Ce(Co, Fe)_4B$	$Ce(Co, Fe)_4B$
					36	41	23	0	CeFeCo	CeFeCo
KA 3	14	58	20	8	12	64	18	6	$Ce_2(Fe, Co)_{14}B$	$Ce_2(Fe, Co)_{14}B$
					16	46	23	15	$Ce(Co, Fe)_4B$	$Ce(Co, Fe)_4B$
					0	86	14	0	α-(Fe, Co)	α-(Fe, Co)
KA 4	15	54	24	7	12	60	22	6	$Ce_2(Fe, Co)_{14}B$	$Ce_2(Fe, Co)_{14}B$
					16	40	28	16	$Ce(Co, Fe)_4B$	$Ce(Co, Fe)_4B$
					0	80	20	0	α-(Fe, Co)	α-(Fe, Co)
KA 5	14	46	32	8	12	54	28	6	$Ce_2(Fe, Co)_{14}B$	$Ce_2(Fe, Co)_{14}B$
					16	33	35	16	$Ce(Co, Fe)_4B$	$Ce(Co, Fe)_4B$
					0	76	24	0	α-(Fe, Co)	α-(Fe, Co)
KA 6	12	42	40	6	11	48	41	0	$Ce_2(Fe, Co)_{17}$	$Ce_2(Fe, Co)_{17}$
					16	23	45	16	$Ce(Co, Fe)_4B$	$Ce(Co, Fe)_4B$
					0	66	34	0	α-(Fe, Co)	α-(Fe, Co)
KA 7	12	32	50	6	11	37	52	0	$Ce_2(Fe, Co)_{17}$	$Ce_2(Fe, Co)_{17}$
					17	13	54	16	$Ce(Co, Fe)_4B$	$Ce(Co, Fe)_4B$
					0	57	43	0	α-(Fe, Co)	α-(Fe, Co)
KA 8	12	22	60	6	11	24	65	0	$Ce_2(Fe, Co)_{17}$	$Ce_2(Fe, Co)_{17}$

	17	7	60	16	$Ce(Co, Fe)_4B$	$Ce(Co, Fe)_4B$
	0	56	44	0	α-(Fe, Co)	α-(Fe, Co)

* Not available: Unknown crystal structure which could not be confirmed by XRD.

Two phases formed in KA 1 ($Ce_{14}Fe_{73}Co_7B_6$) after annealing at 900 °C for 25 days, as shown in Figure 4.8 (a). The solid solubility of the dominating $Ce_2(Fe, Co)_{14}B$ was measured as 6 at. % Co. A boron-rich compound ($Ce_{13}Fe_{39}Co_3B_{45}$) with similar chemical composition to what was found in the diffusion-couple study is also observed in this key alloy. From the MFM test, as presented in Figure 4.8 (b), dominating stripe magnetic domain patterns with some dispersed non-magnetic plates were observed. Comparing the phase morphology between SEM and MFM images, it is concluded that the dominating is the $Ce_2(Fe, Co)_{14}B$ magnetic phase, and non-magnetic regions belong to $Ce_{13}Fe_{39}Co_3B_{45}$. In Figure 4.8 (c), $Ce_2(Fe, Co)_{14}B$ is positively identified in the XRD pattern of KA 1. However, the crystal structure prototype of $Ce_{13}Fe_{39}Co_3B_{45}$ has not been reported in the literature, hence this compound cannot be verified by XRD analysis. A number of unlabeled peaks, marked by "?" in Figure 4.8 (c), may belong to $Ce_{13}Fe_{39}Co_3B_{45}$.

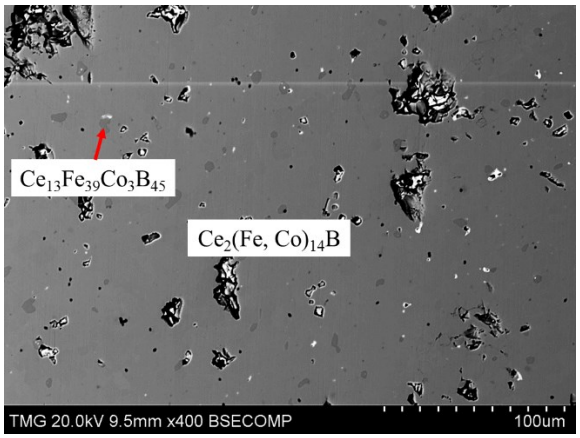

(a)

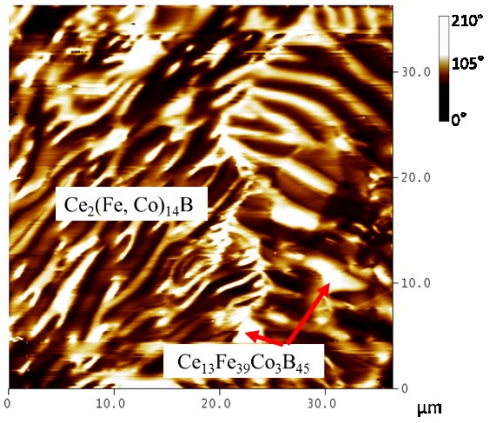

(b)

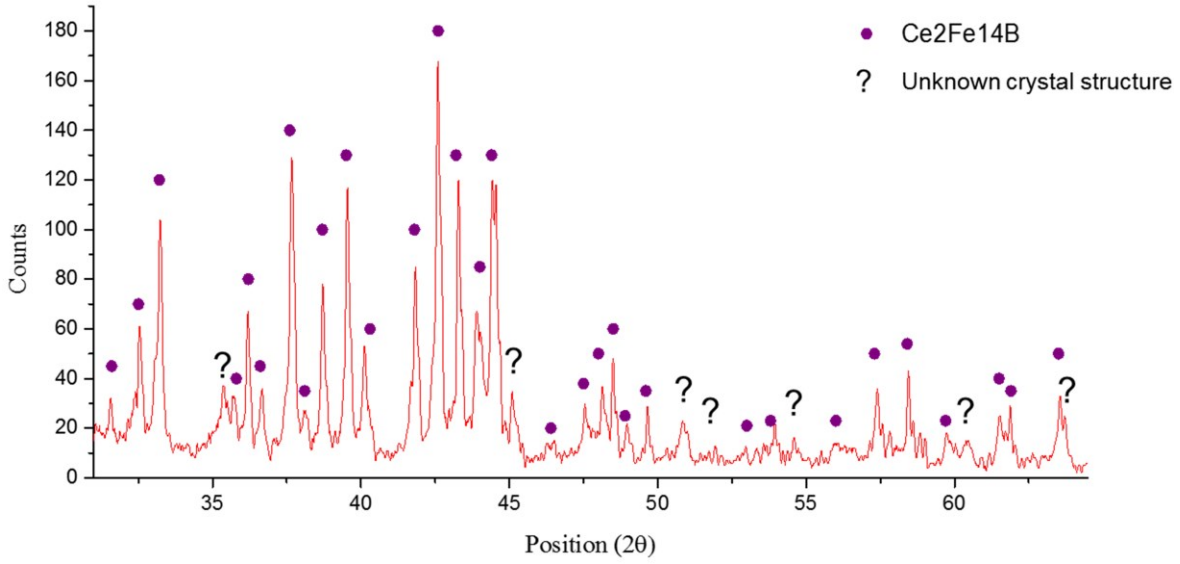

(c)

Figure 4.8. (a) BSE image of KA 1; (b) MFM image of KA 1; (c) XRD spectrum of KA 1.

When the concentration of Co in the global composition increased from 7 at. % in KA 1–12 at. % in KA 2, three-phase equilibrium between $Ce_2(Fe, Co)_{14}B$, $Ce(Co, Fe)_4B$, and CeFeCo occurred, as shown in Figure 4.9 (a). Unlike in KA 1, the boron-rich phase is not observed in KA 2. Instead, a limited quantity of $Ce(Co, Fe)_4B$ started to form when the Co content was increased. XRD analysis also confirmed the phase constituents, as shown in Figure 4.9 (c). The solid solubility limit of $Ce(Co, Fe)_4B$ was measured as 54 at. % Fe, which can be considered as the maximum solid solubility of this phase in the Ce-Fe-Co-B system at 900 °C. In the MFM image, as shown in Figure 4.9 (b), it is clear that the magnetic domain pattern corresponds to the dominating $Ce_2(Fe, Co)_{14}B$. However, $Ce(Co, Fe)_4B$ cannot be easily distinguished from this image, which could be due to its relatively small amount. Another possibility is that $Ce(Co, Fe)_4B$ and $Ce_2(Fe, Co)_{14}B$ have a similar magnetic domain pattern, which makes it difficult to distinguish them from each other. By comparing the morphology of CeFeCo in Figure 4.9 (a) with non-magnetic islands in Figure 4.9 (b), this non-magnetic phase belongs to the CeFeCo compound.

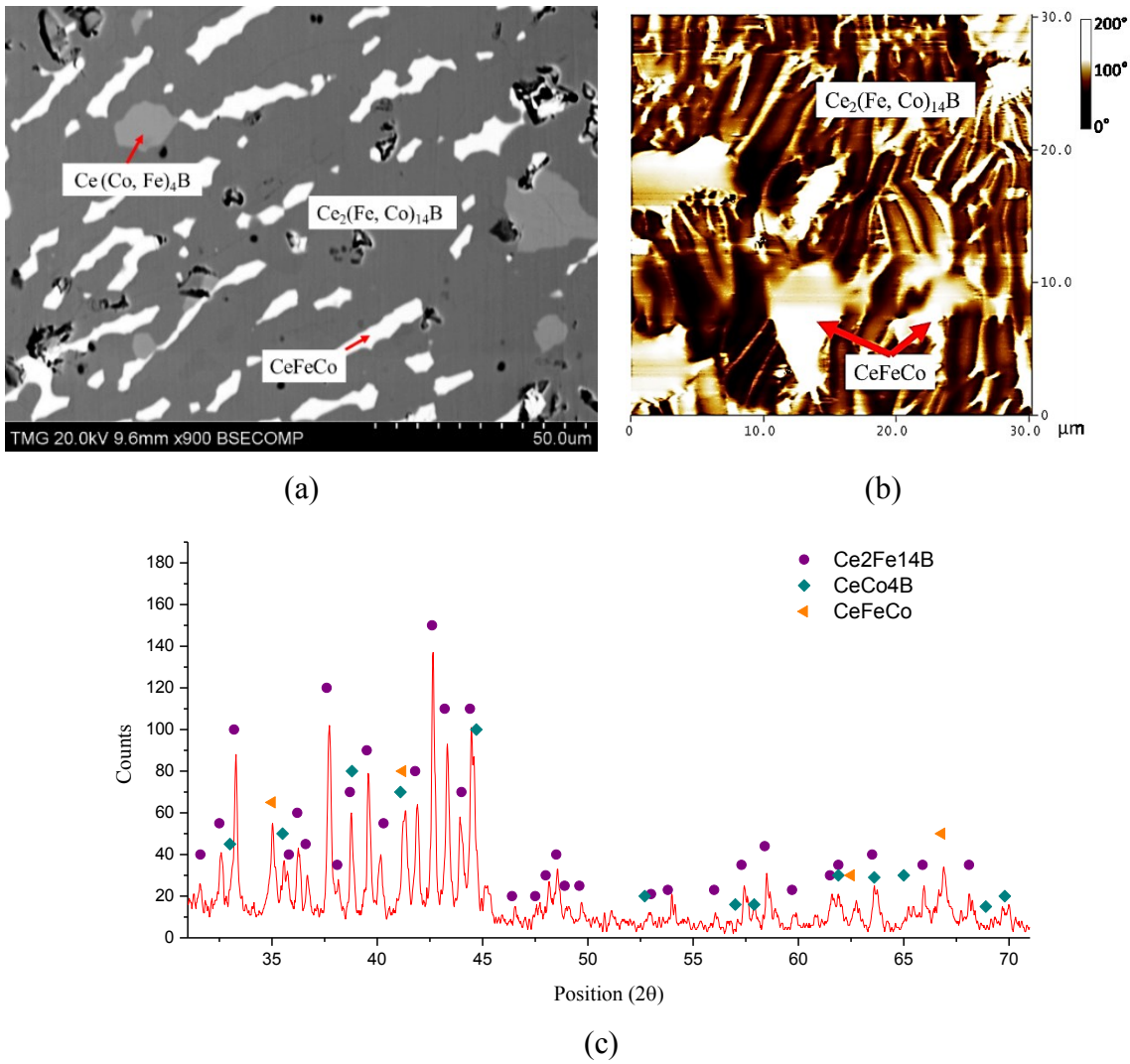

Figure 4.9. (a) BSE image of KA 2; (b) MFM image of KA 2; (c) XRD spectrum of KA 2.

$Ce_2(Fe, Co)_{14}B$ formed through peritectic solidification. Due to the sluggish kinetics of the peritectic reaction, the transformation of α-(Fe, Co) and CeFeCo to $Ce_2(Fe, Co)_{14}B$ and $Ce(Co, Fe)_4B$ takes a very long time. Therefore, two-phase equilibrium was established between $Ce_2(Fe, Co)_{14}B$ and $Ce(Co, Fe)_4B$ in KAs 3, 4, and 5. In KA 3, Co dissolved in $Ce_2Fe_{14}B$ was measured as 18 at. %. With global Co concentrations increased in KAs 4 and 5, the solid solubility of Co in $Ce_2Fe_{14}B$ was also further extended. Dominating $Ce_2(Fe, Co)_{14}B$ was found in KA 4 ($Ce_{15}Fe_{54}Co_{24}B_7$), as shown in Figure 4.10 (a). Solid solubility of $Ce_2(Fe, Co)_{14}B$ was measured as 22 at. % Co, which is consistent with the results obtained from DC2. However, with an increase in Co content to 32 at. % in KA 5 ($Ce_{14}Fe_{46}Co_{32}B_8$), $Ce_2(Fe, Co)_{14}B$ was still found to form in this alloy, and solid solubility was measured as 28 at. % Co. The BSE image of KA 5 is presented in

Figure 4.10 (b). Magnetic domains of $Ce_2(Fe, Co)_{14}B$ can still be observed in both samples based on the MFM study, as can be seen in Figure 4.10 (c). KAs 6, 7, and 8 were prepared in the Co-rich region. The compositions of the detected phases are listed in Table 2. When Co content in KA 6 ($Ce_{12}Fe_{42}Co_{40}B_6$) reached 40 at. %, the $Ce_2(Fe, Co)_{14}B$ phase disappeared. Whereas, $Ce(Co, Fe)_4B$ became the dominating phase and $Ce_2(Co, Fe)_{17}$ started to form in KA 6. KAs 7 and 8 confirmed the phase equilibria obtained from KA 6. In the XRD spectrum of KA 6 in Figure 4.11 (c), all three phases were confirmed by XRD. Three-phase regions $Ce(Co, Fe)_4B$, α-(Fe, Co), and $Ce_2(Co, Fe)_{17}$ were established from these samples, as presented in Figure 4.12 (e). Moreover, the dominating $Ce(Co, Fe)_4B$ was found to be magnetic, as shown in Figure 4.11 (b). Compared to the MFM images of the $Ce_2(Fe, Co)_{14}B$ phase in KAs 1-5, the magnetic contrast of $Ce(Co, Fe)_4B$ is significantly lower. The magnetic contrast of $Ce(Co, Fe)_4B$ in Figure 4.11 (b) is in the range of 0-40 degree; whereas, the magnetic contrast of $Ce_2(Fe, Co)_{14}B$ in KAs 1-5 is in the range of 0-180 degrees or higher. This indicates that the magnetization of $Ce(Co, Fe)_4B$ is weaker than that of $Ce_2(Fe, Co)_{14}B$. In KA 6, there is a number of weaker closure domain patterns at the top and middle of Figure 4.11 (b), which belong to $Ce_2(Co, Fe)_{17}$. The non-magnetic regions were considered as α-(Fe, Co) which were consistent with the MFM studies of other key alloys. The MFM results are only presented here as indications of the effect of composition on the magnetic domains.

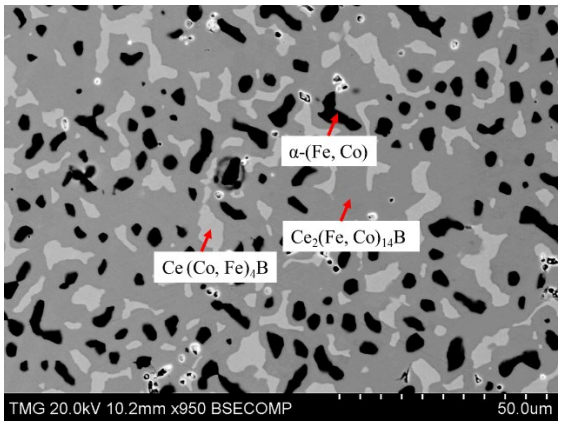

(a)

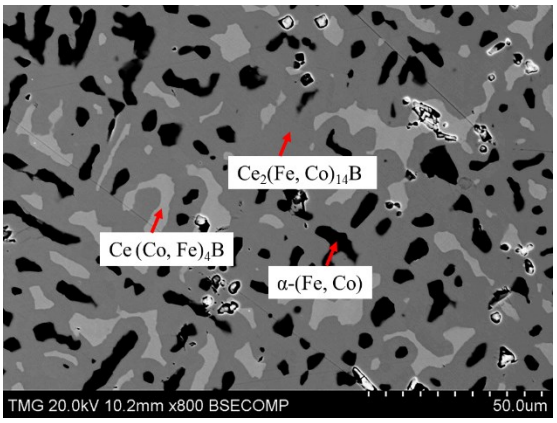

(b)

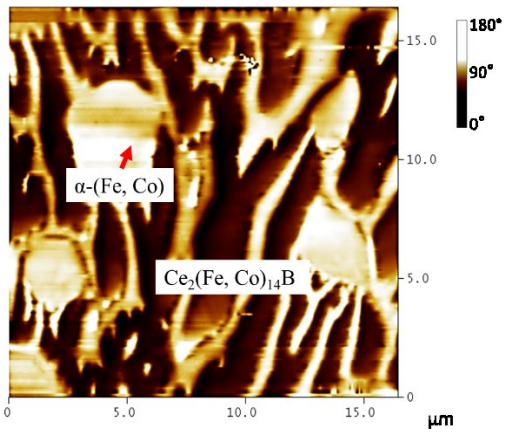

(c)

Figure 4.10. (a) BSE image of KA 4; (b) BSE image of KA 5; (c) MFM image of KA 5.

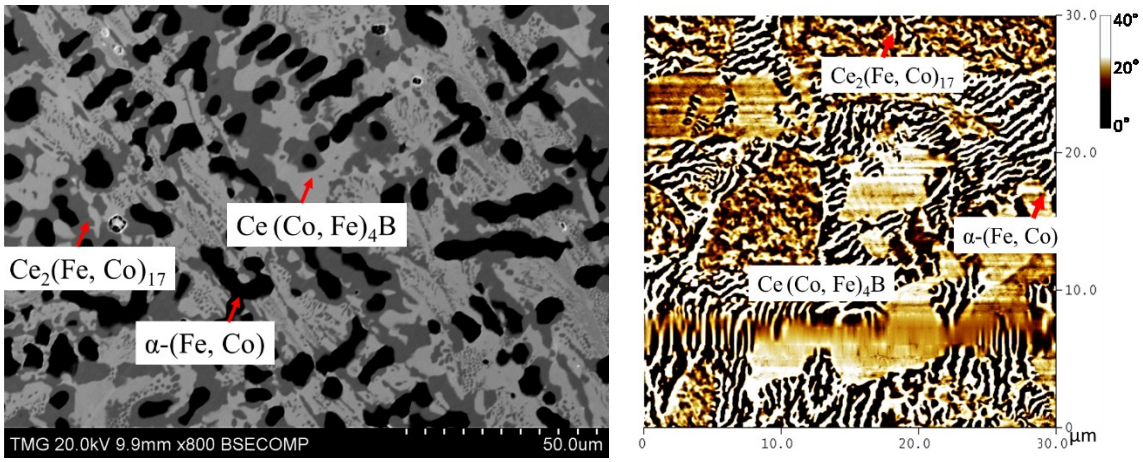

(a) (b)

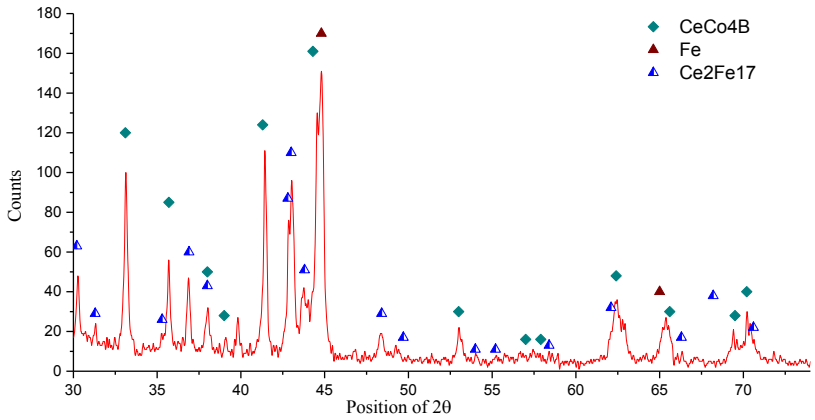

(c)

Figure 4.11. (a) BSE image of KA 6; (b) MFM image of KA 6; (c) XRD spectrum of KA 6.

From the key alloys study, the solubility limits of $Ce_2(Fe, Co)_{14}B$ and $Ce(Co, Fe)_4B$ were measured as 28 at. % Co and 54 at. % Fe, respectively. They are presented by $Ce_2Fe_{14-x}Co_xB$ ($1.02 \leq x \leq 4.76$) and $CeCo_{4-x}Fe_xB$ ($0.42 \leq x \leq 3.18$) formulae. The experimental results of eight key alloys are summarized in Figure 4.12 (a). Solid solubility of ε_1 ($Ce_2(Fe, Co)_{17}$) observed in the diffusion couples was confirmed by key alloys 6, 7, and 8. The Co dissolved in ε_1 was found to extend further, up to 65 at. % in $Ce_2(Fe, Co)_{17}$, as presented by the $Ce_2Fe_{17-x}Co_x$ ($7.79 \leq x \leq 12.35$) formula and shown in Figure 4.12. In the current study, it is found that $Ce(Co, Fe)_4B$ only formed in an Fe-rich region when Co content is greater than 10 at. %. When Co content is below 10 at. %, the boron-rich phase, $Ce_{13}Fe_{39}Co_3B_{45}$, started to form. Moreover, $Ce(Co, Fe)_4B$ might be a weaker magnetic phase compared to $Ce_2(Fe, Co)_{14}B$, based on the MFM results. The phases formed in the Fe-Co-Ce system are presented in Figure 4.12 (b). Two pseudo ternary sections at 12 at. % and 16 at. % Ce were used to demonstrate the locations of $Ce_2(Fe, Co)_{14}B$, and $Ce(Co, Fe)_4B$, respectively, which can be seen in Figure 4.12 (c,d). The phase equilibria obtained from eight key alloys are presented in Figure 4.12 (e). The dotted lines indicate the possible phase equilibria between the detected phases. Two three-phase equilibria ($Ce_2(Fe, Co)_{14}B$/$Ce(Co, Fe)_4B$/CeFeCo and $Ce(Co, Fe)_4B$/α-(Fe, Co)/$Ce_2(Fe, Co)_{17}$) were established.

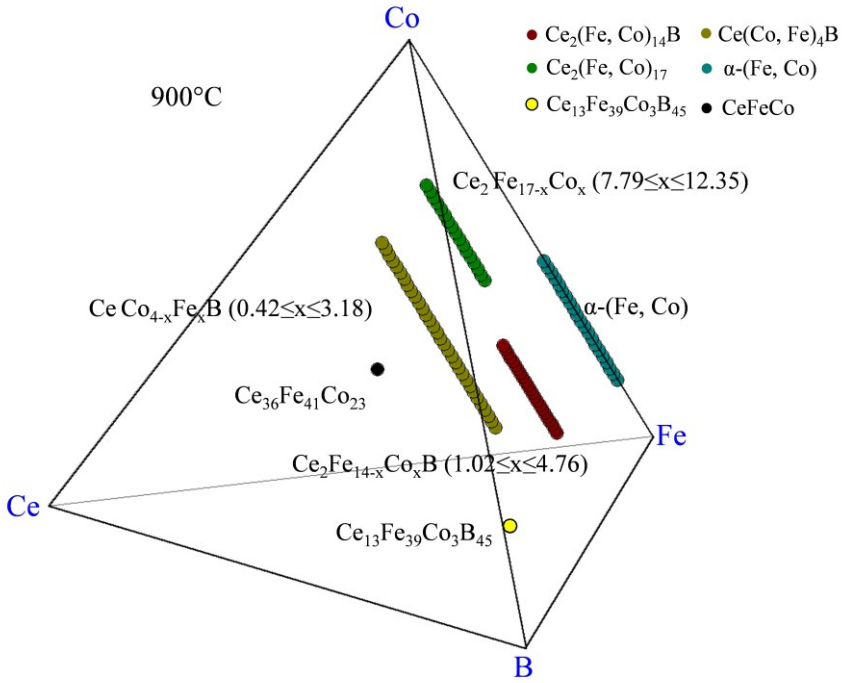

(a)

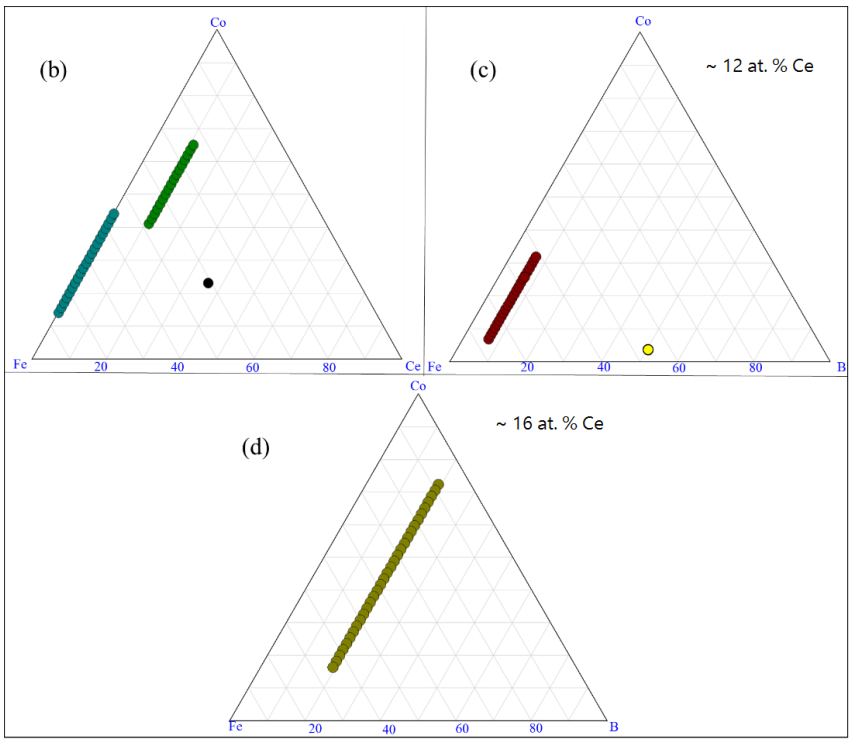

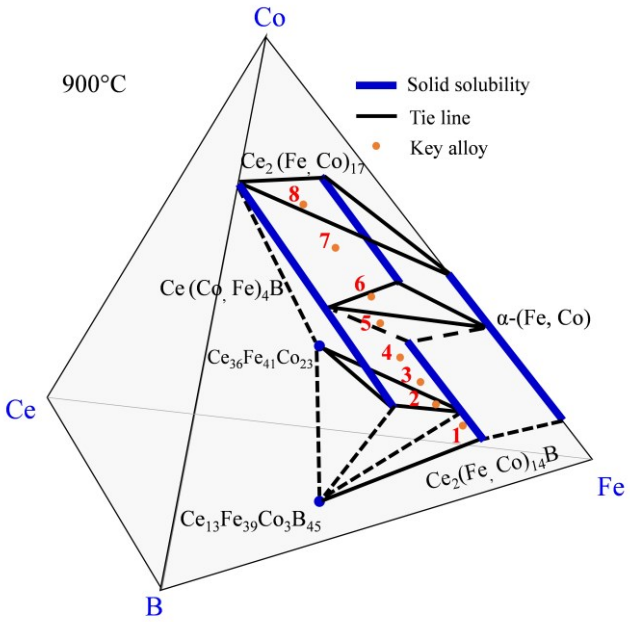

(e)

Figure 4.12. Homogeneity ranges of $Ce_2(Fe, Co)_{14}B$, and $Ce(Co, Fe)_4B$ obtained from key alloys: (a) 3D presentation of the experimental results; (b) Fe-Ce-Co ternary system; (c) pseudo ternary section at ~12 at. % Ce; (d) pseudo ternary section at ~16 at. % Ce; (e) phase relations obtained from KAs 1-8.

$Ce_2(Fe, Co)_{14}B$ forms a substitutional solid solution in this quaternary system, where Co substitutes for Fe atoms, while Ce and B contents remain constant as 12 at. % and 6 at. %, respectively. The maximum solid solubility of $Ce_2(Fe, Co)_{14}B$ has been determined by SEM/WDS as 28 at. % Co in KA 5 at 900 °C. All XRD data has shown that this solid solution, in KAs 1-5, crystallized in a tetragonal structure with a *P42/mnm* (68) space group and an $Nd_2Fe_{14}B$ prototype. Figure 4.13 shows the cell parameters variations with Co concentration in the selected key alloys. The peak positions shift to a higher angle with increasing Co content. The substitution of Fe with Co, which has a smaller atomic radius, decreases the unit cell parameters and lattice volume. This is confirmed by the increase in 2θ values of the peak positions from KAs 1-5 due to the increasing Co concentration. The linear relation between the lattice parameters, lattice volume, and Co concentration obey Vegard's law [110] as plotted in Figure 4.13, indicating clearly the occurrence of substitutional solid solubility in the $Ce_2(Fe, Co)_{14}B$,.

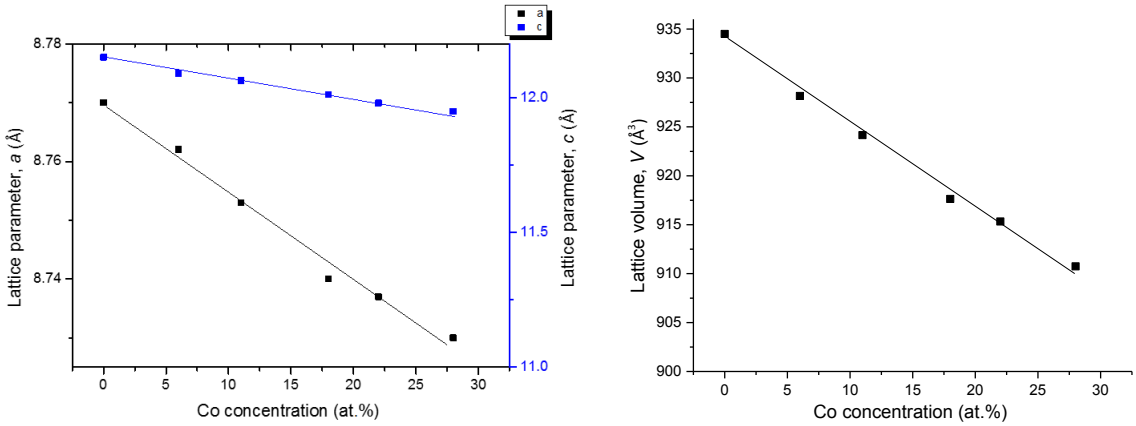

(a) (b)

Figure 4.13. Cell parameters *a* and *c* (a) and lattice volume *V* (b) with Co concentration for the $Ce_2(Fe, Co)_{14}B$ from KAs 1-5.

The unit cell parameters of $Ce(Co, Fe)_4B$ from KAs 2-6 are plotted in Figure 4.14. Similar to $Ce_2(Fe, Co)_{14}B$, $CeCo_4B$ also forms a substitutional solid solution in this quaternary system, while Ce and B contents remain constant as 16 at. % and 17 at. %, respectively. The substitution of Co with Fe, which has a larger atomic radius, increases the unit cell parameters. Cell lengths *a* and *c* reach maximum when $CeCo_4B$ has the maximum quaternary solid solution of 54 at. % Fe in KA 2 at 900 °C. When Fe content in $CeCo_4B$ is reduced, the cell parameters are also decreased. This is confirmed by the increase in the 2θ values of the peaks positions from the KAs 2-8 due to

the decreases in the Fe concentration. The XRD results have demonstrated that Ce(Co, Fe)$_4$B crystallized in a hexagonal structure with a *P6/mnm* (191) space group and a CeCo$_4$B prototype. The linear relation between the lattice parameters, lattice volume, and Co concentration obey Vegard's law [110], indicating again the occurrence of substitution solid solubility in the Ce(Co, Fe)$_4$B, as plotted in Figure 4.14.

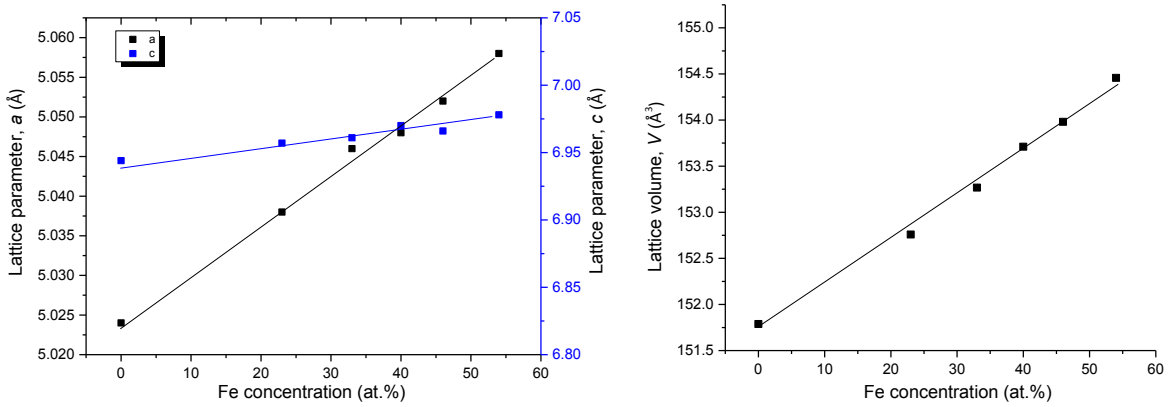

(a) (b)

Figure 4.14. Cell parameters *a* and *c* (a) and lattice volume *V* (b) with Co concentration for the Ce(Co, Fe)$_4$B from KAs 2-6.

4.3.2. Homogeneity ranges of Ce(Co, Fe)$_{12}$B$_6$ and Ce$_3$(Co, Fe)$_{11}$B$_4$

Solid solubilities of Ce(Co, Fe)$_{12}$B$_6$ and Ce$_3$(Co, Fe)$_{11}$B$_4$ were measured as 18 at. % Fe and 23 at. % Fe at 900 °C from the diffusion couple analysis. Seven key alloys were designed to verify the results obtained from the diffusion couples and determine the solubility limits of these two phases in the Ce-Fe-Co-B system at 900 °C. The chemical compositions of the key alloys prepared for this purpose are listed in Table 4.3. Phase equilibria determined from these key alloys are also summarized in Table 4.3. The actual global compositions of the samples were determined by EDS area mapping. Three maps were taken for each sample, and the differences in three scans were less than 2 at. % for all the elements.

Table 4.3. Chemical composition of key alloys and detected phases.

Key Alloys Number	Actual Global Composition (at. %)				WDS Composition (at. %)				Corresponding Phases	
	Ce	Fe	Co	B	Ce	Fe	Co	B	By WDS	By XRD
KA 9	9	7	56	28	6	4	60	30	$Ce(Co, Fe)_{12}B_6$	$Ce(Co, Fe)_{12}B_6$
					0	16	63	21	$Fe_{16}Co_{63}B_{21}$	N/A *
KA 10	16	8	51	25	17	5	55	23	$Ce_3(Co, Fe)_{11}B_4$	$Ce_3(Co, Fe)_{11}B_4$
					6	14	51	29	$Ce(Co, Fe)_{12}B_6$	$Ce(Co, Fe)_{12}B_6$
KA 11	17	18	43	22	17	14	46	23	$Ce_3(Co, Fe)_{11}B_4$	$Ce_3(Co, Fe)_{11}B_4$
					6	32	32	30	$Ce(Co, Fe)_{12}B_6$	$Ce(Co, Fe)_{12}B_6$
KA 12	17	33	27	23	17	28	32	23	$Ce_3(Co, Fe)_{11}B_4$	$Ce_3(Co, Fe)_{11}B_4$
					6	46	18	30	$Ce(Co, Fe)_{12}B_6$	$Ce(Co, Fe)_{12}B_6$
					17	39	27	17	$Ce(Co, Fe)_4B$	$Ce(Co, Fe)_4B$
KA 13	17	42	18	23	17	37	23	23	$Ce_3(Co, Fe)_{11}B_4$	$Ce_3(Co, Fe)_{11}B_4$
					16	47	20	17	$Ce(Co, Fe)_4B$	$Ce(Co, Fe)_4B$
					13	34	8	45	$Ce_{13}Fe_{34}Co_8B_{45}$	N/A *
KA 14	17	50	10	23	16	55	12	17	$Ce(Co, Fe)_4B$	$Ce(Co, Fe)_4B$
					13	37	5	45	$Ce_{13}Fe_{37}Co_5B_{45}$	N/A *
					35	45	20	0	CeFeCo	CeFeCo
KA 15	15	20	49	16	17	16	44	23	$Ce_3(Co, Fe)_{11}B_4$	$Ce_3(Co, Fe)_{11}B_4$
					16	26	42	16	$Ce(Co, Fe)_4B$	$Ce(Co, Fe)_4B$
					0	68	32	0	α-(Fe, Co)	α-(Fe, Co)
KA 16	16	46	9	29	16	47	19	18	$Ce(Co, Fe)_4B$	$Ce(Co, Fe)_4B$
					13	38	4	45	$Ce_{13}Fe_{38}Co_4B_{45}$	N/A *
					34	44	22	0	CeFeCo	CeFeCo
KA 17	15	43	19	23	17	44	22	17	$Ce(Co, Fe)_4B$	$Ce(Co, Fe)_4B$
					13	34	8	45	$Ce_{13}Fe_{34}Co_8B_{45}$	N/A *
					0	42	58	0	α-(Fe, Co)	α-(Fe, Co)

* Not available: Unknown crystal structure which could not be confirmed by XRD.

$Ce(Co, Fe)_{12}B_6$ was first found in the diffusion couple study and the homogeneity range was measured as 9-18 at. % Fe. KA 9 was prepared in the Co-rich side with $Ce_6Fe_6Co_{58}B_{30}$ chemical composition. After annealing at 900 °C for 25 days, the dominating $Ce(Co, Fe)_{12}B_6$ was obtained and some precipitates with $Fe_{16}Co_{63}B_{21}$ chemical composition were also observed, as shown in Figure 4.15 (a). Fe dissolved in $CeCo_{12}B_6$ was determined as 4 at. %. From the MFM image in

Figure 4.15 (b), the dominating phase was found to be non-magnetic, which is also consistent with the MFM result of DC4. The magnetic domain found in this image belongs to $Fe_{16}Co_{63}B_{21}$. Based on the XRD analysis shown in Figure 4.15 (c), the dominating $Ce(Co, Fe)_{12}B_6$ phase is positively identified. However, the crystal structure prototype of $Fe_{16}Co_{63}B_{21}$ is not available in the literature. Therefore, this phase cannot be verified by XRD analysis. Moreover, there are some unlabeled peaks, marked with "?" in Figure 4.15 (c), which may belong to $Fe_{16}Co_{63}B_{21}$.

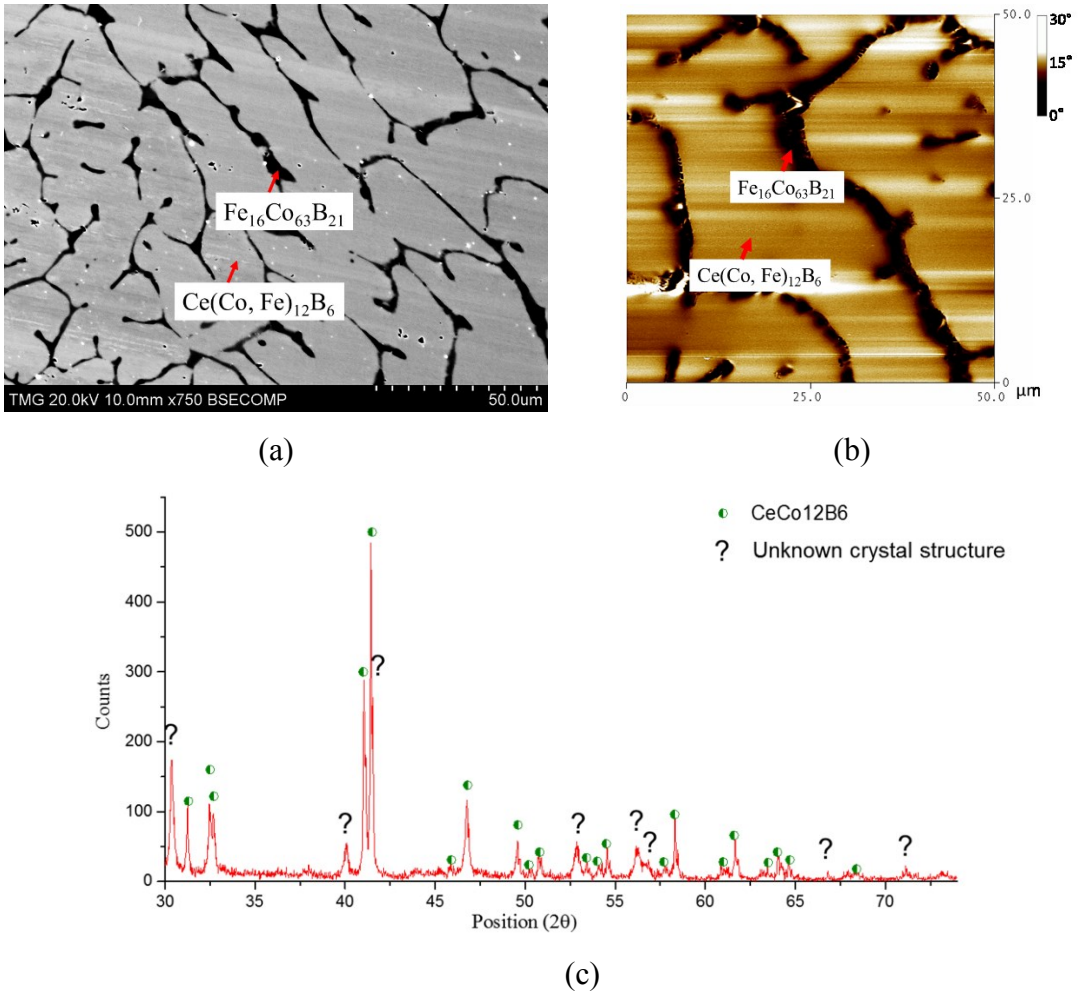

Figure 4.15. (a) BSE image of KA 9; (b) MFM image of KA 9; (c) XRD spectrum of KA 9.

KAs 10-14 were selected to measure the maximum solid solubility of $Ce(Co, Fe)_{12}B_6$ and $Ce_3(Co, Fe)_{11}B_4$. These five key alloys were prepared along the homogeneity range of $Ce_3(Co, Fe)_{11}B_4$ by substituting a different amount of Fe with Co, which were presented by the formulae $Ce_3Co_{11-x}Fe_xB_4$ with x varying as 1.44, 3.24, 5.94, 7.38, and 9.00. The phase relations between $Ce_3(Co, Fe)_{11}B_4$, $Ce(Co, Fe)_{12}B_6$, and $Ce(Co, Fe)_4B$ were investigated. As shown in Figure 4.16

(a), two-phase equilibrium between $Ce_3(Co, Fe)_{11}B_4$ and $Ce(Co, Fe)_{12}B_6$ was established from KA 11. Phase relations obtained from key alloys are summarized in Figure 4.18 (d). The dominating $Ce_3(Co, Fe)_{11}B_4$ phase was identified and the black precipitates in Figure 4.16 (a) were found to be $Ce(Co, Fe)_{12}B_6$. When the global Fe concentration in KA 12 was increased to 33 at. %, a small amount of the $Ce(Co, Fe)_4B$ phase appeared, as can be seen in Figure 4.16 (b). Fe dissolved in $Ce_3(Co, Fe)_{11}B_4$ and $Ce(Co, Fe)_{12}B_6$ was measured as 28 at. % and 46 at. %, respectively. The detected phases were all confirmed by XRD, as presented in Figure 4.16 (g). As Fe content reached 42 at. % in KA 13, $Ce(Co, Fe)_{12}B_6$ disappeared and $Ce(Co, Fe)_4B$ became the dominating phase, along with a limited amount of $Ce_3(Co, Fe)_{11}B_4$.

When Fe content was increased to 50 at. % in KA 14, $Ce_3(Co, Fe)_{11}B_4$ completely disappeared and three-phase equilibrium $Ce(Co, Fe)_4B$, $Ce_{13}Fe_{37}Co_5B_{45}$, and CeFeCo was established. Maximum solid solubility of $Ce_3(Co, Fe)_{11}B_4$ was measured as 37 at. % Fe in KA 13. From the MFM results, as shown in Figure 4.16 (e, f), a mixture of stripe and closure domain patterns is observed, indicating that the dominating $Ce_3(Co, Fe)_{11}B_4$ dissolving 14 at. % Fe and 28 at. % Fe, respectively, is a magnetic phase. Magnetic $Ce_3(Co, Fe)_{11}B_4$ was first found in DC4, and is now confirmed by the MFM study of the key alloys. The substitution of Co with Fe in $Ce_3(Co, Fe)_{11}B_4$ is also studied by XRD. Compared to Co, Fe has a larger atomic radius, which increases the unit cell volume. As can be seen in Figure 4.17, cell length *a* and lattice volume *V* reach maximum when $Ce_3(Co, Fe)_{11}B_4$ has the maximum quaternary solid solubility of 37 at.% Fe in KA 13 at 900 °C. However, when Fe concentration in $Ce_3(Co, Fe)_{11}B_4$ was increased, the cell parameter *c* decreased to some extent. Nevertheless, the volume of the unit cell increased with Fe content, indicating the overall effect of larger atom substitution. The XRD results have demonstrated that $Ce_3(Co, Fe)_{11}B_4$ crystallizes in a hexagonal structure with a *P6/mnm* (191) space group and a $Ce_3Co_{11}B_4$ prototype. The linear relation between the lattice parameters, lattice volume, and Co concentration indicates the occurrence of substitution solid solubility, according to Vegard's law [110], as shown in Figure 4.17.

In KAs 13, 14, 16, and 17, a boron-rich phase with $Ce_{13}Fe_{34\sim38}Co_{4\sim8}B_{45}$ chemical composition was identified. This phase was first observed in DCs 3 and 4, with $Ce_{13}Fe_{38}Co_4B_{45}$ and $Ce_{13}Fe_{32}Co_{10}B_{45}$ composition, respectively. Similar results were also obtained from KA 1, but with $Ce_{13}Fe_{39}Co_3B_{45}$ composition. Analyzing these compositions reveals that Ce and B contents are consistent and the compositional difference was due to Fe/Co atomic exchange. Moreover, the

unidentified peaks in the XRD spectra of KAs 1, 13, 14, 16, and 17 were repeatable, but no reported crystal structure prototype could be found for this phase. Thus, we consider this boron-rich phase, $Ce_{13}Fe_xCo_yB_{45}$ ($32 \leq x \leq 39$, $3 \leq y \leq 10$), as a new quaternary solid solution in the Ce-Fe-Co-B system at 900 °C, and the XRD pattern of this phase is extracted in Figure 4.18.

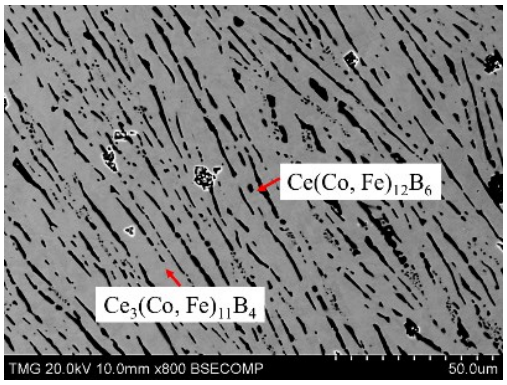

(a)

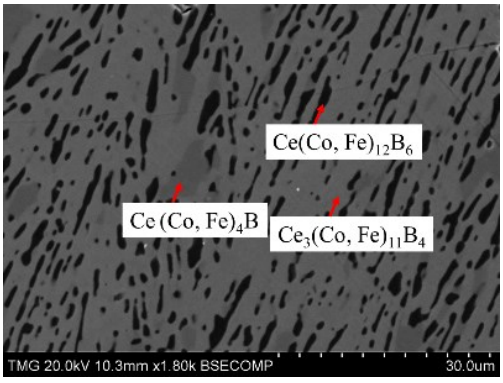

(b)

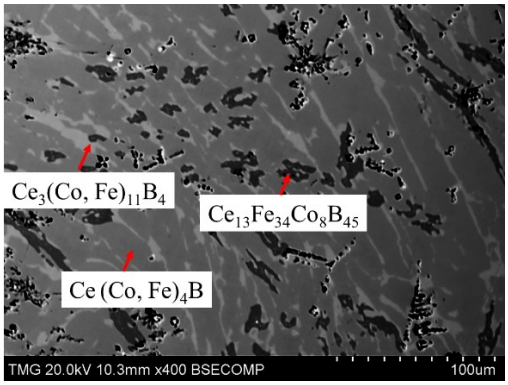

(c)

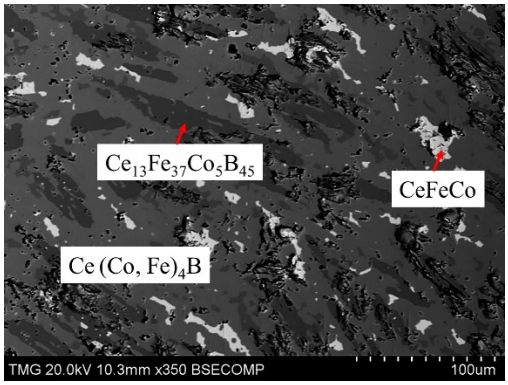

(d)

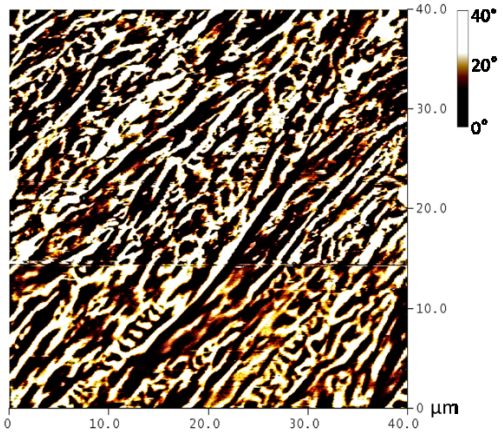

(e)

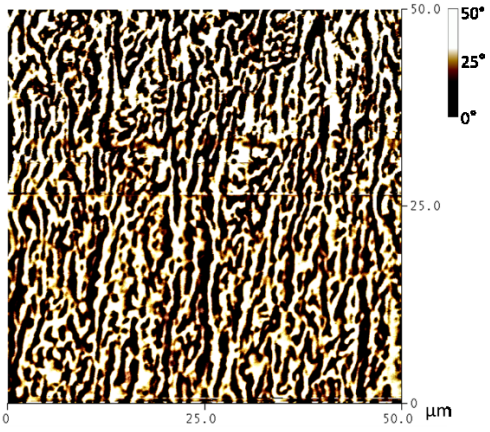

(f)

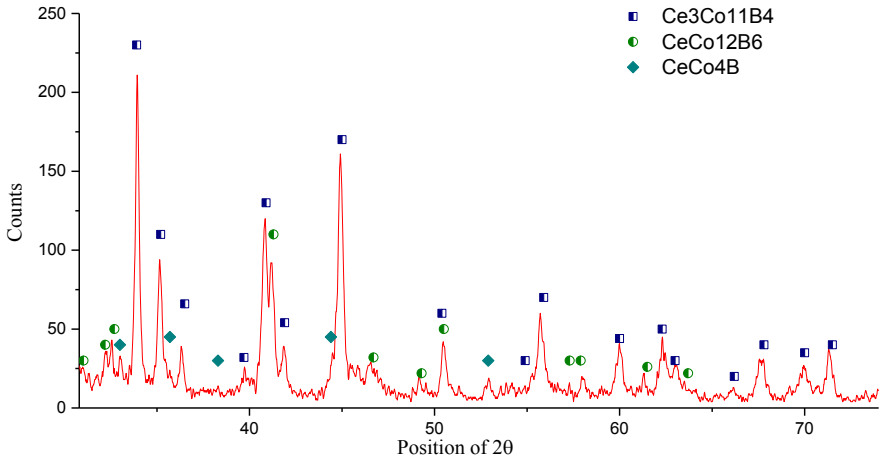

(g)

Figure 4.16. (a) BSE image of KA 11; (b) BSE image of KA 12; (c) BSE image of KA 13; (d) BSE image of KA 14; (e) MFM image of KA 11; (f) MFM image of KA 12; (g) XRD spectrum of KA 12.

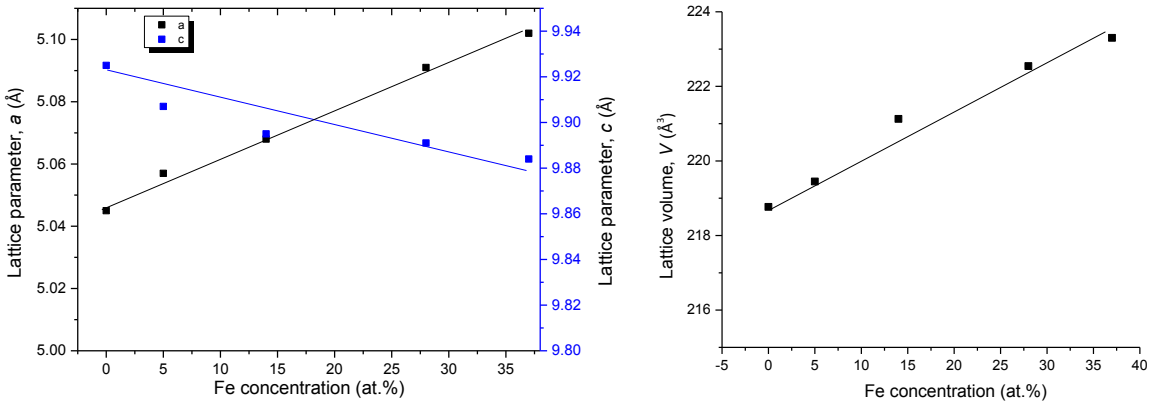

(a) (b)

Figure 4.17. Cell parameters *a* and *c* (a) and lattice volume *V* (b) with Co concentration for the $Ce_3(Co, Fe)_{11}B_4$ from KAs 10-13.

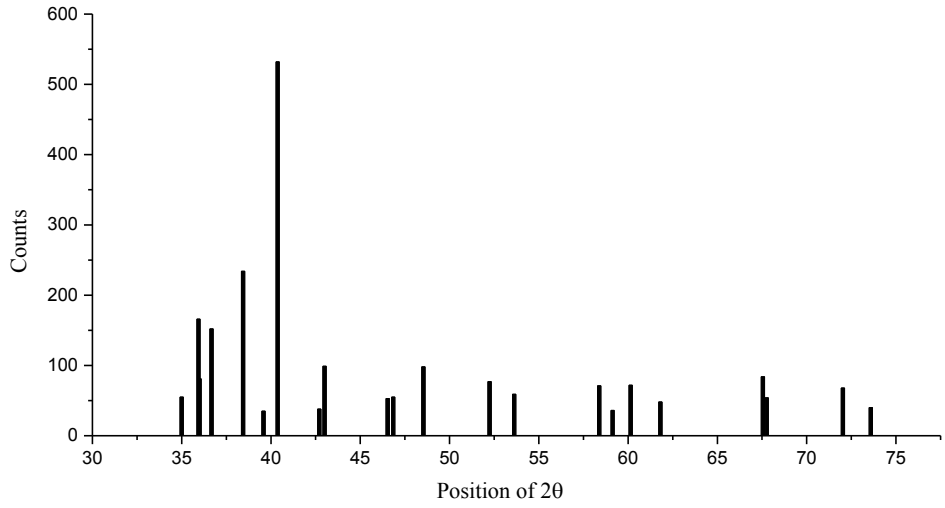

Figure 4.18. The extracted XRD pattern of $Ce_{13}Fe_xCo_yB_{45}$ ($32 \leq x \leq 39$, $3 \leq y \leq 10$).

The experimental results of KAs 9-17 are summarized in Figure 4.19 (a). Solid solubilities of magnetic $Ce_3(Co, Fe)_{11}B_4$ and non-magnetic $Ce(Co, Fe)_{12}B_6$ were first measured by diffusion couples as 23 at. % Fe and 18 at. % Fe, respectively. During the key alloys study, it has been proven that these two phases further extended into the quaternary system. And the solubility limits were measured as 46 at. % Fe and 37 at. % Fe, respectively. They can be presented as $CeCo_{12-x}Fe_xB_6$ ($0.76 \leq x \leq 8.74$) and $Ce_3Co_{11-x}Fe_xB_4$ ($0.9 \leq x \leq 5.04$), as illustrated in Figure 4.19 (a). Two pseudo ternary sections at 6 at. % and 16 at. % Ce were used to demonstrate the locations of $Ce(Co, Fe)_{12}B_6$ and $Ce_3(Co, Fe)_{11}B_4$, respectively, in Figure 4.19 (b, c). In Figure 4.19 (d), solid lines are the phase equilibria determined from key alloys, and dotted lines indicate the possible phase equilibria of detected phases.

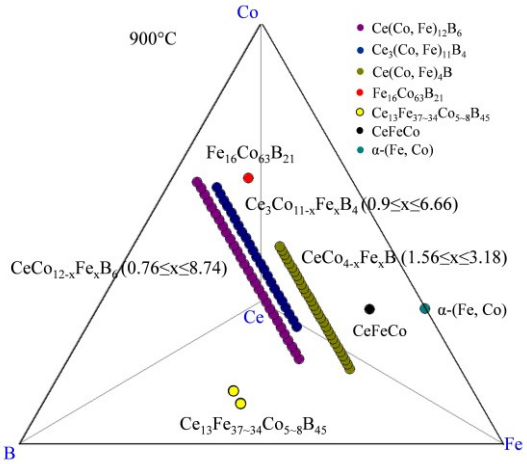

(a)

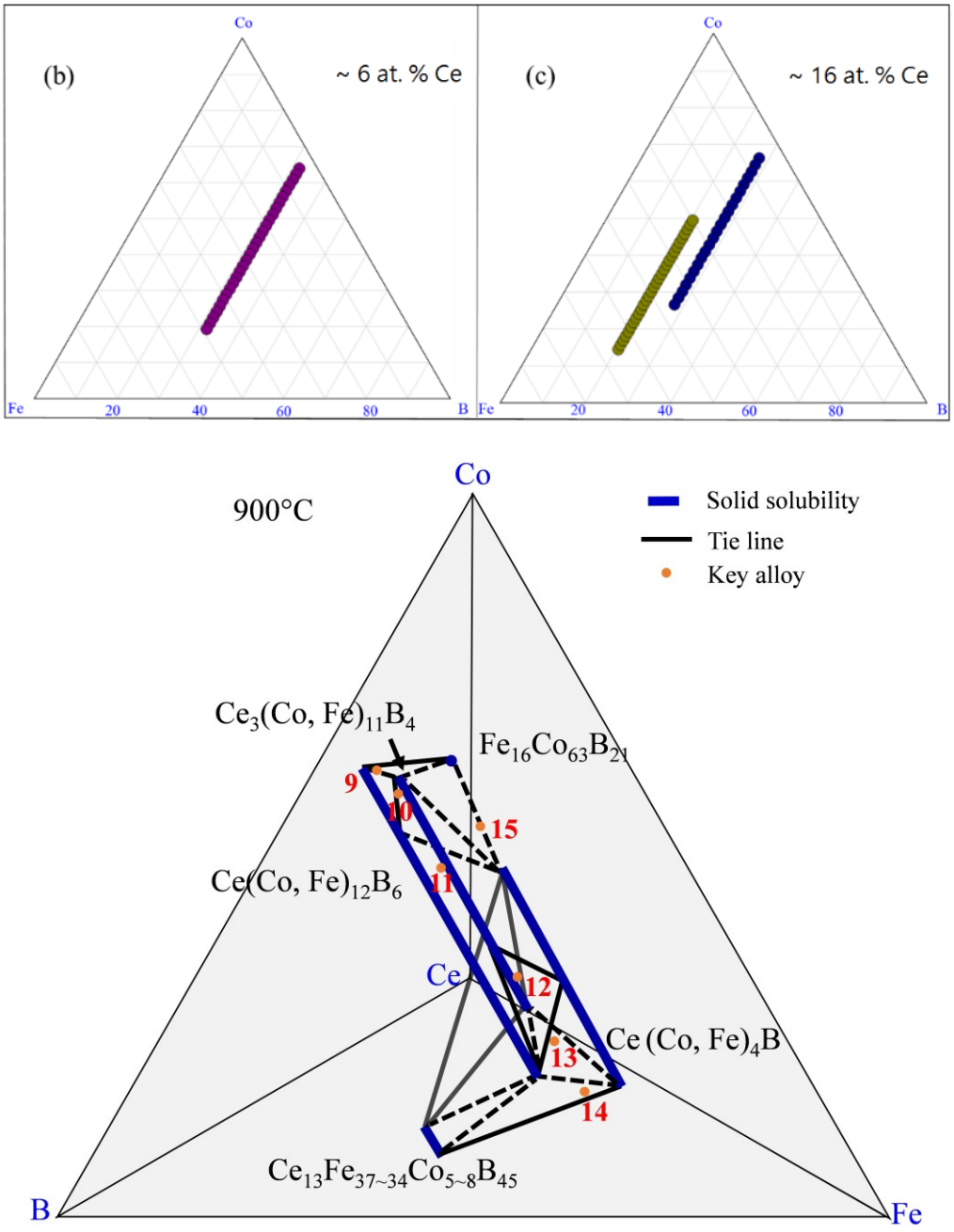

(d)

Figure 4.19. Homogeneity ranges of $Ce_3(Co, Fe)_{11}B_4$ and $Ce(Co, Fe)_{12}B_6$ obtained from key alloys: (a) 3D presentation of the experimental results; (b) pseudo ternary section at ~6 at. % Ce; (c) pseudo ternary section at ~16 at. % Ce; (d) phase relations obtained from the key alloys.

Combining the results which were obtained from the diffusion couples with those attained from the key alloys, the phases which were detected in the Ce-Fe-Co-B system in the Fe-Co rich region at 900 °C are plotted in Figure 4.20 (a). Seven three-phase equilibria were established as: α-(Fe, Co)/Ce_2(Fe, Co)$_{14}$B/Ce_2(Fe, Co)$_{17}$; Ce_2(Fe, Co)$_{14}$B/Ce(Co, Fe)$_4$B/CeFeCo; Ce_2(Fe, Co)$_{17}$/Ce(Co, Fe)$_4$B/α-(Fe, Co); Ce_3(Co, Fe)$_{11}B_4$/Ce(Co, Fe)$_{12}B_6$/Ce(Co, Fe)$_4$B; Ce_3(Co, Fe)$_{11}B_4$/Ce(Co, Fe)$_{12}B_6$/α-(Fe, Co); Ce_3(Co, Fe)$_{11}B_4$/Ce(Co, Fe)$_4$B/$Ce_{13}Fe_{34}Co_8B_{45}$, and Ce_3(Co, Fe)$_{11}B_4$/Ce(Co, Fe)$_4$B/α-(Fe, Co). The phase relations of the Ce-Fe-Co-B system in the Fe-rich corner at 900 °C are plotted in Figure 4.20 (f). Solid lines are the tie-lines determined in this study and dotted lines represent the possible phase relations. Among those detected phases, Ce_2(Fe, Co)$_{14}$B, Ce(Co, Fe)$_4$B, and Ce_3(Co, Fe)$_{11}B_4$ were magnetic in this system, which was proven by the MFM study. Also, Ce(Co, Fe)$_{12}B_6$ was identified as non-magnetic. The phases formed in the Fe-Co-Ce system are plotted in Figure 4.20 (a). Three pseudo ternary sections at around 6 at. %, 12 at. % and 16 at. % Ce were constructed to demonstrate the locations and phase relations of Ce(Co, Fe)$_{12}B_6$, Ce_2(Fe, Co)$_{14}$B, Ce(Co, Fe)$_4$B, and Ce_3(Co, Fe)$_{11}B_4$.

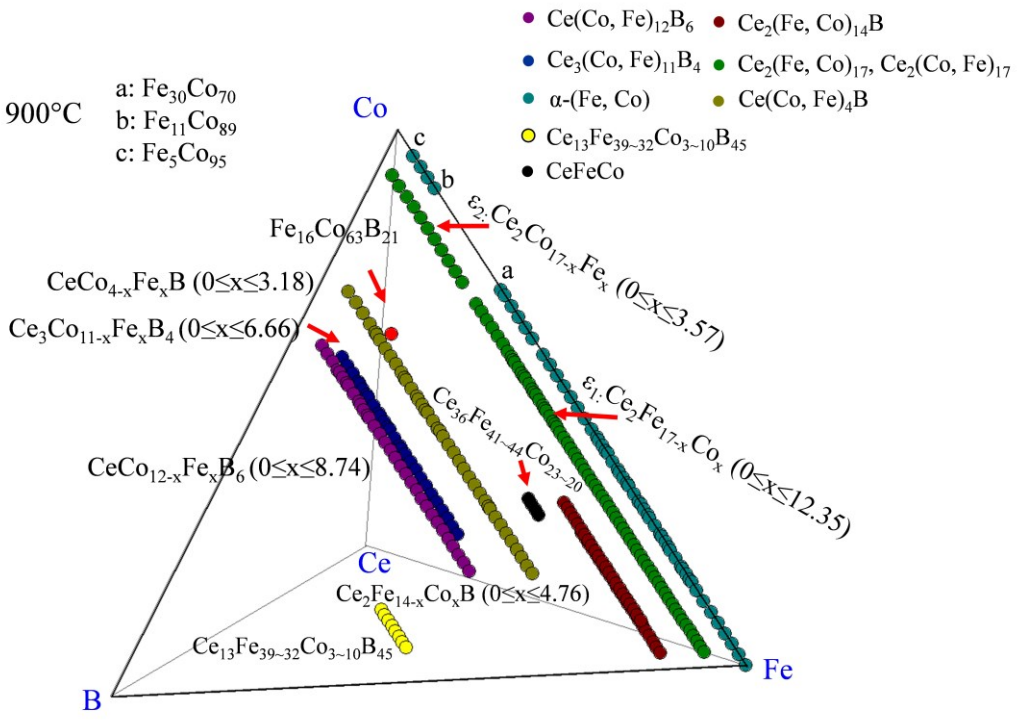

(a)

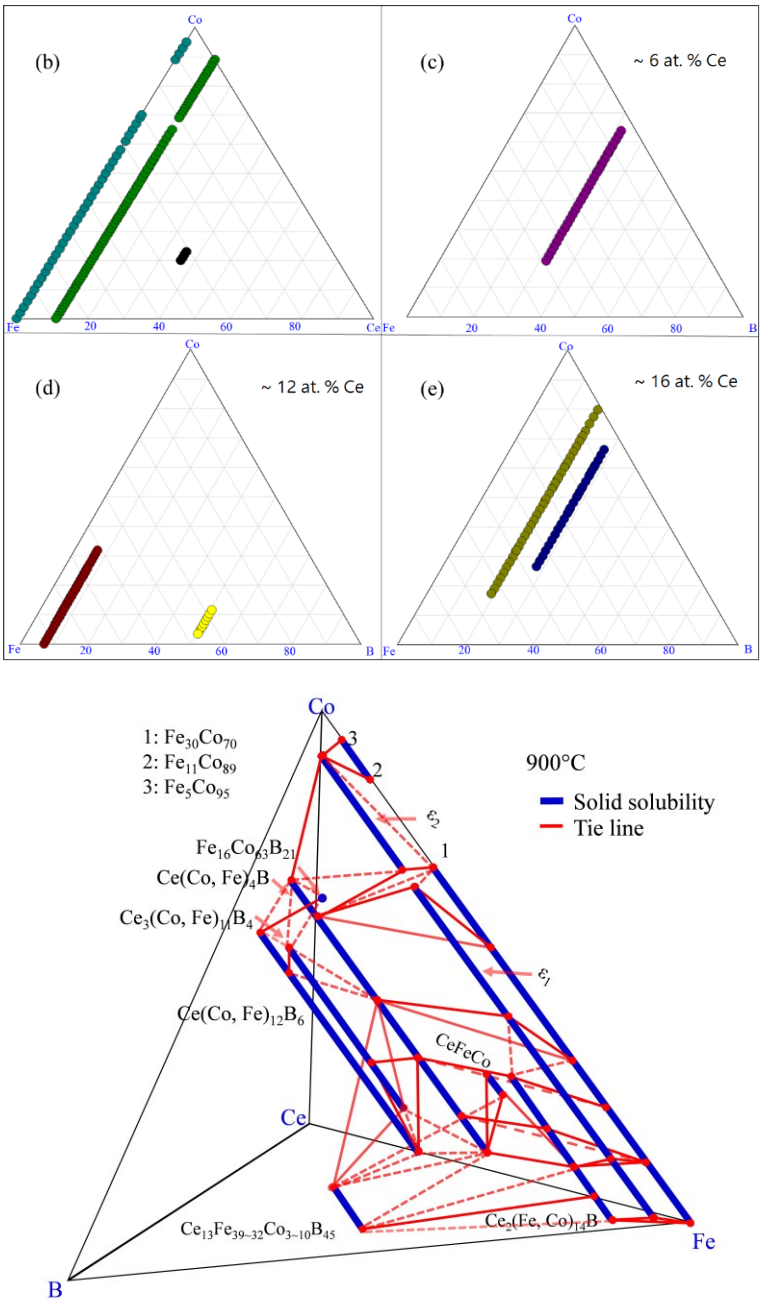

(f)

Figure 4.20. Combined experimental results of diffusion couples and key alloys in the Ce-Fe-Co-B system at 900°C: (a) 3D presentation of the experimental results; (b) Fe-Ce-Co ternary system; (c) pseudo ternary section at ~6 at. % Ce; (d) pseudo ternary section at ~12 at. % Ce; (e) pseudo ternary section at ~16 at. % Ce; (f) phase relations in the Fe-rich region of the Ce-Fe-Co-B system at 900°C.

Chapter 5: Intrinsic magnetic properties of $Ce_2(Fe, Co)_{14}B$ and its modifications by Ni and Cu

5.1 Intrinsic magnetic properties of $Ce_2Fe_{14-x}Co_xB$

The ferromagnetic tetragonal P42/mnm $Ce_2Fe_{14}B$ has attracted the attention of researchers hoping to build low cost magnets with acceptable magnetic properties suitable for automobile applications. The maximum solubility of $Ce_2Fe_{14-x}Co_xB$ was determined as 28 at.% Co (x=4.76) at 900°C. The details of the influence of Co substitution on the lattice parameters and lattice volume of $Ce_2Fe_{14-x}Co_xB$ can be found in Chapter 4. To measure the intrinsic magnetic properties of $Ce_2Fe_{14-x}Co_xB$, seven key alloys named KAs 18 to 24 were prepared along the homogeneity range by substituting different amounts of Fe with Co. The dominating $Ce_2(Fe, Co)_{14}B$ along with a small amount of impurities (such as α-(Fe, Co)) were obtained after the annealing process. Based on the WDS analysis, α-(Fe, Co) was found to dissolve up to 28 at.% Co. The M_s of α-(Fe, Co) at around 0, 10, 20, 30 at.% Co were reported to vary from 205 to 225 emu/g [54]. The M_s value of $Ce_2Fe_{14-x}Co_xB$ with different amounts of Co content is calculated using equation 1 mentioned in Chapter 3.

The influence of compositional variations on the intrinsic properties of $Ce_2Fe_{14-x}Co_xB$ has been studied and presented in Table 5.1. The magnetic measurements of $Ce_2Fe_{14-x}Co_xB$ were also compared with the dopant-free $Ce_2Fe_{14}B$ reference material. The compositional dependence of saturation magnetization, anisotropy field and Curie temperature of $Ce_2Fe_{14-x}Co_xB$ are plotted in Figures 5.1 and 5.2. The dotted lines in these figures are an approximate fit of the data.

Table 5.1. Dependence of intrinsic magnetic properties of $Ce_2Fe_{14-x}Co_xB$ on Co content.

Key alloy	Global composition (at.%)	Co content in $Ce_2Fe_{14-x}Co_xB$		M_s (emu/g) at 25°C	H_a (kOe) at 25°C	T_c (°C)
		at.%	x			
$Ce_2Fe_{14}B$	$Ce_{13.4}Fe_{80.0}B_{6.6}$	0	0	130.0	28.1	151 [4]
KA 18	$Ce_{13.2}Fe_{76.8}Co_{3.1}B_{6.9}$	3	0.51	133.9	29.2	227
KA 19	$Ce_{14.6}Fe_{72.8}Co_{6.7}B_{5.9}$	6	1.02	140.1	29.3	234
KA 20	$Ce_{15.3}Fe_{67.6}Co_{9.3}B_{7.8}$	9	1.53	145.1	25.5	271
KA 21	$Ce_{13.5}Fe_{69.6}Co_{12.3}B_{4.6}$	14	2.38	149.3	22.7	313
KA 22	$Ce_{14.7}Fe_{59.2}Co_{17.8}B_{8.3}$	18	3.06	153.8	21.7	351

KA 23	$Ce_{13.4}Fe_{61.1}Co_{20.3}B_{5.2}$	22	3.74	154.8	19.4	405
KA 24	$Ce_{13.7}Fe_{53}Co_{30.5}B_{4.9}$	28	4.76	155.1	13.2	467

The M_s and H_a of dopant-free $Ce_2Fe_{14}B$ are determined in this study, which are also consistent with the results of Orimoloye *et al.* [112]. The M_s of dopant-free $Ce_2Fe_{14}B$ at 25°C is measured as 130 emu/g which is approximately 982.8 kA/m using the density of $Ce_2Fe_{14}B$ reported in [4]. This value observed to be around 5% greater than the 931.1 kA/m reported by Herbst *et al.* [9] for $Ce_2Fe_{14}B$ at 22°C. Such a difference may be due to the contribution of secondary phases such as α-Fe, which is also observed by Orimoloye *et al.* [112]. The H_a of dopant-free $Ce_2Fe_{14}B$ is measured as 28.1 kOe which is 8% higher than the 26.0 kOe value reported in the literature [114-115]. As shown in Figure 5.1 (a), the saturation magnetization of $Ce_2Fe_{14-x}Co_xB$ is enhanced by Co substitution and becomes closer to that of $Nd_2Fe_{14}B$. By substituting 3 at.% Co (x=0.51) for Fe, the M_s was measured as 133.9 emu/g, which is higher than that of the dopant-free $Ce_2Fe_{14}B$ compound. And the M_s increased by approximately 1.32 emu/g for each 1 at.% substitution of Fe by Co up to 18 at.% Co ($x \leq 3.06$). However, the M_s value of $Ce_2Fe_{14-x}Co_xB$ did not increase considerably when the Co content was over 18 at.% and the rate was around 0.13 emu/g per 1 at.% Co. $Ce_2Fe_{14-x}Co_xB$ was observed to have the highest M_s value of 155.1 emu/g upon reaching the solubility limit of 28 at.% Co (x=4.76). With the influence of Co, the observed M_s value of $Ce_2Fe_{14-x}Co_xB$ exhibited a different tendency compared to that of $R_2(Fe, Co)_{14}B$ (R=Y, Nd and Gd) in [116]. The M_s dropped proportionally with the Co content in $R_2(Fe, Co)_{14}B$ (R=Y, Nd and Gd). On the other hand, the M_s of $Ce_2Fe_{14-x}Co_xB$ showed an increasing trend with Co. This different behavior might be due to the hybridization between the Ce 4*f* and Co 3*d* states which results in a strong induced polarization of Ce (4*f*+5*d*) states that brings large orbital moments at the Ce sites [117]. Also, the influence of Co on the saturation magnetization of $Ce_2Fe_{14-x}Co_xB$ could be related to the Co occupancy on different Fe sites which will be discussed in the next section.

The anisotropy field of $Ce_2Fe_{14-x}Co_xB$ with 3 at.% Co (x=0.51) was comparable to dopant-free $Ce_2Fe_{14}B$ and it showed a slightly increase to 29.3 kOe in the presence of 6 at.% Co (x=1.02). However, it is still inferior to that of $Nd_2Fe_{14}B$ as shown in Figure 5.1 (b). Beyond this composition, H_a of $Ce_2Fe_{14-x}Co_xB$ dropped monotonically with Co concentration. It decreased nearly at about 0.7 kOe for each 1 at.% substitution of Fe by Co. This behavior reflects the reduction of the uniaxial magnetocrystalline anisotropy which was reported by [10]. The decrease

in the magnetic anisotropy of $Ce_2Fe_{14-x}Co_xB$ with Co content is related to the lattice volume shrinkage [104]. Co substitution leads to a reduction in the size of $Ce_2Fe_{14-x}Co_xB$ particles which reduces the contributions of crystal-symmetry, and thereby influences the shape anisotropy and decreases the global anisotropy [104]. The influences of Co content on the anisotropy field and Curie temperature of $Ce_2Fe_{14-x}Co_xB$ are presented in Table 5.1. In general, Co substitution reduces the anisotropy field but increases the Curie temperature as well as the saturation magnetization of $Ce_2Fe_{14-x}Co_xB$.

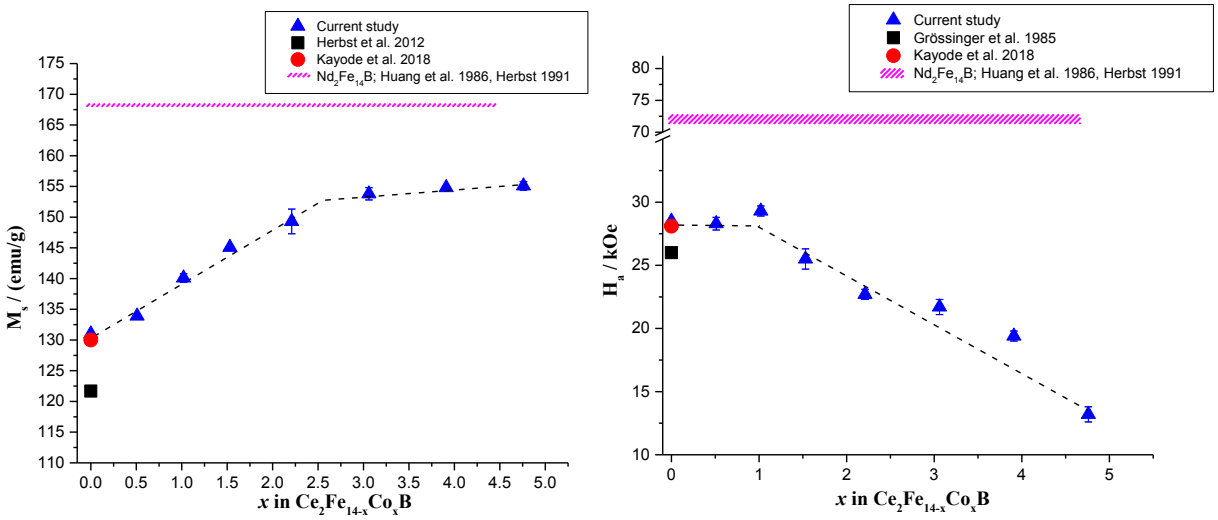

(a) (b)

Figure 5.1. Compositional dependence of (a) saturation magnetization; (b) anisotropy field of $Ce_2Fe_{14-x}Co_xB$ at 25°C. The thickness of $Nd_2Fe_{14}B$ line represents the variation in the literature data.

The Curie temperature of dopant-free $Ce_2Fe_{14}B$ was reported to be 151°C [4]. Based on current observation, the Curie temperature of $Ce_2Fe_{14-x}Co_xB$ increased proportionally with Co concentration, approximately 11.3°C for each 1 at.% Fe substituted by Co from pure $Ce_2Fe_{14}B$ to $Ce_2Fe_{9.24}Co_{4.76}B$ as shown in Figure 5.2. This is principally because the Co-Co exchange interaction is stronger than that of Co-Fe or Fe-Fe interactions [118]. As more Co ions are distributed into the lattice, the Fe-Fe interactions are gradually replaced by Co-Fe and then by Co-Co, which leads to an enhancement of the Curie temperature of $Ce_2Fe_{14-x}Co_xB$. The maximum T_c was measured as 467°C at 28 at.% Co (x=4.76), surpassing the value of the un-doped $Nd_2Fe_{14}B$ compound, as can be seen in Figure 5.2. A similar study has been done by Skoug *et al.* [10], where the Curie temperature of $Ce_3Fe_{14-x}Co_xB$ melt-spun ribbons was measured. They found that the

Curie temperature increased almost uniformly with the Co content in the range of 6 to 28 at.% ($1.02 \leq x \leq 4.76$). After a comparison of their results [10] with the current work in Figure 5.2, a similar trend was observed in both, as the T_c increases almost linearly with the Co content. However, in the current study, Curie temperature of $Ce_2Fe_{14-x}Co_xB$ is, on an average 50°C higher than that reported in [10]. The differences in Curie temperature of nanomaterials and bulk polycrystalline materials was also reported by Dominguez *et al.* [119]. They found as a result of the effect of particle size, the Curie temperature of $CoFe_2O_4$ nanoparticles was observed to be less than that of bulk materials [119]. A similar finding in this study with regard to the difference in Curie temperature suggested that such difference could be due to the particle size effect. The melt-spun ribbons were found to contain smaller grains compared to the annealed polycrystalline bulk materials [119]. In melt-spun materials, fluctuations of electron spins become more prominent, which could potentially reduce the magnetic exchange interaction. Thus, the order-disorder transition of magnetic moments in melt-spun ribbons could be achieved at a relatively lower temperature than the bulk materials, which leads to the lower Curie temperature [119].

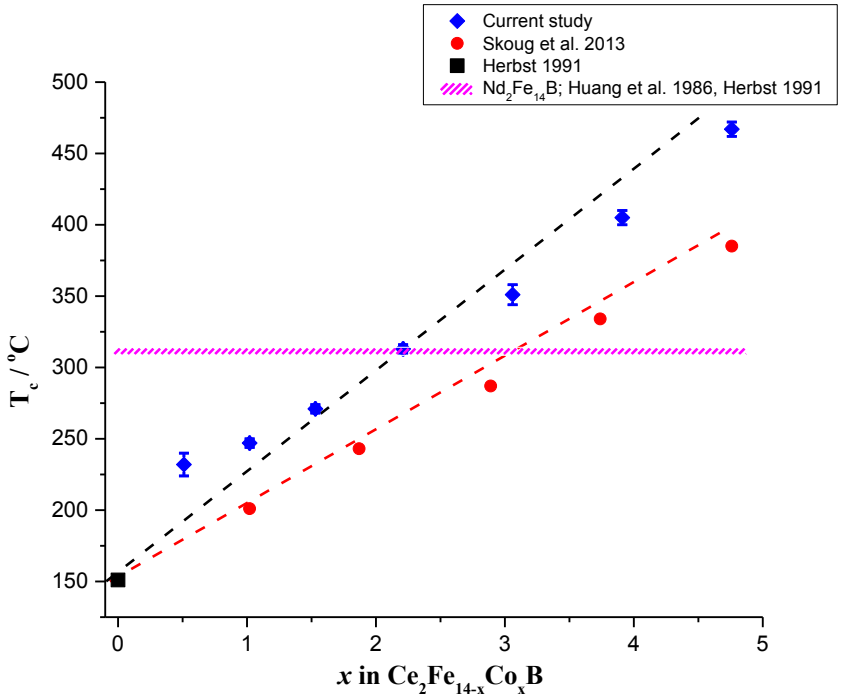

Figure 5.2. Current Curie temperature measurements in relation to Skoug *et al.* [10], Herbst [4] and Huang *et al.* [116].

The M_s of $Nd_2Fe_{14}B$ was reported as 16 kG (167.6 emu/g) at 22°C with H_a of 71~73 kOe and T_c of around 312°C [4, 116]. By substitution of Co for Fe in $Ce_2Fe_{14-x}Co_xB$, the M_s and T_c were largely enhanced. The M_s of $Ce_2Fe_{14-x}Co_xB$ is shown to be comparable to $Nd_2Fe_{14}B$, and even the T_c is observed to be greater, when containing Co content over 14 at.% ($x \geq 2.38$), as can be seen in Figures 5.1 (a) and 5.2. This indicates that Co-doped $Ce_2Fe_{14}B$ is a promising permanent magnet candidate which should be considered for further development. Hence, Co-containing $Ce_2Fe_{14}B$ solid solutions form the basis for the rest of the analysis presented in this thesis. In general, $Ce_2Fe_{14-x}Co_xB$ with 28 at.% Co (x=4.76) manifests the highest saturation magnetization and Curie temperature, but with the lowest anisotropy field. When selecting a potential permanent magnet for certain applications, an intermediate composition between 3 to 18 at.% Co ($0.51 \leq x \leq 3.06$) with high Curie temperature and saturation magnetization but with acceptable anisotropy field might be the most suitable.

5.2 Crystal structure refinement of $Ce_2Fe_{14-x}Co_xB$

The preference of Co occupancies on six crystallographically inequivalent Fe sites of $Nd_2(Fe, Co)_{14}B$ have been studied by Liao *et al.* [120]. Their results clearly indicate that Co prefers the 8*j2* and 16*k2* sites. Besides, Co atoms were seen to strongly avoid the 8*j1* site. The 16*k1* and 4*e* sites were observed to be randomly populated by the remaining Co atoms, while they also showed a small avoidance concerning the 4*c* site [120]. All the sites avoided by Co were found to be associated with the largest iron hyperfine fields, while the preferred sites tended to be those with small hyperfine fields [120]. It is known that the change of the average atomic size, caused by replacing Fe atoms with others, can be correlated with the change in the effective magnetic moment of hyperfine fields [121]. Therefore, it can be said that as the magnetic moment of the magnetic phase is associated with Fe atoms, whereas the change in the value of hyperfine fields caused by additives is related to the change in the magnetic moment [120]. This explains why modest Co additions to iron-based magnetic alloys generally lead to an increase in magnetization.

Table 5.2 presents the refined crystal structure parameters of $Ce_2Fe_{14-x}Co_xB$ and its reliability factors. The current refinement of structure parameters of $Ce_2Fe_{14-x}Co_xB$ shows consistent results with the study of $Nd_2Fe_{14-x}Co_xB$ in [120]. The decrease in the unit cell parameters is in favor of the Co occupancy at 8*j2* site. The prerequisite substitutional position of 8*j2* site has also been confirmed by the shortest lengths of Fe-Fe bond as can be seen in Table 5.3. Most of the bond

lengths with Fe4 show relatively short distance, indicating that the Fe4 position has higher potential to be substituted by the Co smaller atoms because shorter distance results in higher potential energy and more reactivity. Therefore, replacing Fe4 by Co atoms lowers the total energy enabling the materials to reach equilibrium. Once the 8*j2* site are completely occupied by Co atoms, Fe atoms start to be replaced sequentially by Co on 16*k2*, 4*e*, and 16*k1* sites.

Table 5.2. Refined crystal structure parameters of $Ce_2Fe_{14-x}Co_xB$.

Sample No.	Wyckoff position	Atomic position			Occupancy (%)	Reliability factors*		
		x	*y*	*z*		R_e	R_{wp}	*s*
KA 18	Fe1-16*k1*	0.0671	0.2765	0.1269	Fe 100.0	19.48	23.07	0.71
	Fe2-16*k2*	0.0379	0.3587	0.3237	Fe 100.0			
	Fe3-8*j1*	0.3174	0.3174	0.2535	Fe 100.0			
	FeCo4-8*j2*	0.0979	0.0979	0.2951	Co 27.1			
	Fe5-4*e*	0	0	0.1144	Fe 100.0			
	Fe6-4*c*	0	0.5	0	Fe 100.0			
	Ce1-4*g*	0.2313	0.7687	0	Ce 100.0			
	Ce2-4*f*	0.3585	0.3585	0	Ce 100.0			
	B-4*f*	0.1243	0.1243	0	B 100.0			
KA 19	Fe1-16*k1*	0.0671	0.2765	0.1269	Fe 100.0	21.06	23.66	0.79
	Fe2-16*k2*	0.0379	0.3587	0.3237	Fe 100.0			
	Fe3-8*j1*	0.3174	0.3174	0.2535	Fe 100.0			
	FeCo4-8*j2*	0.0979	0.0979	0.2951	Co 53.2			
	Fe5-4*e*	0	0	0.1144	Fe 100.0			
	Fe6-4*c*	0	0.5	0	Fe 100.0			
	Ce1-4*g*	0.2313	0.7687	0	Ce 100.0			
	Ce2-4*f*	0.3585	0.3585	0	Ce 100.0			
	B-4*f*	0.1243	0.1243	0	B 100.0			
KA 20	Fe1-16*k1*	0.0671	0.2765	0.1269	Fe 100.0	22.25	30.03	1.82
	Fe2-16*k2*	0.0379	0.3587	0.3237	Fe 100.0			
	Fe3-8*j1*	0.3174	0.3174	0.2535	Fe 100.0			
	FeCo4-8*j2*	0.0979	0.0979	0.2951	Co 82.9			
	Fe5-4*e*	0	0	0.1144	Fe 100.0			
	Fe6-4*c*	0	0.5	0	Fe 100.0			
	Ce1-4*g*	0.2313	0.7687	0	Ce 100.0			

	Ce2-4*f*	0.3585	0.3585	0	Ce 100.0			
	B-4*f*	0.1243	0.1243	0	B 100.0			
KA 21	Fe1-16*k1*	0.0671	0.2765	0.1269	Fe 100.0	21.86	29.31	1.79
	FeCo2-16*k2*	0.0379	0.3587	0.3237	Co 0.6			
	Fe3-8*j1*	0.3174	0.3174	0.2535	Fe 100.0			
	Co4-8*j2*	0.0979	0.0979	0.2951	Co 100.0			
	Fe5-4*e*	0	0	0.1144	Fe 100.0			
	Fe6-4*c*	0	0.5	0	Fe 100.0			
	Ce1-4*g*	0.2313	0.7687	0	Ce 100.0			
	Ce2-4*f*	0.3585	0.3585	0	Ce 100.0			
	B-4*f*	0.1243	0.1243	0	B 100.0			
KA 22	Fe1-16*k1*	0.0671	0.2765	0.1269	Fe 100.0	23.96	27.11	1.27
	FeCo2-16*k2*	0.0379	0.3587	0.3237	Co 20.6			
	Fe3-8*j1*	0.3174	0.3174	0.2535	Fe 100.0			
	Co4-8*j2*	0.0979	0.0979	0.2951	Co 100.0			
	Fe5-4*e*	0	0	0.1144	Fe 100.0			
	Fe6-4*c*	0	0.5	0	Fe 100.0			
	Ce1-4*g*	0.2313	0.7687	0	Ce 100.0			
	Ce2-4*f*	0.3585	0.3585	0	Ce 100.0			
	B-4*f*	0.1243	0.1243	0	B 100.0			
KA 23	Fe1-16*k1*	0.0671	0.2765	0.1269	Fe 100.0	22.98	26.49	1.32
	FeCo2-16*k2*	0.0379	0.3587	0.3237	Co 34.5			
	Fe3-8*j1*	0.3174	0.3174	0.2535	Fe 100.0			
	Co4-8*j2*	0.0979	0.0979	0.2951	Co 100.0			
	FeCo5-4*e*	0	0	0.1144	Co 6.5			
	Fe6-4*c*	0	0.5	0	Fe 100.0			
	Ce1-4*g*	0.2313	0.7687	0	Ce 100.0			
	Ce2-4*f*	0.3585	0.3585	0	Ce 100.0			
	B-4*f*	0.1243	0.1243	0	B 100.0			
KA 24	FeCo1-16*k1*	0.0671	0.2765	0.1269	Co 3.5	22.64	30.86	1.85
	FeCo2-16*k2*	0.0379	0.3587	0.3237	Co 43.4			
	Fe3-8*j1*	0.3174	0.3174	0.2535	Fe 100.0			
	Co4-8*j2*	0.0979	0.0979	0.2951	Co 100.0			
	FeCo5-4*e*	0	0	0.1144	Co 19.5			
	Fe6-4*c*	0	0.5	0	Fe 100.0			
	Ce1-4*g*	0.2313	0.7687	0	Ce 100.0			

Ce2-4*f*	0.3585	0.3585	0	Ce 100.0
B-4*f*	0.1243	0.1243	0	B 100.0

* Reliability factors: R_e is the value statistically expected; R_{wp} is the weighted summation of residuals of the least squared fit; *s* presents the goodness of fit.

Table 5.3. Atomic Fe-Fe bond lengths of $Ce_2Fe_{14-x}Co_xB$. The bold values represent the shortest atomic Fe-Fe bond.

Atom 1	Atom2	Distance (Å)
Fe1	Fe5	2.497
Fe1	Fe6	2.554
Fe1	Fe4	2.576
Fe1	Fe1	2.594
Fe1	Fe3	2.696
Fe2	Fe4	**2.369**
Fe2	Fe1	2.454
Fe2	Fe6	2.483
Fe2	Fe2	2.539
Fe2	Fe3	2.616
Fe4	Fe4	**2.426**
Fe4	Fe5	2.494
Fe4	Fe3	2.633
Fe3	Fe5	2.767
Fe5	Fe5	2.760

The fractional atomic occupancy of 8*j2*, 16*k2*, 4*e* and 16*k1* sites of $Ce_2Fe_{14-x}Co_xB$ have been determined as a function of Co concentration which has been presented in Figure 5.3. When adding Co and Ni, the reduction in effective magnetic hyperfine fields is proportional to the electrons in partially filled 3*d* and 4*d* shell [122]. On the other hand, when adding Cu, the reduction in the effective magnetic hyperfine fields is directly proportional to the number of electrons in the outer electron shell and inversely proportional to the number of electrons of the additive element [122]. As Co occupies the Fe sites with low hyperfine fields, an increase of saturation magnetization of magnetic phase is achieved. Relating Figure 5.3 to the saturation magnetization of $Ce_2Fe_{14-x}Co_xB$

in Figure 5.1 (a), an increase is observed in saturation magnetization when $x \leq 2.38$ is related to the continuous occupancy of Co atoms at 8*j2* site. Later, the Co occupancy at other Fe sites does not influence the saturation magnetization significantly. However, the Co substitution in the unit cell leads to a stronger average exchange interaction which may be responsible for the significantly higher Curie temperature [123] and for the continuous increase of its value with Co concentration. The coordination spheres and atomic substitution of Fe by Co for the different atomic coordinates have been identified and presented in Figure 5.4. The sequence of Co substitution on Fe sites gradually occupying 8*j2* site of $Ce_2Fe_{14-x}Co_xB$ is followed by the sequentially occupation of 16*k2*, 4*e* and 16*k1* sites, both of which have been illustrated in this figure.

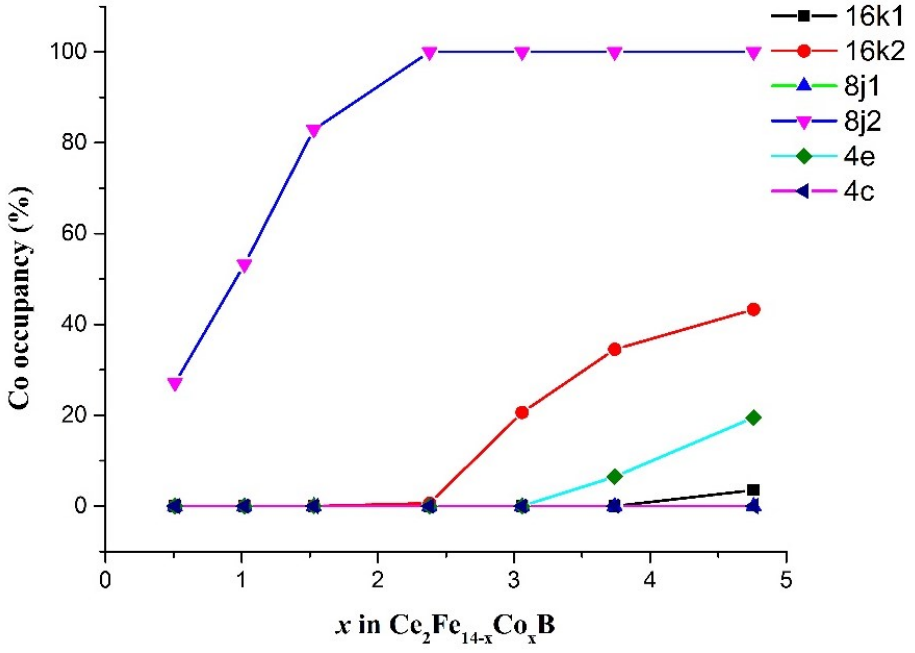

Figure 5.3. Co occupancy in $Ce_2Fe_{14-x}Co_xB$ as a function of Co concentration.

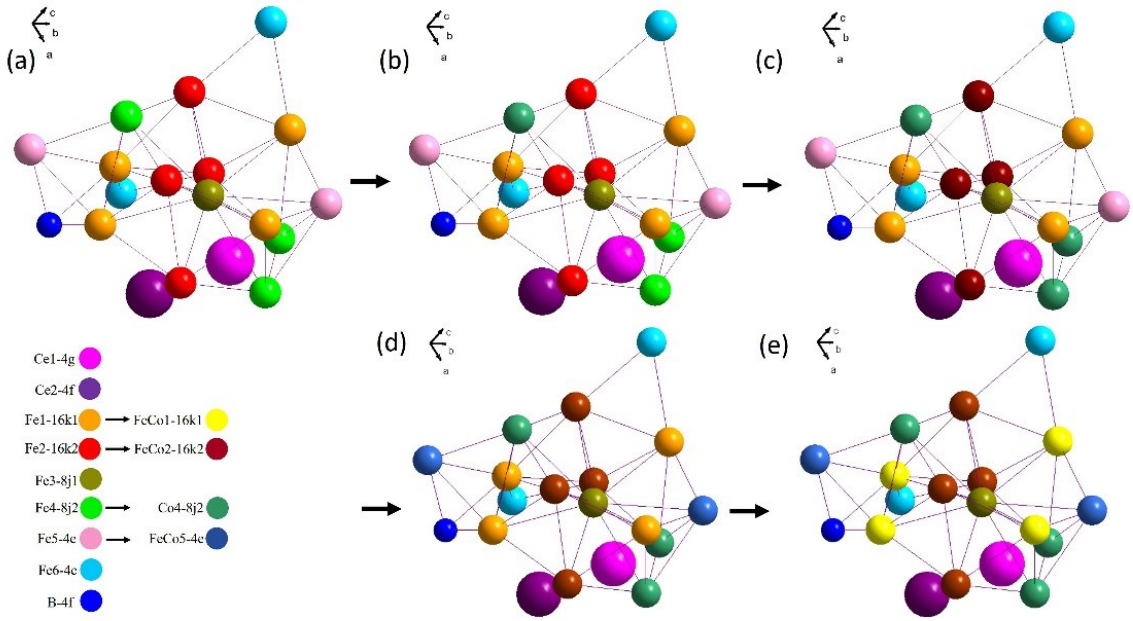

Figure 5.4. The coordination spheres of dynamic atomic substitution of Fe by Co with different atomic coordinates: (a) before Co substitution in $Ce_2Fe_{14}B$; (b) to (c) substitution of Fe atoms by Co atoms on 8*j2* site until they are completely occupied by Co and then started to occupy 16*k2* site; (d) to (e) the substitution of Fe by Co atoms on 4*e* and 16*k1* sites.

5.3 Intrinsic magnetic properties of $Ce_2Fe_{12.98-x}Co_{1.02}Ni_xB$ and $Ce_2Fe_{12.98-x}Co_{1.02}Cu_xB$

$Ce_2Fe_{14-x}Co_xB$ with 6 at.% Co (x=1.02) was found to have the highest anisotropy field (H_a=29.3 kOe) with a saturation magnetization of 140.1 emu/g and Curie temperature of 234°C in the range between 0 and 28 at.% Co ($0 \leq x \leq 4.76$). According to the research of Fan *et al.* [124], the substitution of Ni for Co was detrimental to the Curie temperature of the FeCoZrBCu magnet. In order to maintain the thermal stability as well as the high anisotropy field of $Ce_2(Fe, Co)_{14}B$, six Ni-doped $Ce_2(Fe, Co)_{14}B$ alloys were designed by keeping the Co concentration constant at 6 at.%, while substitutions occurred between Fe and Ni. The chemical compositions were presented by the formula of $Ce_2Fe_{12.98-x}Co_{1.02}Ni_xB$. Fe was substituted by around 0.5, 1, 3, 5, 7, 10 and 13 at.% Ni to study the effect of Ni on the intrinsic magnetic properties and measure the homogeneity range of $Ce_2Fe_{12.98-x}Co_{1.02}Ni_xB$ at 900°C. The dominant $Ce_2Fe_{12.98-x}Co_{1.02}Ni_xB$ was obtained in KAs 25 to 29. As the Ni content increased to 10 at.% in the global composition, the quantity of $Ce_2(Fe, Co, Ni)_{14}B$ reduced significantly due to the formation of other phases. The solid solubility of Ni in $Ce_2Fe_{12.98-x}Co_{1.02}Ni_xB$ was measured to be around 8 at.% (x=1.36) at 900°C. Traces of

$Ce_2(Fe, Co, Ni)_{14}B$ were no longer observed in the alloy containing 12 at.% Ni, and $Ce(Co, Fe, Ni)_4B$ became the dominating phase.

The influence of Ni on the lattice parameters of $Ce_2Fe_{12.98-x}Co_{1.02}Ni_xB$ is illustrated in Figure 5.5. The substitution of Fe by Ni, which has a smaller atomic radius, leads to a decrease in the unit cell parameters and the lattice volume. This is confirmed by the increase in 2θ values of the peak positions due to an increase in Ni concentration. The linear relations between the lattice parameters, lattice volume, and Ni concentration obey Vegard's law [110], thereby indicating the occurrence of substitutional solid solubility in $Ce_2Fe_{12.98-x}Co_{1.02}Ni_xB$.

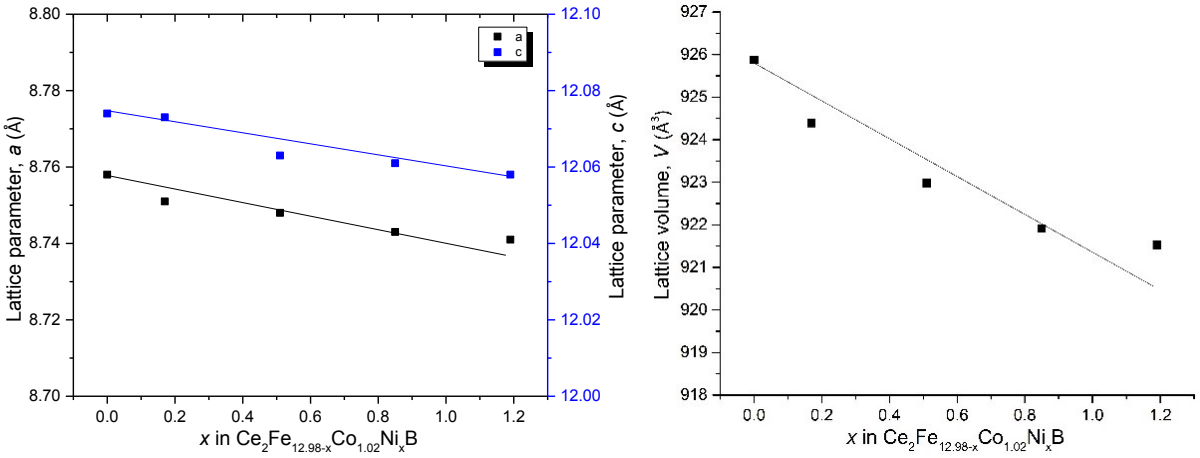

(a) (b)

Figure 5.5. Cell parameters (a) a and c; and (b) lattice volume V versus Ni concentration in $Ce_2Fe_{12.98-x}Co_{1.02}Ni_xB$.

The intrinsic magnetic properties of $Ce_2Fe_{12.98-x}Co_{1.02}Ni_xB$ are summarized in Table 5.4. Curie temperature of Ni-doped $Ce_2Fe_{12.98}Co_{1.02}B$ is improved; whereas, the saturation magnetization and the anisotropy field have diminished with the Ni substitution. The compositional dependence of saturation magnetization, anisotropy field, and Curie temperature of $Ce_2Fe_{12.98-x}Co_{1.02}Ni_xB$ are plotted as red triangles in Figure 5.6, where the red dotted lines are an approximate fit of the data.

Table 5.4. Intrinsic magnetic properties of $Ce_2Fe_{12.98-x}Co_{1.02}Ni_xB$.

Key alloy	Global composition (at.%)	Ni content in $Ce_2Fe_{12.98-x}Co_{1.02}Ni_xB$		M_s (emu/g) at 25°C	H_a (kOe) at 25°C	T_c (°C)
		at.%	x			
$Ce_2Fe_{12.98-x}Co_{1.02}Ni_xB$	$Ce_{14.6}Fe_{72.8}Co_{6.7}B_{5.9}$	0	0	140.1	29.3	234
KA 25	$Ce_{14.5}Fe_{73.1}Co_{6.1}Ni_{0.5}B_{5.8}$	0.7	0.12	135.2	26.6	261
KA 26	$Ce_{14.8}Fe_{73.9}Co_{5.9}Ni_{1.2}B_{4.2}$	1	0.17	128.0	25.7	265
KA 27	$Ce_{15.1}Fe_{67.1}Co_{6.8}Ni_{3.1}B_{7.9}$	3	0.51	124.8	24.5	278
KA 28	$Ce_{13.5}Fe_{67.4}Co_{6.4}Ni_{5.4}B_{7.3}$	5	0.85	115.7	23.8	293
KA 29	$Ce_{12.7}Fe_{66.9}Co_{6.5}Ni_{7.3}B_{6.6}$	7	1.19	113.3	22.6	297

A drop of the M_s value is observed at a rate of 3.82 emu/g per 1 at.% Ni as shown in Figure 5.6 (a), which indicates that Ni additive is detrimental to the saturation magnetization of $Ce_2Fe_{12.98}Co_{1.02}B$. A similar phenomenon was also observed by Bolzoni *et al.* [86]. They analyzed three Ni-doped $Nd_2Fe_{14}B$ alloys, where the M_s value was reported to drop from 187 to 180 emu/g at 77K after dissolving around 6 at.% Ni. Ni reducing the saturation magnetization of $Nd_2(Fe_{1-y}Ni_y)_{14}B$ was explained by the electron transfer between Ni and Nd [61]. Ni prefers to substitute Fe at the 16*k2* and 8*j2* sites simultaneously in $Nd_2(Fe_{1-y}Ni_y)_{14}B$ [125]. The large electronegativity difference between Ni and rare earth atoms [126], and the 16*k2* site occupancy by Ni atoms both result in considerable electron transfer, which thereby leads to the hybridized state commonly observed in RE-Ni compounds [127]. In $Nd_2(Fe_{1-x-y}Co_xNi_y)_{14}B$. The 8*j2* site is separated from the Nd-B layers by the iron atomic layer as can be seen in Figure 5.4. Hence, the electron transfer does not take place after the Ni occupancy and the saturation magnetization of $Nd_2(Fe_{1-x-y}Co_xNi_y)_{14}B$ is only affected by the Co content and the occupancy of Co atoms at this site [91]. In our case, the double substitution of Co and Ni for Fe atoms could further impact the electron transfer in the crystal. In $Ce_2Fe_{12.98-x}Co_{1.02}Ni_xB$, 8*j2* site has been largely occupied by Co atoms, which leads to the gradual occupancy of Ni atoms at 16*k2* site during the substitution. Since the occupancy of Ni at 8*j2* site does not affect the saturation magnetization, as significantly more Ni atoms occupy 16*k2* site, certain amount of electron transfer occurs, and the saturation magnetization of $Ce_2Fe_{12.98-x}Co_{1.02}Ni_xB$ decreases monotonously with Ni as shown in Figure 5.6 (a).

Ni has a low anisotropy constant *K1* of -5.7×10^3 J/m^3, which is far lower than that of Fe (48×10^3 J/m^3) and Co (461×10^3 J/m^3) at room temperature [128]. Thus, Ni substitution for Fe could reduce the effective magneto-crystalline anisotropy of Ni-doped $Ce_2Fe_{12.98}Co_{1.02}B$. The

compositional dependence of the anisotropy field at 25°C is shown in Figure 5.6 (b). The H_a value of $Ce_2Fe_{12.98}Co_{1.02}B$ before Ni substitution was measured to be at 29.3 kOe. With the influence of Ni, a drop was observed in the anisotropy field of Ni-doped $Ce_2Fe_{12.98}Co_{1.02}B$. The decrement rate of H_a is determined as 0.96 kOe per 1 at.% Ni. Similarly, Bolzoni *et al.* [86] found that H_a of $Nd_2Fe_{14-x}Ni_xB$ ($1 \leq x \leq 3$) decreased with the influence of Ni at 293 K.

Ni substitution enhances the Curie temperature of $Nd_2Fe_{14-x}Ni_xB$ [86]. For the current $Ce_2Fe_{12.98-x}Co_{1.02}Ni_xB$, substitution of Ni for Fe increases the Curie temperature significantly, which indicates that the magnetic interactions are highly improved by Ni. The T_c of $Ce_2Fe_{12.98-x}Co_{1.02}Ni_xB$ is improved from 234°C to around 297°C after doping with 7 at.% Ni (x=1.19) as can be seen in Figure 5.6 (c). The increment rate of T_c is approximately 9°C per 1 at.% Ni. An overall enhancement of Curie temperature could be observed for $Ce_2Fe_{12.98-x}Co_{1.02}Ni_xB$ in Figure 5.6 (c). In general, $Ce_2Fe_{12.98-x}Co_{1.02}Ni_xB$ (x=0.12) has the optimum intrinsic magnetic properties, because it has the highest M_s value (135.2 emu/g) among the Ni-containing alloys with moderate H_a (26.6 kOe) and T_c (261°C) among all Ni-doped $Ce_2Fe_{12.98}Co_{1.02}B$.

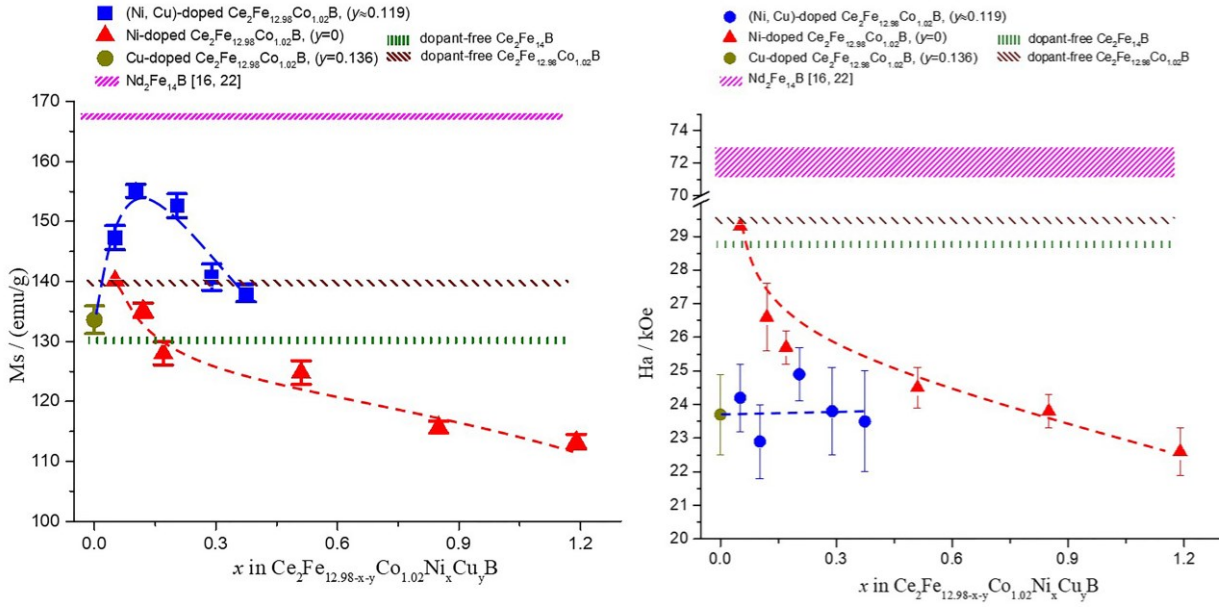

(a) (b)

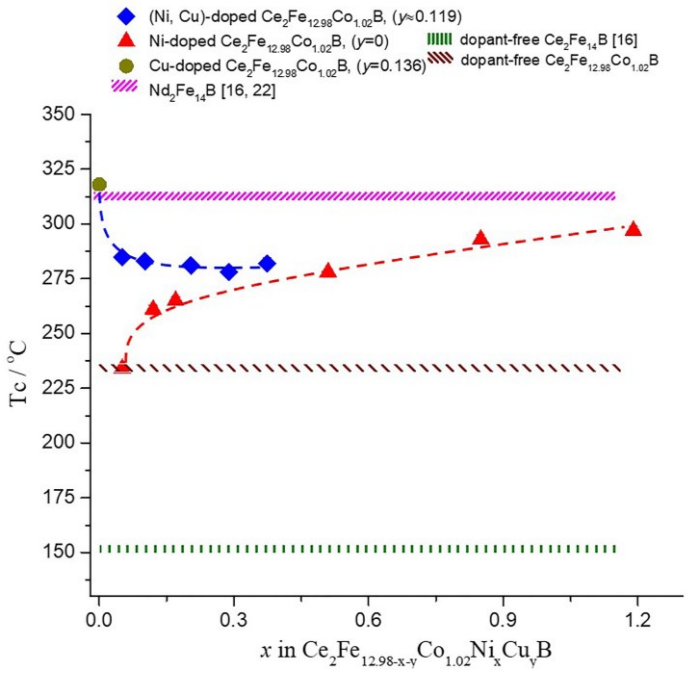

(c)

Figure 5.6. Compositional dependence of (a) saturation magnetization; (b) anisotropy field; (c) Curie temperature of $Ce_2Fe_{12.98-x-y}Co_{1.02}Ni_xCu_yB$. The thickness of $Nd_2Fe_{14}B$ line represents the variation in the literature data.

Cu normally locates at the intergranular regions. Through pinning the domain wall movement, Cu is an essential additive that influences the extrinsic magnetic properties of Nd-Fe-B [129]. Therefore, Cu effects on the intrinsic magnetic properties of $Ce_2(Fe, Co)_{14}B$ have to be understood first, especially because this information is scarce in the literature. As discussed in Chapter 2, the Fe-Cu and Co-Cu binary systems are characterized by the presence of a liquid-liquid miscibility gap [94, 95], which leads to the fact that very limited Cu could dissolve in the Fe-rich or Co-rich Ce-Fe-Co-B compounds. Key alloys were designed by varying Cu content in the global compositions of $Ce_2Fe_{12.98-x}Co_{1.02}Cu_xB$ alloys. The maximum solid solubility of $Ce_2Fe_{12.98-x}Co_{1.02}Cu_xB$ was determined as 0.8 at.% Cu (x=0.136) at 900°C. The intrinsic magnetic properties of $Ce_2Fe_{12.98-x}Co_{1.02}Cu_xB$ (x=0.136) are discussed below.

When $Ce_2Fe_{12.98-x}Co_{1.02}Cu_xB$ contained 0.8 at.% Cu (x=0.136), the Curie temperature increased up to 318°C. Meanwhile, the saturation magnetization and the anisotropy field decreased from 140.1 emu/g to 133.6 emu/g, and from 29.3 kOe to 23.7 kOe, respectively. As compared to $Ce_2Fe_{12.81}Co_{1.02}Ni_{0.17}B$ which contains similar Ni content as that of Cu, it is obvious that Cu is

much more effective in improving Curie temperature than Ni. By doping with Cu, the T_c of $Ce_2Fe_{12.844}Co_{1.02}Cu_{0.136}B$ is observed to be higher than that of Ni-doped $Ce_2Fe_{12.81}Co_{1.02}Ni_{0.17}B$, while the M_s and H_a values of these two compounds were close to each other as can be seen in Table 5.5 and Figure 5.6.

Table 5.5. Intrinsic magnetic properties of $Ce_2Fe_{12.98-x}Co_{1.02}Cu_xB$.

Key alloy	Global composition (at.%)	Cu content in $Ce_2Fe_{12.98-x}Co_{1.02}Cu_xB$		M_s (emu/g) at 25°C	H_a (kOe) at 25°C	T_c (°C)
		at.%	x			
$Ce_2Fe_{12.98-x}Co_{1.02}Cu_xB$	$Ce_{14.6}Fe_{72.8}Co_{6.7}B_{5.9}$	0	0	140.1	29.3	234
$Ce_2Fe_{12.81}Co_{1.02}Ni_{0.17}B$	$Ce_{14.8}Fe_{73.9}Co_{5.9}Ni_{1.2}B_{4.2}$	0	0	128.0	25.7	271
KA 30	$Ce_{13.2}Fe_{71.6}Co_{6.3}Cu_{1.1}B_{7.8}$	0.8	0.136	133.6	23.7	318

5.4 The combined effects of Ni and Cu on intrinsic magnetic properties of $Ce_2Fe_{12.98-x-y}Co_{1.02}Ni_xCu_yB$

The effects of substituting Fe by both Ni and Cu on the intrinsic magnetic properties of $Ce_2Fe_{12.98}Co_{1.02}B$ were also studied. Six $Ce_2Fe_{12.98-x-y}Co_{1.02}Ni_xCu_yB$ alloys were prepared by keeping the Co content constant at 6 at.%. The contents of Ni and Cu contents, however, varied in the global compositions as listed in Table 5.6. Dominating $Ce_2Fe_{12.98-x-y}Co_{1.02}Ni_xCu_yB$ is obtained in all alloys after the process of annealing at 900°C for 25 days. The Cu overall content was varied in six alloys from 0.7 to 2.8 at.%. Cu solubility in this compound was measured using WDS point analysis on several locations and the average value was reported. In all of the six samples, the maximum Cu solubility was 0.8 at.% in $Ce_2Fe_{12.98-x-y}Co_{1.02}Ni_xCu_yB$. This is also consistent with the results of the Cu-doped $Ce_2Fe_{12.98}Co_{1.02}B$ which are discussed in the previous section.

The intrinsic magnetic properties of $Ce_2Fe_{12.98-x-y}Co_{1.02}Ni_xCu_yB$ are summarized in Table 5.6. It is noticeable that the saturation magnetization and the Curie temperature are improved, while the anisotropy field drops after the double substitution. The optimum intrinsic magnetic properties of $Ce_2Fe_{12.98-x-y}Co_{1.02}Ni_xCu_yB$ were observed to be as follows: M_s=152.6 emu/g, H_a=24.9 kOe and T_c=281°C, at Ni=1.2 at.% (x=0.204) and Cu=0.7 at.% (y=0.119). The intrinsic magnetic properties of (Ni, Cu)-doped $Ce_2Fe_{12.98}Co_{1.02}B$ were also compared with the Ni-doped and the Cu-doped $Ce_2Fe_{12.98}Co_{1.02}B$ compound as well as with $Nd_2Fe_{14}B$, which have been depicted in Figure 5.6. The Cu content in $Ce_2Fe_{12.98-x-y}Co_{1.02}Ni_xCu_yB$ varied in a limited range between 0.6 to 0.8 at.%. For the purpose of comparison, the Cu contents dissolved in all the

$Ce_2Fe_{12.98-x-y}Co_{1.02}Ni_xCu_yB$ solid solutions are considered to be 0.7 at.% (y≈0.119) in Figure 5.6. The intrinsic magnetic properties of $Nd_2Fe_{14}B$, dopant-free $Ce_2Fe_{14}B$ and dopant-free $Ce_2Fe_{12.98}Co_{1.02}B$ are also inserted using pink, green and brown lines in Figure 5.6. They represent benchmarks to measure the improvement in the magnetic property improvement after doping with Ni and/or Cu.

Table 5.6. Intrinsic magnetic properties of $Ce_2Fe_{12.98-x-y}Co_{1.02}Ni_xCu_yB$.

Key alloy	Global composition (at.%)	Ni content in $Ce_2Fe_{12.98-x-y}Co_{1.02}Ni_xCu_yB$		Cu content in $Ce_2Fe_{12.98-x-y}Co_{1.02}Ni_xCu_yB$		M_s (emu/g) at 25°C	H_a (kOe) at 25°C	T_c (°C)
		at.%	x	at.%	y			
$Ce_2Fe_{12.98}Co_{1.02}B$	$Ce_{14.6}Fe_{72.8}Co_{6.7}B_{5.9}$	0	0	0	0	140.1	29.3	234
KA 31	$Ce_{13.1}Fe_{71.6}Co_{6.1}Ni_{0.3}Cu_{2.8}B_{6.1}$	0.3	0.051	0.8	0.136	147.3	24.2	285
KA 32	$Ce_{10.3}Fe_{74.9}Co_{6.0}Ni_{0.5}Cu_{2.6}B_{5.7}$	0.6	0.102	0.8	0.136	155.1	22.9	283
KA 33	$Ce_{15.1}Fe_{71.8}Co_{5.8}Ni_{0.9}Cu_{2.1}B_{4.3}$	1.2	0.204	0.7	0.119	152.6	24.9	281
KA 34	$Ce_{11.2}Fe_{73.8}Co_{7.8}Ni_{1.3}Cu_{1.7}B_{4.2}$	1.7	0.289	0.7	0.119	140.7	23.8	278
KA 35	$Ce_{14.8}Fe_{68.0}Co_{6.3}Ni_{1.9}Cu_{1.2}B_{7.8}$	2.2	0.374	0.7	0.119	138.1	23.5	282
KA 36	$Ce_{13.7}Fe_{68.8}Co_{6.1}Ni_{2.2}Cu_{0.7}B_{8.5}$	2.4	0.408	0.6	0.102	142.2	24.6	281

Figure 5.6 (a) shows the saturation magnetization of $Ce_2Fe_{12.98-x-y}Co_{1.02}Ni_xCu_yB$ in the range of 0≤x≤0.41, y≈0.119. In general, the M_s of (Ni, Cu)-doped $Ce_2Fe_{12.98}Co_{1.02}B$ is seen to be higher than that of Ni-doped or Cu-doped $Ce_2Fe_{12.98}Co_{1.02}B$ but still inferior to $Nd_2Fe_{14}B$. It first increases with Ni substitution, when Ni content is below 0.6 at.% (x≤0.102). Then, M_s drops at a rate of 9.4 emu/g per 1 at.% Ni after doping with Ni between 0.6 at.% and 2.4 at.% (0.102≤x≤0.408). Since the Cu content in $Ce_2Fe_{12.98-x-y}Co_{1.02}Ni_xCu_yB$ does not vary considerably, such a decline in the value of M_s may be due to the different site occupancies of Ni at Fe sites. So far, the combination of Ni and Cu demonstrates a significant improvement in the saturation magnetization.

The anisotropy field of $Ce_2Fe_{12.98}Co_{1.02}B$ drops after the individual substitution of Ni or Cu for Fe atoms as shown in Table 5.6 and Figure 5.6 (b). Through the combined substitution of both Ni and Cu in $Ce_2Fe_{12.98-x-y}Co_{1.02}Ni_xCu_yB$ in the range of 0≤x≤0.41, y≈0.119, the H_a did not change significantly and appeared to be constant at around 23.5 kOe. It is worth noting that both individual and combined substitution have a similar influence on the anisotropy field and the results are comparable to each other, but in fact, they are lower than that of dopant-free $Ce_2Fe_{12.98}Co_{1.02}B$, dopant-free $Ce_2Fe_{14}B$ and much lower than $Nd_2Fe_{14}B$ as can be seen in Figure 5.6 (b).

By dissolving around 0.8 at.% Cu (x=0.136) in $Ce_2Fe_{12.98-x}Co_{1.02}Cu_xB$, the highest Curie temperature of 318°C is achieved. It shows a significant increase as compared to the 234°C of dopant-free $Ce_2Fe_{12.98}Co_{1.02}B$ and 151°C [4] of dopant-free $Ce_2Fe_{14}B$. After the combined substitution of Ni and Cu, the T_c of $Ce_2Fe_{12.98-x-y}Co_{1.02}Ni_xCu_yB$ is measured to be around 282±3°C which is similar to the T_c of Ni-doped $Ce_2Fe_{12.98}Co_{1.02}B$ at $0.51 \leq x \leq 1.19$ and $Nd_2Fe_{14}B$, but lower than that of Cu-doped $Ce_2Fe_{12.98}Co_{1.02}B$ as can be seen in the Figure 5.6 (c). Nevertheless, the T_c of (Ni, Cu)-doped $Ce_2Fe_{12.98}Co_{1.02}B$ increased almost 50°C compared to that of dopant-free $Ce_2Fe_{12.98}Co_{1.02}B$.

Chapter 6: Magnetic force microscopic study of magnetic $Ce_2(Fe, Co)_{14}B$, and its modifications by Ni and Cu

Microstructural aspects have a strong influence on the magnetic coercivity and remanence. An important attribute in explaining the improvements in the magnetic properties is the magnetic domains morphology and interaction which depend on the domain size and domain wall energy [130]. Besides the main magnetic matrix phase, some minor phases are also required at the grain boundaries to pin the domain wall movement which could also affect the extrinsic magnetic properties [131]. For the bulk materials, only the magnetic structure near the surface of the samples can be investigated. Unlike thin films, where it is generally assumed that the observed domain boundary walls continue through the depth of the sample, it is more complicated to interpret the domain behavior in the interior of the bulk samples [132, 133]. However, the MFM's tip stray field does not modify the magnetic state of bulk sample which could present a good approximation of the near surface magnetic structure [133]. Also, the domain structure evolved in thin films does not accurately represent the domain structure in bulk materials which are suitable for permanent magnets [132]. Additionally, the magnetic properties of thin films were found changing with the annealing temperature, which makes it difficult to evaluate the relation between magnetic domain structure and magnetic property [134, 135]. Hence, it is preferable to study domain structures of permanent magnet in bulk forms.

The intrinsic magnetic properties of $Ce_2Fe_{14-x}Co_xB$ have been determined and reported in [140]. So far, there is lack of magnetic domain structure investigations of $Ce_2Fe_{14-x}Co_xB$. Therefore, domain structure and domain wall energy of $Ce_2Fe_{14-x}Co_xB$ are studied here. In this work, the domain size has been measured combining magnetic force microscopy (MFM) with diffusion couple and key alloys. By applying MFM on diffusion couples, the influence of Co on the domain size variation of $Ce_2Fe_{14-x}Co_xB$ can be readily understood. Key alloys are designed to confirm the results obtained from the diffusion couple and to understand the magnetic domain morphology of $Ce_2Fe_{14-x}Co_xB$. This thesis also attempts to understand the effects of Ni and Cu on the domain size and domain wall energy of $Ce_2Fe_{14-x}Co_xB$.

6.1 Domain morphology and domain size

The solubility limits of Co in $Ce_2Fe_{14-x}Co_xB$ was measured as 28 at.% (x=4.76) at 900°C. In order to study the influence of Co content on the domain width (D_w) of $Ce_2Fe_{14-x}Co_xB$, MFM is

used to scan the diffusion layers of DC2. The chemical compositions across the diffusion layers and the corresponding phases that formed in the diffusion layers are listed in Table 6.1 and the microstructure is shown in Figure 6.1.

Table 6.1. Chemical compositions across DC2 and the corresponding phases.

Layer	Composition (at. %)				Corresponding Phase
	Ce	Fe	Co	B	
1	12	82-60	0-22	6	$Ce_2(Fe, Co)_{14}B$
	0	100-82	0-18	0	α-(Fe, Co)
2	15	27-17	42-52	16	$Ce(Co, Fe)_4B$
	0	82-37	18-63	0	α-(Fe, Co)
3	0	35-33	65-67	0	α-(Fe, Co)
	16	6-1	63-68	15	$Ce(Co, Fe)_4B$
	11	14	75	0	$Ce_2(Co, Fe)_{17}$
4	0	11-0	89-100	0	γ-(Fe, Co)
	11	14-0	75-89	0	$Ce_2(Co, Fe)_{17}$

The backscattered electron (BSE) image of the diffusion layers is presented in Figure 6.1 (a). Four layers formed after annealing at 900°C for 25 days. The compositions of the formed phases were determined using WDS analysis. The grey phase in layer 1 is identified as $Ce_2(Fe, Co)_{14}B$ with variable Co content. A WDS compositional profile of $Ce_2(Fe, Co)_{14}B$ in the diffusion couple is shown in Figure 6.1 (b). Based on this diffusion couple, the quaternary solid solubility of Co in $Ce_2Fe_{14}B$ is 22 at.%. This is not the maximum solubility which is obtained more accurately using key alloys, as discussed in Chapter 4. And the $Ce_2(Fe, Co)_{14}B$ is in equilibrium with α-(Fe, Co). $Ce(Co, Fe)_4B$ (light regions) and α-(Fe, Co) (dark regions) were found in layer 2. Layer 3 contains α-(Fe, Co), $Ce(Co, Fe)_4B$ and $Ce_2(Co, Fe)_{17}$ phases. γ-(Fe, Co) and $Ce_2(Co, Fe)_{17}$ are found in layer 4. Details of phase equilibria in the Ce-Fe-Co-B system can be found in Chapter 4.

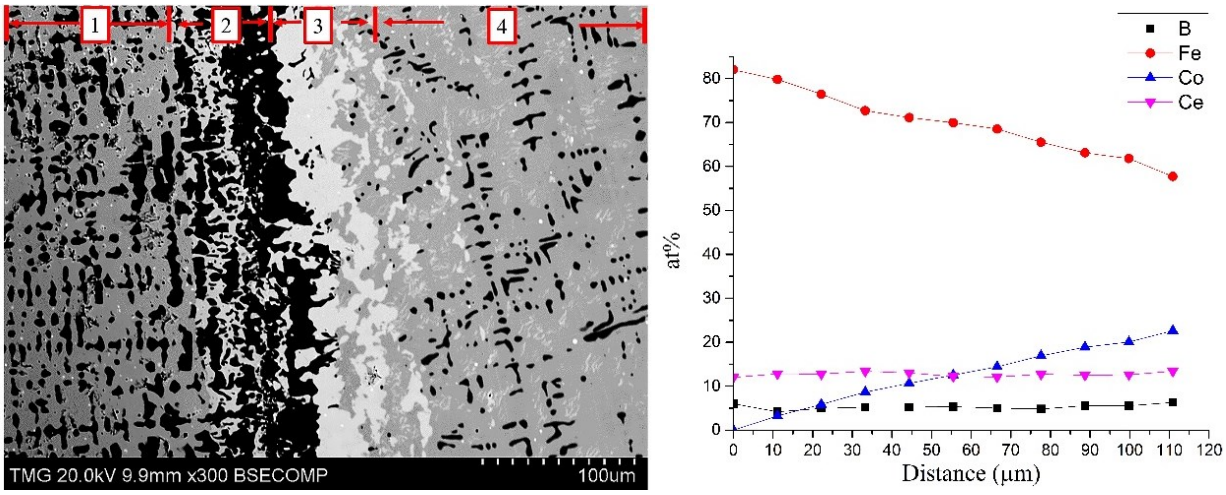

(a) (b)

Figure 6.1. (a) BSE image of DC2; (b) WDS compositional profile of $Ce_2(Fe, Co)_{14}B$ in layer 1.

Four MFM images for $Ce_2Fe_{14-x}Co_xB$ with different Co content are shown in Figure 6.2. The strength of the near-surface stray fields were observed. MFM tests were first applied on the interface between layers 1 and 2. Then the tip was moved around 40 μm towards layer 1 to capture the second image where the Co content is around 14 at.% in $Ce_2Fe_{14-x}Co_xB$ (x=2.38). Moving another 40 μm toward the edge of layer 1, the third MFM image was acquired when Co content is about 6 at.%. The last MFM test was performed at the edge of layer 1 where negligible Co could be found in $Ce_2Fe_{14}B$.

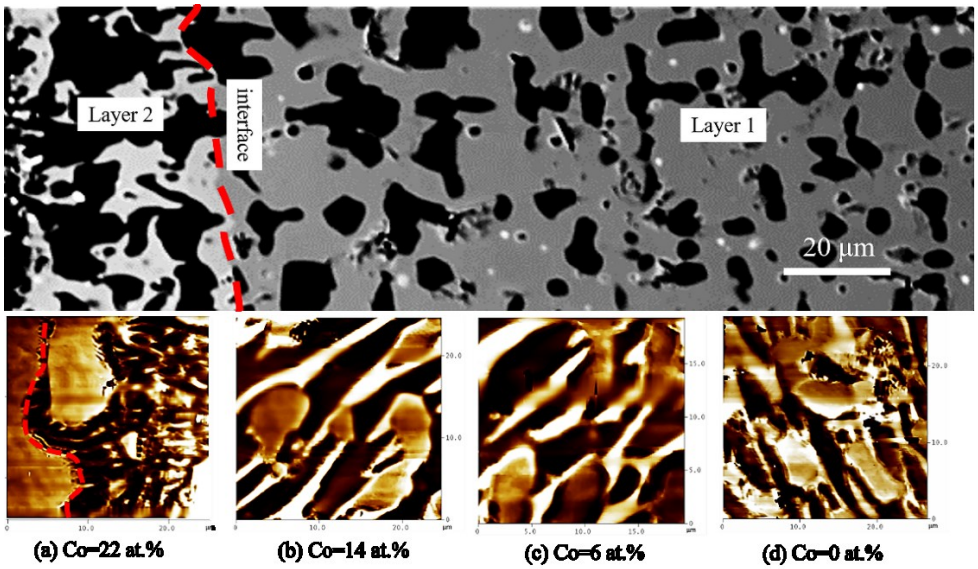

Figure 6.2. Microstructure (top) and four MFM images (a-c) obtained from layer 1 to the interface with layer 2 of DC2.

The observed MFM contrast mechanism depends on the effective magnetic interaction gradient between the tip and the sample [131]. The dark image contrast indicates that the attractive interaction and the negative phase shift both occur. Whereas, the positive phase shift and the bright image contrast result when repulsive interaction takes place [131]. During the MFM analysis, the phase shift ($(\Delta\Phi)_{rms}$) of the tip oscillation is directly proportional to the second derivative of the vertical component of the stray fields emerging from the surface of the sample [136]. Therefore, phase shift can give an indication of the effective magnetic moment of the sample such as the *z*-component of the stray field which is generally related to the saturation magnetization (M_s) [137]. Applying surface morphology analysis on these MFM images, the root mean square (RMS) values of phase shift are measured, which can be used to represent the contrast of the magnetic force images. In general, for the MFM images with the same data scale, sharper color contrast corresponds to larger RMS values of phase shift $(\Delta\Phi)_{rms}$ [137]. Since the four MFM images from the diffusion couple were captured through consecutive tests and testing conditions were maintained, the influence of Co content on the phase shift of $Ce_2Fe_{14-x}Co_xB$ could be interpreted which is presented in Figure 6.3 (a). The saturation magnetizations of $Ce_2Fe_{14-x}Co_xB$ at 6, 14 and 22 at.% Co (x=1.02, 2.38, 3.74) are determined using key alloys and presented in this figure. It has been found that the phase shift and saturation magnetization all increase with the Co content in $Ce_2Fe_{14-x}Co_xB$. Also, by comparing the relations between phase shift and saturation magnetization of $Ce_2Fe_{14-x}Co_xB$ as shown in Figure 6.3 (b), they almost follow a linear trend where higher $(\Delta\Phi)_{rms}$ value corresponds to larger saturation magnetization of $Ce_2Fe_{14-x}Co_xB$. Therefore, determining $(\Delta\Phi)_{rms}$ values in the MFM analysis could be used as an assessment for the saturation magnetization of magnetic $Ce_2Fe_{14-x}Co_xB$ materials.

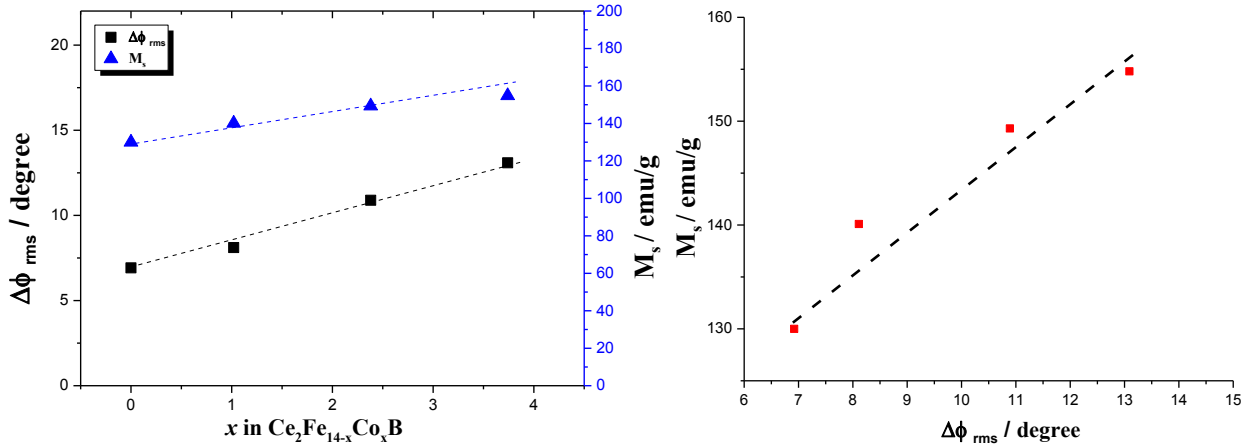

(a) (b)

Figure 6.3. (a) Phase shift and saturation magnetization of $Ce_2Fe_{14-x}Co_xB$ as a function of Co concentration; (b) saturation magnetization of $Ce_2Fe_{14-x}Co_xB$ as a function of phase shift.

Domain width measurement was carried out using the stereological method proposed in [131]. The effective domain width can be defined as the ratio between a test area and the total domain wall length in this area. The intersections of the domain walls with arbitrary test lines are counted and evaluated to calculate the effective domain width [131]. According to [131], the average domain width D_w is determined using the following equation:

$$D_w = \frac{2l}{\pi n} \qquad (2)$$

where l is the total length of the test lines and n is the number of intersections of the test lines with domain walls. The length of test line and the number of intersections can be obtained from section analysis, an example is shown in Figure 6.4. The MFM images were enhanced via Nanoscope Analysis software [138] to remove the artifacts during the scans. Then, the clean image option was used to remove some streaks and noise which could affect the image interpretation. Sharpening process was done to enhance the contrast and to provide a clearer image. Each image was subjected to 20 random direction test lines to cover all the test area. The measurements were repeated two times for each MFM image. The differences between the two tests were less than 0.03 μm.

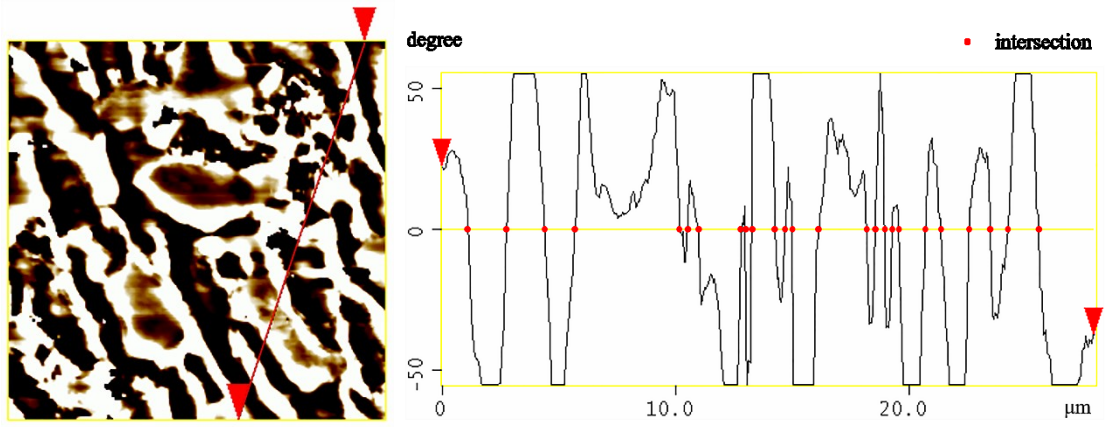

(a) (b)

Figure 6.4. (a) A random direction test line superimposed to apply section analysis; (b) section analysis results of the test line.

The influence of Co content on the domain width of $Ce_2Fe_{14-x}Co_xB$, obtained using the diffusion couple, is summarized in Table 6.2. It can be seen that domain width of $Ce_2Fe_{14-x}Co_xB$ decreased with Co content at 0.02 μm per 1 at.%. Domain width could be related to the size of magnetic crystal [139]. By substituting different amount of Co, the volume of $Ce_2Fe_{14-x}Co_xB$ crystal decreased with Co content [104] as shown in Figure 6.5. The domain width decreased correspondingly with Co content as can be seen in Table 6.2.

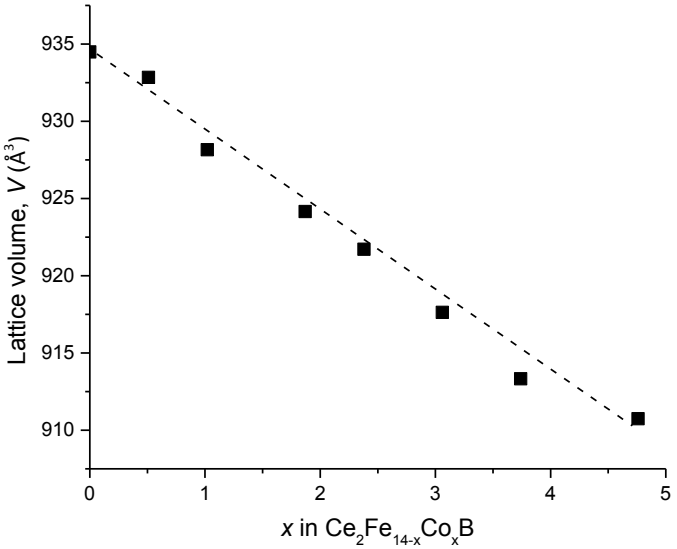

Figure 6.5. Lattice volume V of $Ce_2Fe_{14-x}Co_xB$ with x.

Table 6.2. Influence of Co content on average surface magnetic domain width of $Ce_2Fe_{14-x}Co_xB$.

x in $Ce_2Fe_{14-x}Co_xB$	D_w (μm)
0	1.19
1.02	1.03
2.38	0.98
3.74	0.79

Four key alloys (KAs 18, 19, 21 and 23) were used to confirm the domain width results obtained from the diffusion couple and to study the domain structure as well as to measure the domain wall energy. $Ce_2Fe_{14-x}Co_xB$ at 6 at.% Co (x=1.02) in KA 19 was reported to have the highest anisotropy field (H_a=29.3 kOe) in the $Ce_2Fe_{14-x}Co_xB$ ($0 \leq x \leq 4.76$) system [140]. Therefore to understand the effects of Ni and Cu on the domain width of $Ce_2Fe_{14-x}Co_xB$, KAs 26, 30 and 33 were selected and the Co content is kept the same (6 at.%) in order to be able to compare with KA 19. In KAs 26 and 30, about 1 at.% of Ni or Cu is added to replace Fe in the $Ce_2Fe_{14-x}Co_xB$ solid solution. Both Ni and Cu are added in KA 33 to compare the domain width variations with KAs 19, 26 and 30. After annealing at 900°C for 25 days, dominating magnetic phases (over 80 wt.%) were obtained in all the samples with limited amount of impurities such as α-(Fe, Co). Based on the WDS analysis, α-(Fe, Co) was found to dissolve up to 20 at.% Co in KAs 18, 19, 21 and 23. The M_s of ferromagnetic α-(Fe, Co) at around 0, 10, 20, 30 at.% Co were reported in [50, 54] ranging from 205 to 225 emu/g. The M_s of $Ce_2Fe_{14-x}Co_xB$ were then calculated by equation 1, as will be discussed further below. The chemical compositions and domain widths of $Ce_2Fe_{14-x}Co_xB$ are listed in Table 6.3.

Table 6.3. Chemical compositions and average domain widths of the dominating magnetic phase in the key alloys.

Key alloy	Dominating magnetic phase	at%	x	y	z	D_w (μm)
KA 18	$Ce_2Fe_{14-x}Co_xB$	Co=3	0.51	-	-	1.14
KA 19	$Ce_2Fe_{14-x}Co_xB$	Co=6	1.02	-	-	1.01
KA 21	$Ce_2Fe_{14-x}Co_xB$	Co=14	2.38	-	-	0.97
KA 23	$Ce_2Fe_{14-x}Co_xB$	Co=22	3.74	-	-	0.77
KA 26	$Ce_2Fe_{14-x-y}Co_xNi_yB$	Co=6; Ni=1	1.02	0.17	-	1.39
KA 30	$Ce_2Fe_{14-x-z}Co_xCu_zB$	Co=6; Cu=0.8	1.02	-	0.136	0.71
KA 33	$Ce_2Fe_{14-x-y-z}Co_xNi_yCu_zB$	Co=6; Ni=1.2; Cu=0.7	1.02	0.20	0.119	0.99

In this work, the dimensionless reduced anisotropy constant or magnet quality factor (Q) is calculated for $Ce_2Fe_{14}B$ as 7.8 based on equation 3 [141]:

$$Q=K_1/2\pi M_s^2 \quad (3)$$

where K_1 is the first uniaxial magnetocrystalline anisotropy constant, which is reported to be 1.51×10^7 erg/cm^3 [22]; M_s is measured as 130 emu/g at 25°C in this study. The domain structure of ferromagnets or ferrimagnets is a result of minimizing the total energy. In a ferromagnet, the total energy is the sum of different energy contributions such as exchange energy, magnetostatic energy, magnetocrystalline anisotropy energy, domain wall energy and magnetoelastic energy [142]. Certain flux closure domains at the sample's surface has to form to decrease the magnetostatic energy. As for strong uniaxial ferromagnets (with Q>>1), such magnets normally have large magnetocrystalline anisotropy energy which inhibits the formation of flux closure domains at the sample's surface. As such, the stray field leaks out of the sample and the associated energy cannot be eliminated entirely. However, in order to minimize energy, an appropriate geometrical arrangements of the magnetic domains take place [141]. The magnetic domain structure is also related to the ratio between magnetocrystalline anisotropy energy and magnetostatic energy or stray field energy [141]. If the decrease in magnetostatic energy is greater than the energy needed to form magnetic domain walls, numerous surface magnetic domains will arise [141]. For the current uniaxial bulk polycrystalline samples which are in demagnetization

state and the magnetic moments are randomly oriented, the magnetic domain structures may vary in different directions.

For example, two MFM tests have been first carried out on the top surface of KA 18 as shown in Figure 6.6 (a). The bulk wavy stripe domains indicate that the magnetic moments at the surface are either parallel or antiparallel to the easy axis and are separated by 180º domain walls. The magnetostatic interaction energy between the stripe domains and the tip is not perturbed resulting in nearly straight domain walls. The second test was done on the same sample but on the side cross section as shown in the Figure 6.6 (b). The 3D view of the domain structure of side cross section is shown in Figure 6.6 (c). The stripe like domain of $Ce_2Fe_{14-x}Co_xB$ in Figure 6.6 (a) turns into the matrix maze like domain in Figure 6.6 (b), indicating that the magnetization of $Ce_2Fe_{14-x}Co_xB$ crystal at the cross section is perpendicular or near-perpendicular to the alignment axis. There are some domains whose magnetization in the surface is perpendicular to the alignments appearing as spikes and reverse spikes domains visible as small white or dark spots in Figure 6.6 (c). This typical domain formed due to a compromise between magnetostatic energy and domain wall energy. They follow the domain walls which could reduce the domain wall energy and generate a strong surface anisotropy, also may reduce the density of magnetostatic energy near the surface [143, 144]. The spike and reverse spike domains are associated with strong attractive and repulsive stray fields, respectively, which indicate high and low stray fields in the domain regions [144]. The MFM analysis on the top surface and side section of KA 18 is summarized by a schematic shown in Figure 6.6 (d). The *c*-axis is the magnetic easy axis and the branching bulk stripe domain of alternating interaction (attraction and repulsion) is revealed near the sample surface.

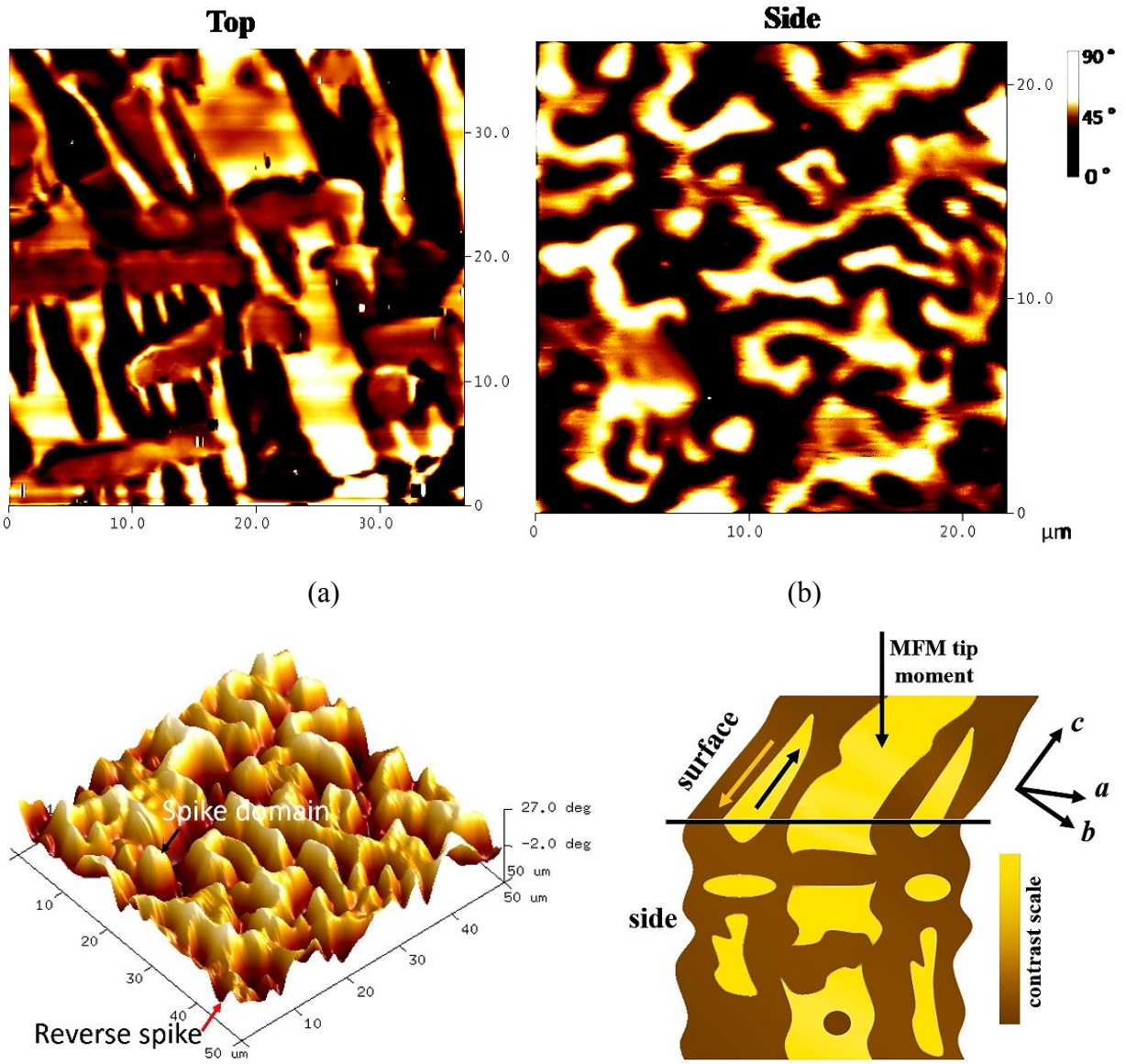

Figure 6.6. (a) MFM image of (a) top surface of KA 18; (b) side cross section of KA 18; (c) 3D view of magnetic domain structure of side section of KA 18 (d) schematic of magnetic domain along the magnetization direction.

The enhanced MFM image of KA 18 with superimposed 20 random selected test lines is presented in Figure 6.7. The domain widths of $Ce_2Fe_{14-x}Co_xB$ at Co=3 at.% (x=0.51) on the top surface and side cross section are similar and close to 1.14 μm. KAs 19, 21 and 234 were used to determine the influence of Co content on the domain size of $Ce_2Fe_{14-x}Co_xB$. The average domain widths of $Ce_2Fe_{14-x}Co_xB$ in KAs 19, 21 and 23 were measured as 1.01, 0.97 and 0.77 μm,

respectively, which supports the results obtained from the diffusion couple, confirming that the domain width of $Ce_2Fe_{14-x}Co_xB$ reduces with increasing Co content.

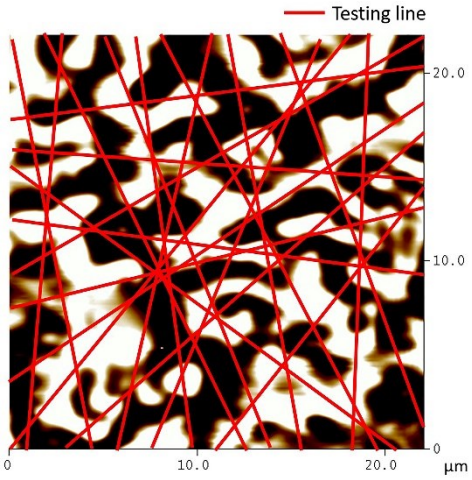

Figure 6.7. Enhanced MFM image of KA 18.

According to the experimental results of [145], the domain width is proportional to the saturation magnetization. The average surface domain width of Nd-Fe-B increased by partial substitution of Dy for Nd, which leads to increased magnetic anisotropy field and domain wall energy γ [145]. However, the saturation magnetization M_s decreased with the Dy content [145]. Such relation between domain width and saturation magnetization also obtained through analyzing $Ce_2Fe_{14-x}Co_xB$ with different Co contents in this study. The average surface domain width of $Ce_2Fe_{14-x}Co_xB$ as a function of x is shown in Figure 6.8 (a). It can be seen that the D_w reduces with Co content. Comparing the domain width and saturation magnetization of $Ce_2Fe_{14-x}Co_xB$ in Figure 6.8 (b), these two properties nearly follow a linear relation indicating that Co is effective in reducing the average domain width and improving the saturation magnetization of $Ce_2Fe_{14-x}Co_xB$. For $Ce_2Fe_{14-x}Co_xB$, the sample with smaller domain width has larger saturation magnetization, and higher phase shift in the MFM investigation.

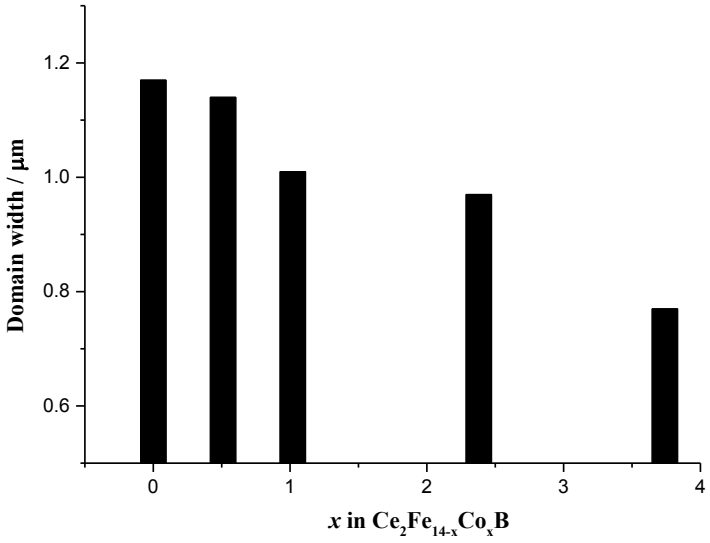

(a)

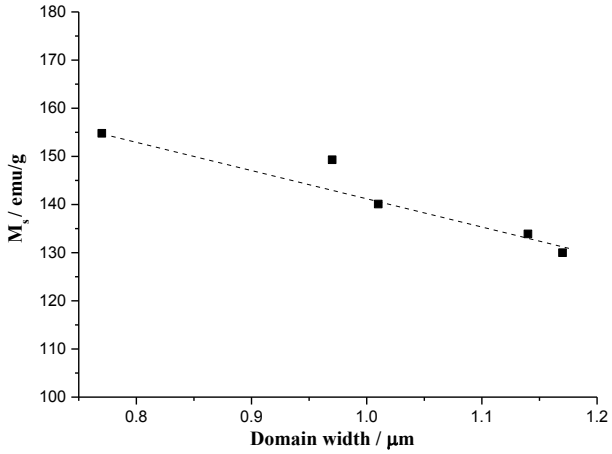

(b)

Figure 6.8. (a) Average surface domain widths of $Ce_2Fe_{14-x}Co_xB$ as a function of Co content; and (b) domain width versus saturation magnetization of $Ce_2Fe_{14-x}Co_xB$.

The enhanced MFM images of KAs 26, 30 and 33 are shown in Figure 6.9. The average domain width of $Ce_2Fe_{12.98-y}Co_{1.02}Ni_yB$ (y=0.17) is determined as 1.39 µm. In KA 30, the dominating $Ce_2Fe_{12.98-z}Co_{1.02}Cu_zB$ phase contained around 0.8 at.% Cu (z=0.136) and 6 at.% Co. After applying the same measurement on the enhanced MFM image in Figure 6.9 (b), the average domain width of $Ce_2Fe_{12.98-z}Co_{1.02}Cu_zB$ (z=0.136) is measured as 0.71 µm. The influence of adding both Ni and Cu on the domain width of $Ce_2Fe_{12.98-x}Co_{1.02}TM_xB$ (TM=Ni and/or Cu) is illustrated in Figure 6.9 (d). It can be concluded that a small amount of Ni, as low as 1 at.%, in $Ce_2Fe_{12.98-y}Co_{1.02}Ni_yB$ (y=0.17) increases the domain width. Whereas, Cu reduces the domain width of

$Ce_2Fe_{12.98-z}Co_{1.02}Cu_zB$ (z=0.136) at 6 at.% Co significantly. The domain width of sintered $Nd_2Fe_{14}B$ is reported in [144] as 0.71 μm in the perpendicular direction to alignment direction and 1 μm in the parallel direction. Due to the influence of Ni, the domain width of $Ce_2Fe_{12.98-y}Co_{1.02}Ni_yB$ (y=0.17) is greater than that of $Nd_2Fe_{14}B$. Ni and Ce atoms have large difference in electronegativity [128]. Hence substituting Ni for Fe will result in considerable electron transfer in the crystal, which could influence the exchange energy as well as the magnetic domain structure [129]. As can be seen in Figure 6.9 (a), the finer stripe domains indicate that the domain structure on grain surface are parallel to the easy direction. When both Ni and Cu are added, the domain width of $Ce_2Fe_{12.98-y-z}Co_{1.02}Ni_yCu_zB$ was determined as 0.99 μm when containing 1.2 at.% Ni (y=0.20) and 0.7 at.% Cu (z=0.119) at 6 at.% Co in KA 33, as shown in Figure 6.9 (c).

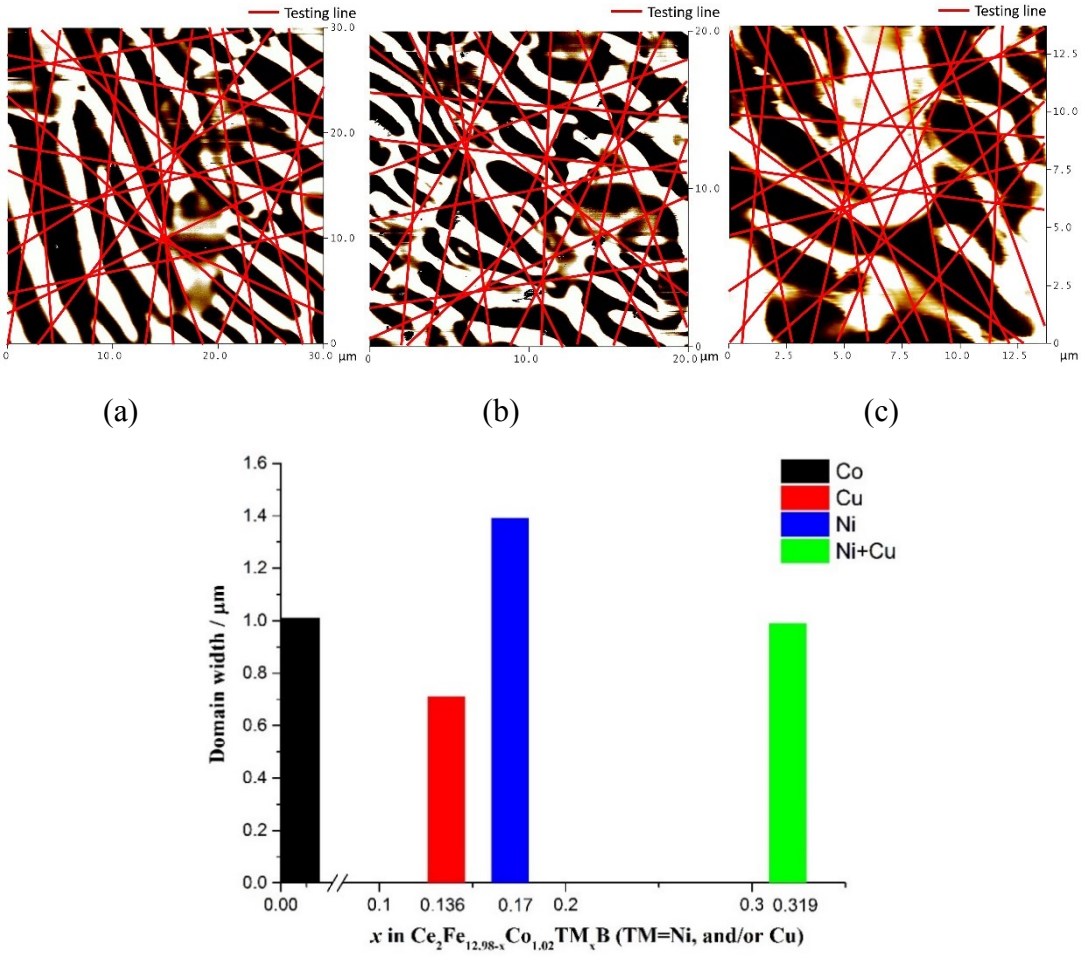

Figure 6.9. Enhanced MFM images of (a) KA 26; (b) KA 30; (c) KA 33; (d) domain width of $Ce_2Fe_{12.98-x}Co_{1.02}TM_xB$ (TM=Ni and/or Cu) as a function of x.

6.2 Domain wall energy

The domain wall energy is a fundamental magnetic parameter related to the coercivity, as it can be used as an approximation of the sum of the contributions from the exchange and magnetic anisotropy energies [145]. The knowledge of this parameter is also significant for understanding either nucleation or pinning is the dominant mechanism responsible for magnetic hardening [145]. The domain wall energy (γ_w) of $Ce_2Fe_{14}B$ as well as the magnetic phase in selected key alloys were calculated based on the following equation proposed by Bodenberger *et al.* [146]:

$$\gamma_w = \frac{D_w(M_s)^2}{4\pi\beta} \quad (4)$$

where D_w is the average domain width and M_s is the saturation magnetization of the magnetic phase. β is a surface structure coefficient, and its value has been previously determined as 0.31 for $SmCo_5$ and similar magnetic materials with high magnetocrystalline anisotropy (for which the relative magnetic anisotropy Q>>1) [146]. Therefore, this value has been used in this work. The mass saturation magnetizations of $Ce_2Fe_{14}B$, $Ce_2Fe_{14-x}Co_xB$ in KAs 18, 19, 21 and 23, and $Ce_2Fe_{12.98-y-z}Co_{1.02}Ni_yCu_zB$ in KAs 26, 30 and 33 were measured and converted into volume saturation magnetization using the density of $Ce_2Fe_{14}B$ as 7.56 g/cm^3 reported in [4]. The calculation results are listed in Table 6.4.

Table 6.4. Domain wall energy.

Sample	M_s (emu/cm^3) at 25ºC	D_w (μm)	γ_w (erg/cm^2)
$Ce_2Fe_{14}B$	982.8	1.17	29.0
KA 18	1012.3	1.14	30.0
KA 19	1059.3	1.01	29.1
KA 21	1128.7	0.97	31.7
KA 23	1170.3	0.77	27.1
KA 26	967.7	1.39	33.4
KA 30	1010.1	0.71	18.6
KA 33	1153.7	0.99	33.8

The domain wall energy of $Ce_2Fe_{14}B$ increased slightly from 29.0 to 30.0 erg/cm^2 after doping with 3 at.% Co and decreased back to 29.1 erg/cm^2 at 6 at.% Co. When containing 14 at.%

Co, the domain wall energy of the solid solution increased reaching 31.7 erg/cm^2. Although both saturation magnetization of $Ce_2Fe_{11.62}Co_{2.38}B$ (14 at.% Co) and $Ce_2Fe_{10.26}Co_{3.74}B$ (22 at.% Co) are similar, γ_w of $Ce_2Fe_{10.26}Co_{3.74}B$ is still lower than that of $Ce_2Fe_{11.62}Co_{2.38}B$, because the average domain width in $Ce_2Fe_{10.26}Co_{3.74}B$ is 20% smaller than in $Ce_2Fe_{11.62}Co_{2.38}B$. Although the addition of Ni exhibited an improvement in domain wall energy, Cu reduced the domain wall energy significantly. The domain wall energy of $Ce_2Fe_{12.98-y}Co_{1.02}Ni_yB$ with 1 at.% Ni (y=0.17) at 6 at.% Co was determined as 33.4 erg/cm^2. And the domain wall energy of $Ce_2Fe_{12.98-z}Co_{1.02}Cu_zB$ with 0.8 at.% Cu (z=0.136) at 6 at.% Co was measured as 18.6 erg/cm^2. The highest domain wall energy of $Ce_2(Fe, Co)_{14}B$ was achieved as 33.8 erg/ cm^2 when doping with 1.2 at.% Ni and 0.7 at.% Cu. Domain wall energy related to the domain wall thickness which is controlled by the short-range interactions between exchange energy and anisotropy energy [131]. Larger domain wall energy indicates that more domain walls are needed to split magnetic domains in the magnetic materials to minimize the magnetostatic energy of magnets [131]. Thus, the number of domain walls in KA 33 should be higher than KAs 19, 26 and 30. Based on the results obtained from KAs 19, 26, 30 and 33, the response surface plots of D_w and γ_w versus Ni and Cu content in $Ce_2Fe_{12.98-y-z}Co_{1.02}Ni_yCu_zB$ ($y \leq 0.20$, $z \leq 0.136$) at Co=6 at.% are presented in Figure 6.10. An appropriate response surface model could help understanding the relationship between several factors and the various magnetic properties. In summary, Ni substitution increases the domain width and the domain wall energy; whereas, Cu reduces the average domain width as well as domain wall energy in $Ce_2Fe_{12.98-z}Co_{1.02}Cu_zB$, which can be seen from Figure 6.10. Also, it can be seen from this figure that Cu substitution does not affect the domain wall energy significantly at the higher level of Ni content.

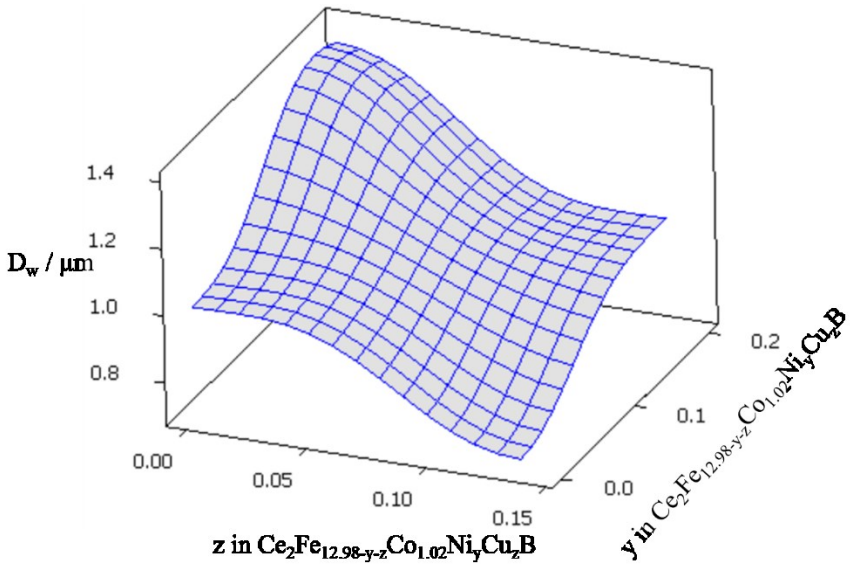

(a)

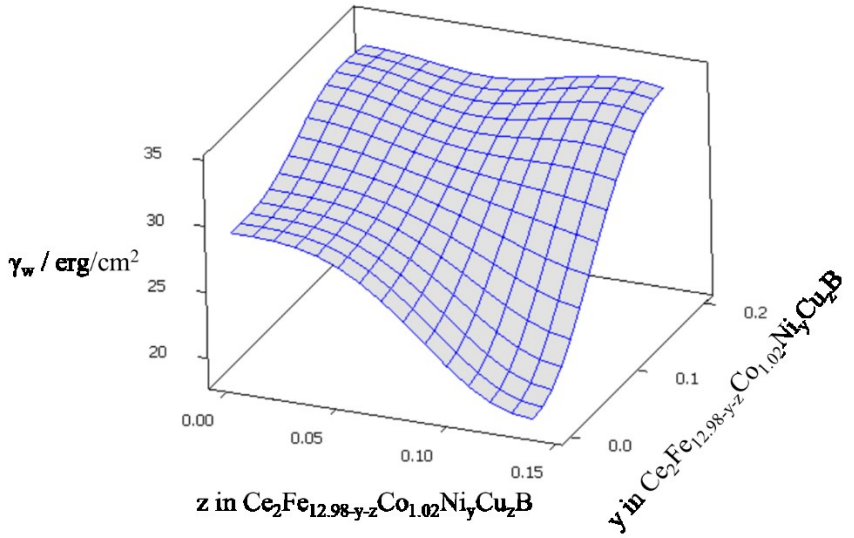

(b)

Figure 6.10. Response surfaces of (a) D_w; (b) γ_w versus Cu and Ni contents in $Ce_2Fe_{12.98-y-z}Co_{1.02}Ni_yCu_zB$ at Co=6 at.%.

Wyslocki *et al.* [130] used equation 4 to calculate the domain wall energy of $Y_2Fe_{13}MnB$ and $Y_2Fe_{12}Mn_3B$ as 22 erg/cm^2 and 3 erg/cm^2, respectively [130], which are lower than domain wall energy of $Ce_2(Fe, Co)_{14}B$-based magnets. Yazid *et al*. [144] reported the domain wall energy of sintered Nd-Fe-B magnet as 38 erg/cm^2 and 26 erg/cm^2 in two different alignment directions. Bulk $Ce_2(Fe, Co)_{14}B$-based magnets have similar domain width and domain wall energy as

sintered Nd-Fe-B magnet. This indicates that Ce-Fe-Co-B magnets could be considered as a promising candidate for permanent magnets application. In addition, the extrinsic magnetic properties (such as coercivity and remanence) can be measured to comprehend the influence of various additives on extrinsic magnetic properties of the Ce-Fe-Co-B magnets.

Chapter 7: Conclusions, contributions and recommendations for future works

7.1 Conclusions

High-throughput screening method is found to be effective in studying the phase equilibria in the Ce-Fe-Co-B system while exploring potential magnetic phases. Phase equilibria and homogeneity ranges have been determined in the Fe-Co rich side of the Ce-Fe-Co-B system at 900°C. Three magnetic phases are observed which are presented as $Ce_2Fe_{14-x}Co_xB$ ($0 \leq x \leq 4.76$), $CeCo_{4-x}Fe_xB$ ($0 \leq x \leq 3.18$) and $Ce_3Co_{11-x}Fe_xB_4$ ($0 \leq x \leq 6.66$). $Ce_2(Fe, Co)_{14}B$ exhibits stronger magnetic interaction than $Ce(Co, Fe)_4B$ and $Ce_3(Co, Fe)_{11}B_4$ based on the MFM analysis. Moreover, a non-magnetic $CeCo_{12-x}Fe_xB_6$ ($0 \leq x \leq 8.74$) is found to form in this system at 900°C. A new non-magnetic boron-rich solid solution with $Ce_{13}Fe_xCo_yB_{45}$ ($32 \leq x \leq 39$, $3 \leq y \leq 10$) chemical composition is observed in this quaternary system. The XRD pattern of this phase is extracted in this work.

Intrinsic magnetic properties of $Ce_2Fe_{14-x}Co_xB$ ($x \leq 4.76$) are studied at 25°C. From the current investigation, the substitution of Co for Fe in the $Ce_2Fe_{14}B$ enhances the M_s and T_c values. Whereas the H_a decreases proportionally with Co concentration. The crystal structure refinement of $Ce_2Fe_{14-x}Co_xB$ reveals that Co atoms show a preferred occupancy at 8*j2* site. After this site is fully occupied, Co atoms start occupying 16*k2*, 4*e* and 16*k1* sites, consecutively. The occupancy of Co at different sites is found to be related to the saturation magnetization of $Ce_2Fe_{14-x}Co_xB$ where the rate of increase in M_s drops after the 8*j2* site is fully occupied. The highest values of M_s and T_c of $Ce_2Fe_{14-x}Co_xB$ are measured to be 155.1 emu/g and 467°C at 28 at.% Co (x=4.76). However, the highest H_a is determined as 29.3 kOe at 6 at.% Co (x=1.02). The substitution of Ni or Cu alone for Fe is unfavorable to the M_s and H_a of $Ce_2Fe_{12.98}Co_{1.02}B$. However, the T_c of $Ce_2Fe_{12.98}Co_{1.02}B$ can be further improved through substituting by either of these two additives. In the case of Ni substitution, the highest M_s and H_a are found to be 135.2 emu/g and 26.6 kOe with T_c of 261°C, after doping with 0.7 at.% Ni (x=0.12). In contrast, when Cu is doped alone, the M_s and T_c are determined as 133.6 emu/g and 318°C with H_a of 23.7 kOe after dissolving 0.8 at.% Cu (y=0.136) in $Ce_2Fe_{12.98-y}Co_{1.02}Cu_yB$. A combination of Ni and Cu leads to an enhancement in M_s of $Ce_2Fe_{12.98-x-y}Co_{1.02}Ni_xCu_yB$ ($0.051 \leq x \leq 0.204$, $y \approx 0.119$) which is measured to fall in the range between 147 emu/g and 155 emu/g, with H_a and T_c measured to be close to 24 kOe and 280°C, respectively.

Combining magnetic force microscopy, diffusion couple and key alloys has been found to be effective in studying the magnetic domain structure, determining the domain width and calculating domain wall energy. The phase shift of $Ce_2Fe_{14-x}Co_xB$ increases with Co content which follows similar trend as its saturation magnetization. This indicates that higher phase shift in $Ce_2Fe_{14-x}Co_xB$ is associated with larger saturation magnetization. The domain width of $Ce_2Fe_{14-x}Co_xB$ drops with increasing Co concentration at 0.02 μm per 1 at.% Co. Domain wall energy is related to the domain size and saturation magnetization. The highest domain wall energy of $Ce_2Fe_{14-x}Co_xB$ is found to be 31.7 erg/cm^2 after substituting 14 at.% Co (x=2.38) for Fe. The combined influence of Ni and Cu on D_w and γ_w of $Ce_2Fe_{12.98-y-z}Co_{1.02}Ni_yCu_zB$ ($y\leq0.20$, $z\leq0.136$) at Co=6 at.% are presented by the response surfaces. Ni is found to increase the domain width and domain wall energy of $Ce_2Fe_{12.98-y}Co_{1.02}Ni_yB$. While the domain width does not change significantly when both Ni and Cu are added, the domain wall energy is at maximum.

7.2 Contributions

The Ce-Fe-Co-B quaternary system has been experimentally investigated for the first time. The phase equilibria of Ce-Fe-Co-B system is described and magnetic phases in the Fe-rich corner are identified. The intrinsic magnetic properties of $Ce_2(Fe, Co)_{14}B$ are determined, along with the influences of additives such as Ni and Cu on this magnetic phase are studied. In the present work, the following contributions have been achieved:

- The phase equilibria of Ce-Fe-Co-B system is comprehensively investigated and established at 900°C via diffusion couples and key alloys. Three magnetic compounds $Ce_2(Fe, Co)_{14}B$, $Ce(Co, Fe)_4B$ and $Ce_3(Co, Fe)_{11}B_4$, are identified. The solid solubilities of $Ce_2(Fe, Co)_{14}B$, $Ce(Co, Fe)_4B$ and $Ce_3(Co, Fe)_{11}B_4$ are determined as 28 at.% Co, 53 at.% Fe and 37 at.% Fe at 900°C, respectively, using WDS and XRD analysis.
- The intrinsic magnetic properties of $Ce_2(Fe, Co)_{14}B$ are determined by PPMS and TGA, including the effect of Ni and Cu additions on intrinsic magnetic properties of $Ce_2Fe_{12.98}Co_{1.02}B$. Ni and Cu are found to be effective in improving both M_s and T_c of $Ce_2Fe_{12.98}Co_{1.02}B$, while reducing the H_a. The combination of Ni and Cu exhibits a decent enhancement in M_s of $Ce_2Fe_{12.98}Co_{1.02}B$.
- Magnetic domain structures of magnetic $Ce_2(Fe, Co)_{14}B$, $Ce(Co, Fe)_4B$ and $Ce_3(Co, Fe)_{11}B_4$ are revealed via MFM. Domain width and domain wall energy of $Ce_2(Fe, Co)_{14}B$

are analyzed. The influences of Ni and Cu on the domain width and domain wall energy of $Ce_2(Fe, Co)_{14}B$ are also studied.

The following publications have been accomplished during the current study and they were used in this thesis:

1. **Tian Wang** and Mamoun Medraj, Intrinsic magnetic properties of $Ce(Co, Fe)_4B$ and $Ce_3(Co, Fe)_{11}B_4$, and their modifications by Ni and Cu. (submitted to *Applied Sciences*).
2. **Tian Wang** and Mamoun Medraj, Intrinsic magnetic properties of $Ce_2(Fe, Co)_{14}B$ and its modifications by Ni and Cu, *Journal of Alloys and Compounds*, Vol. 763, 2018, pp. 916-925.
3. **Tian Wang** and Mamoun Medraj, Magnetic force microscopic study of $Ce_2(Fe, Co)_{14}B$, and its modifications by Ni and Cu, *Journal of Magnetism and Magnetic Materials*, Vol. 460, 2018, pp. 95-103.
4. **Tian Wang**, Dmytro Kevorkov and Mamoun Medraj, Phase equilibria and magnetic phases in the Ce-Fe-Co-B system, *Materials*, Vol. 10, Issue 1, 2017, pp. 16-42.

7.3 Recommendations for future works

In the current study, the Ce-Fe-Co-B system has been experimentally investigated. The intrinsic magnetic properties of $Ce_2(Fe, Co)_{14}B$ are determined. The effects of Ni and Cu additives on the $Ce_2(Fe, Co)_{14}B$ are studied. However, it can be further improved through the following suggestions:

- In the current study, the phase equilibria of Ce-Fe-Co-B system are established at 900°C. Thermodynamic modelling is essential to construct a self-consistent database of this quaternary system. This can be achieved using CALPHAD approach relying on the experimental results obtained from the current work.
- The extrinsic magnetic properties (coercivity and remanence) of Ce-Fe-Co-B compounds are important to be determined.
- The effects of different fabrication processes such as melt-spinning and casting on the extrinsic magnetic properties of Ce-Fe-Co-B phases are also needed.
- The magnetic ordering and magnetic interaction of Ce-Fe-Co-B compounds should be analyzed for a better understanding through Mössbauer Spectroscopy and Neutron Diffraction.

- Attempting to replace rare earth elements completely in permanent magnets is of great interest. High throughput screening should be used to discover magnetic phases in metallic systems that do not contain rare earth elements.

References

[1] K. H. J. Buschow, New permanent magnet materials, *Materials Science Reports*, Vol 1, 1986, pp. 1-64.

[2] M. J. Kramer, R. W. Mccallum, I. A. Anderson, and S. Constantinides, Prospects for non-rare earth permanent magnets for traction motors and generators, *Journal of Materials*, Vol. 64, No. 7, 2012, pp. 752-763.

[3] S. Sugimoto, Current status and recent topics of rare-earth permanent magnets, *Journal of Physics D: Applied Physics*, Vol. 44, 2011, pp. 1-11.

[4] J. F. Herbst, $R_2Fe_{14}B$ materials: Intrinsic properties and technological aspects, *Reviews of Modern Physics*, Vol. 63, 1991, pp. 819-898.

[5] J. J. Croat, J. F. Herbst, R. W. Lee and F. E. Pinkerton, Pr-Fe and Nd-Fe-based materials: A new class of high-performance permanent magnets, *Journal of Applied Physics*, Vol. 55, 1984, pp. 2078-2082.

[6] M. Sagawa, S. Fujimura, M. Togawa and Y. Matsuura, New material for permanent magnets on a base of Nd and Fe, *Journal of Applied Physics,* Vol. 55, No. 6, 1984, pp. 2083-2087.

[7] H. R. Kirchmayr, Permanent magnets and hard magnetic materials, *Journal of Physics D: Applied Physics*, Vol. 29, 1996, pp. 2763-2778.

[8] U.S. Geological Survey, Metal prices in the United States through 2010: U.S. Geological Survey Scientific Investigations Report 2012, 2013, pp. 5188-5204.

[9] J. F. Herbst, M. S. Meyer and F. E. Pinkerton, Magnetic hardening of $Ce_2Fe_{14}B$, *Journal of Applied Physics*, Vol. 111, No. 7, 2012, pp. 1-3.

[10] E. J. Skoug, M. S. Meyer, F. E. Pinkerton, M. M. Tessema, D. Haddad, J. F. Herbst, Crystal structure and magnetic properties of $Ce_2Fe_{14-x}Co_xB$ alloys, *Journal of Alloys and Compounds*, Vol. 574, No. 15, 2013, pp. 552-555.

[11] Q. M. Lu, M. Yue, H. G. Zhang, M. L. Wang, F. Yu, Q. Z. Huang, D. H. Ryan and Z. Altounian, Intrinsic magnetic properties of single-phase $Mn_{1+x}Ga$ ($0 < x < 1$) alloys, *Scientific Reports***,** Vol. 5, 2015, pp. 17086-17091.

[12] C. D. Fuerst, J. F. Herbst and E. A. Alson, Magnetic properties of $Nd_2(Co_xFe_{1-x})_{14}B$ alloys, *Journal of Magnetism and Magnetic Materials*, Vol. 54-57, 1986, pp. 567-569.

[13] C. D. Fuerst and E. G. Brewer, Diffusion alloyed additives in die upset Nd-Fe-B magnets, *Journal of Applied Physics*, Vol. 69, No. 8, 1991, pp. 5826-5828.

[14] C. D. Fuerst, and E. G. Brewer, Enhanced coercivities in die-upset Nd-Fe-B magnets with diffusion-alloyed additives (Zn, Cu, and Ni), *Applied Physics Letters*, Vol. 56, 1990, pp. 2252-2254.

[15] J. M. D. Coey, Magnetism and magnetic materials, Cambridge University Press, New York, 2009.

[16] K. H. J. Buschow and F. R. De Boer, Physics of magnetism and magnetic materials, Kluwer Academic Publishers, New York, 2003.

[17] W. D. Callister and D. G. Rethwisch, Materials science and engineering: An introduction, 8th Edition, Wiley Global Education, New York, 2009.

[18] J. D. Schobel, H. H. Stadelmaier, The cobalt-boron two-component system, *Zeitschrift Fur Metallkunde*, Vol. 57, 1966, pp. 323-325.

[19] P. K. Liao and K. E. Spear, Ce-Fe-B system at 550°C, *Bulletin of Alloy Phase Diagrams*, Vol. 9, 1988, pp. 452-457.

[20] C. Lerner, M. Cadeville, Sur la solubilite du bore dans le cobalt, *Scipta Metallurgica*, Vol. 7, 1973, pp. 941–944.

[21] K. H. J. Buschow, Magnetic Properties of Borides. In: Matkovich V.I. (eds) Boron and Refractory Borides. Springer, Berlin, Heidelberg, 1977.

[22] S. Hirosawa, Y. Matsuura, H. Yamamoto, S. Fujimura, M. Sagawa and H. Yamauchi, Single crystal measurements of anisotropy constants of $R_2Fe_{14}B$ (R=Y, Ce, Pr, Nd, Gd, Tb, Dy and Ho), *Japanese Journal of Applied Physics*, Vol. 24, No. 10, 1985, pp. L803-L805.

[23] B. Hallemans, P. Wollants, J. R. Roos, Thermodynamic assessment of Fe-Nd-B phase diagram, *Journal of Phase Equilibria*. Vol. 16, 1995, pp. 137-149.

[24] B. Hallemans, P. Wollants, J. R. Roos, Thermodynamic reassessment and calculation of the Fe-B phase diagram, *Zeitschrift Fur Metallkunde*. Vol. 85, 1994, pp. 676-682.

[25] L. Kaufman, B. Uhrenius, D. Bimie, K. Taylor, Coupled pair potential, thermochemical and phase diagram data for transition metal binary systems-VII, *Calphad*, Vol. 8, 1984, pp. 25-66.

[26] H. Ohtani, M. Hasebe, K. Ishida, T. Nishizawa, Calculation of the Fe-C-B ternary phase diagram, *The Iron and Steel Institute of Japan*. Vol. 28, 1988, pp. 1043-1050.

[27] T. V. Rompaey, K. C. H. Kumar, and P. Wollants, Thermodynamic optimization of the B-Fe System, *Journal of Alloys and Compounds*, Vol. 334, 2002, pp. 173-181.

[28] E. C. Passamani, J. R. B. Tagarro, C. Larica, and A. A. R. Fernandes: Thermal studies and magnetic properties of mechanical alloyed Fe2B. J. Physics-Condensed Matter, Vol. 14, No. 8, 2002, pp. 1975–1983.

[29] P. K. Liao, K. E. Spear, M. E. Schlesinger, The B-Ce (Boron-Cerium) system, *Journal of Phase Equilibria*, Vol. 18, Issue. 3, 1997, pp. 280–283.

[30] P. Stecher, F. Benesovsky, H. Nowotny, Study of the alloy behavior of borides in the ternary system Cerium-Thorium (Uranium)-Boron, *Planseeber. Pulvermetall*. Vol. 13, 1965, pp. 37–46.

[31] K. E. Spear, Boron and refractory borides, Springer, New York, 1977, pp. 439-456.

[32] L. Brewer, D. L. Sawyer, D. H. Templeton, C. H. Dauben, A study of the refractory borides, Journal of the American Ceramic Society, Vol. 34, 1951, pp. 173-179.

[33] K. E. Spear, Phase diagrams, Materials science and technology, Academic Press, New York, 1976, pp. 91-159.

[34] A. U. Seybolt, An exploration of high boron alloys, *Metallurgical and Materials Transactions A*, Vol. 52, 1960, pp. 971–989.

[35] C. P. Wang, Y. Shi, D. Wang, Y. Lu, D.L. Zhao, X.J. Liu, Thermodynamic assessment of the B–Ce and B–Pr systems, *Calphad*, Vol. 41, 2013, pp. 150-155,

[36] Y. Khan, Intermetallic compounds in the cobalt-rich part of the R-cobalt systems (R=Ce, La, Ce-La), *Journal of the Less Common Metals*, Vol. 34, 1974, pp. 191-200.

[37] A. E. Ray, G. I. Hoffer, Phase diagrams for the Ce-Co, Pr-Co, and Nd-Co alloy systems, Proceedings of the 8th Rare Earth Research Conference, Reno, Nevada, April 19-22, 1970.

[38] K. H. J. Buschow, Rare-earth cobalt intermetallic compounds, *Philips Research Reports*, Vol. 26, 1971, pp. 49-64.

[39] C. H. Wu, Y. C. Chuang, X. M. Jin, X. H. Guan, Reinvestigation of the Ce-Co system, *Zeitschrift Fur Metallkunde*, Vol. 82, 1991, pp. 621-625.

[40] T. Massalski, P. R. Subramanian, H. Okamoto, L. Kacprzak, Binary Alloys Phase Diagrams, ASM, Materials Park, OH, 1990.

[41] X. Su, W. Zhang, Z. Du, A thermodynamic modelling of the Co-Ce system. *Journal of Alloys and Compounds*, Vol. 267, 1998, pp. 121-127.

[42] K. H. J, Buschow, Intermetallic compounds of rare-earth and 3d transition metals, *Reports on Progress in Physics*, Vol. 40, No. 10, 1977, pp. 1179-1256.

[43] K. A. Gschneidner Jr., M.E. Verkade, Selected Cerium Phase Diagrams, IS-RIC-7, 1974, United States.

[44] Y. Z. Chuang, C. H. Wu, Z. B. Shao, Investigation of the Ce-Fe binary system, *Journal of the Less common Metals*. Vol. 136, Issue. 1, 1987, pp. 147-153.

[45] X. Su and J. C. Tedenac, Thermodynamic Modeling of the Ternary Ce-Fe-Sb System: Assessment of the Ce-Sb and Ce-Fe Systems, *Calphad*, 2006, 30, p 455-460.

[46] L. Paolasini, P. Dervenagas, P. Vulliet, J. P. Sanchez, G. H. Lander, A. Hiess, A. Panchula, and P. C. Canfield, Magnetic response function of the itinerant ferromagnetCeFe2, *Physics Review B*, Vol. 58, No. 18, 1998, pp. 12117–12124.

[47] Y. Janssen, S. Chang, A. Kreyssig, A. Kracher, Y. Mozharivskyj, S. Misra, and P. C. Canfield, Magnetic phase diagram of Ce_2Fe_{17}, *Physics Review B*, Vol. 76, No. 5, 2007, pp. 054420.

[48] W. Iwasieczko, A. G. Kuchin, L. Folcik, and H. Drulis, Effect of pressure and Mn substitution on magnetic ordering of $Ce_2Fe_{17-x}Mn_x$ (x = 0, 1), *Journal of Alloys and Compounds*, Vol. 406, 2005, pp. 155–159.

[49] T. Nishizawa, K. Ishida, The Co-Fe (Cobalt-Iron) system, *Bulletin of Alloy Phase Diagrams*, Vol. 5, 1984, pp. 250-259.

[50] I. Ohnuma, H. Enoki, O. Ikeda, R. Kainuma, H. Ohtani, B. Sundman, and K. Ishida, Phase Equilibria in the Fe-Co Binary System, *Acta Materialia*, Vol. 50, 2002, pp. 379-393.

[51] A. F. Guillermet, Critical evaluation of the thermodynamic properties of the Iron-Cobalt system, *High Temp-High Pressures*, Vol. 19, 1987, pp.477-499.

[52] Y. Ustinovshikov and B. Pushkarev, Ordering and phase separation in alloys of the Fe-Co System, *Journal of Alloys and Compounds*, Vol. 424, 2006, pp. 145-151.

[53] H. Okamoto, Co-Fe (Cobalt-Iron), *Journal of Phase Equilibria and Diffusion*, Vol. 29, Issue. 4, 2008, pp. 383-384.

[54] F. Sánchez-De Jesús, A. M. Bolarín-Miró, C. A. Cortés Escobedo, G. Torres-Villaseñor, and P. Vera-Serna, Structural analysis and magnetic properties of FeCo alloys obtained by mechanical alloying, *Journal of Metallurgy*, Vol. 2016, 2016, Article ID: 8347063, 8 pages.

[55] R. S. Sundar and S. C. Deevi, Soft magnetic FeCo alloys: alloy development, processing and properties, *International Materials Review*, Vol. 50, 2005, pp. 157-192.

[56] N. S. Bilonizhko, B. Yu, ang N. S. Kuz'ma, Ce-Fe-B system, *Izvestiya Akademii Nauk SSSR, Neorganicheskie Materialy*, Vol. 8, No. 1, 1972, pp.183–184.

[57] O. M. Dub and Y. B. Kuz'ma, Ternary borides with the $Nd_2Fe_{14}B$ structure, *Soviet Powder Metallurgy and Metal Ceramics*, Vol. 25, No.7, 1986, pp. 572-575.

[58] A. Bezinge, H. F. braun, J. Muller and K. Yvon, Tetragonal rare earth (R) iron borides, $R_{1+x}Fe_4B_4$ ($x\approx0.1$) with incommensurate rare earth and iron substructures, *Solid state communication*, Vol. 55, Issue, 2, 1985, pp. 131-135.

[59] O. M. Dub, N. F. Chaban, and Y. B. Kuz'ma, New borides of $Pr_{5-x}Co_{2+x}B_6$-type structure, *Journal of Less Common Materials*, Vol. 117, 1986, pp. 297-303.

[60] V. Raghavan, G. V. Raynor, V. G. Rivlin, Phase diagrams of ternary iron alloys, ASM International, 1987, pp. 297-300.

[61] H. Putz and K. Brandenburg, Pearson's Crystal Data, Crystal Structure Database for Inorganic Compounds, CD-ROM software version 1.3.

[62] J. F. Herbst and W. B. Yelon, Crystal and magnetic structure of $Ce_2Fe_{14}B$ and $Lu_2Fe_{14}B$, *Journal of Magnetism and Magnetic Materials*, 1986, pp: 570-572.

[63] P. Rogl, J. C. Schuster, H. Nowotny, Phase equilibrium and compound formation in Fe-M(metal)-B-X(nonmetal) systems*, Boron in Steel Proceeding of the International Symposium*, Metallurgical Society of AIME, Milwaukee, 1979, pp. 33-43.

[64] G. Pradelli, C. Gianoglio, and E. Quadrini, The Co-Fe-B System in the presence of liquid, *Metall. Ital.,* 1981, Vol. 73(7-8), pp. 351-355, in Italian.

[65] F. J. J. V. Loo and J. A. V. Beek, Reactions and Phase Relations in the Fe-Ni-B and Fe-Co-B Systems, *Z. Metallkd*., Vol. 80(4), 1989, pp. 245-250.

[66] V. Raghavan, B-Co-Fe (Boron-Cobalt-Iron), *Journal of Phase Equilibria and Diffusion,* Vol. 33, No. 5, 2012, pp. 392-394.

[67] Y. Q. Liu, X. S. Zhao, J. Yang, and J. Y. Shen, Thermodynamic Optimization of the Boron-Cobalt-Iron System, *Journal of Alloys and Compounds*, Vol. 509, 2011, pp. 4805-4810.

[68] F. Pfeifer, C. Radeloff, Soft magnetic Ni-Fe and Co-Fe alloys - some physical and metallurgical aspects, *Journal of Magnetism and Magnetic Materials*, Volume 19, 1980, pp. 190-207.

[69] B. M. Concha, R.D. Zysler, and H. Romero, Magnetization enhancement in Fe–Co–B alloy nanoparticles, *Physica B: Condensed Matter*, Vol. 384, Issues 1–2, 2006, pp. 274-276,

[70] J. K. Critchley, Low melting point alloys of cerium with iron, cobalt and plutonium, U. K. At. Energy Auth., Harwell Lab., Memo AERE-M, Vol. 488, 1959, pp. 1-7.

[71] ASM Alloy Phased Diagram Database, (http://www1.asminternational.org/AsmEnterprise/APD/BrowseAPD.aspx).

[72] R. C. Mansey, G. V. Raynor and I. R. Harris, Rare-earth intermediate phases VI. Pseudo-binary systems between cubic laves phases formed by rare-earth metals with iron, cobalt, nickel, aluminum and rhodium, *Journal of the Less-Common Metals*, 1968, pp. 337-347.

[73] I. R. Harris, G. Longworth, X-ray and Mössbauer studies of the pseudo-binary system $Ce(Fe_{1-x}Ni_x)_2$, *Journal of the Less-Common Metals*, Vol. 45, No. 2, 1976, pp. 63-77.

[74] G. Longworth and I. R. Harris, Mössbauer effect study of the pseudo-binary system $Ce(Fe_{1-x}Co_x)_2$, *Journal of the Less-Common Metals*, Vol. 41, 1975, pp. 175-185.

[75] G. E. Fernández, M. G. Berisso, O. Trovarelli, J. G. Sereni, Comparative study of the ferro-antiferromagnetic transition in $Ce(Fe,Co)_2$ and $Ce(Fe,Al)_2$, *Journal of Alloys and Compounds*, Volume 261, Issues 1–2, 1997, pp. 26-31.

[76] H. Fujii, M. V. Satyanarayana, and W. E. Wallace, Magnetic and crystallographic properties of substituted $Ce_2Co_{17-x}T_x$ compounds (T = Ti, V, Cr, Mn, Fe, Cu, Zr, and Hf), *Journal of Applied Physics,* 1982, pp. 2371.

[77] X. Xu and S. A. Shaheen, Structural and magnetic properties of rare-earth iron $Ce_2(Fe_{1-x}Co_x)_{17}N_y$ series, *Journal of Applied Physics,* Vol. 73, No. 10, 1993, pp. 5896-5898.

[78] H. C. Bilonizhko, N. S. Kuz'ma, B. Yu, Cerium-Cobalt-Boron system, *Izvestiya Akademii Nauk SSSR, Neorganicheskie Materialy*, 1974, pp. 265-269.

[79] Y. B. Kuz'ma, N. S. Bilonizhko, S. I. Mykhalenko, G. F. Stepanchikova, N. F. Chaban, The interaction of transition and rare earth metals with boron. *Journal of Less Common Materials*, Vol. 67, 1979, pp. 51-57.

[80] M. Jurczyk, Crystallographic and Magnetic Characteristics of the $Ce_3Co_{20}B$ Compound. *Physica Status Solidi A*, Vol. 100, 1987, pp. K173-K176.

[81] Y. B. Kuz'ma, G. V. Chernyak, N. F. Chaban, New Borides of Rare-Earth Metals with the Structure of $SrNi_{12}B_6$ Type. *Dopov. Akad. Nauk Ukr. RSR (Ser. A)* 1981, pp. 12-80.

[82] O. M. Dub, R. V. Skolozdra, Y. B. Kuz'ma, N. S. Dubenko. Magnetic and electrical parameters of ternary rare-earth borides containing cobalt and nickel. *Inorganic Materials.* Vol. 26, 1990, pp. 1034-1037.

[83] H. Gencer, N. Kervan, A. Gencer, M. Gunes, S. Atalay, Magnetocaloric effect in CeCo4B compound, *Journal of Alloys and Compounds*, Vol. 466, Issues 1–2, 2008, pp. 1-4.

[84] H. Ido, H. Asano, G. Kito, N. M. Hong, G. Hilscher, R. Ballou, Magnetic properties of the $Ce_2Co_7B_3$, *Journal of Magnetism and Magnetic Materials*, Vol. 140, 1995, pp. 955-956.

[85] M. Jurczyk, A. T. Pedziwiatr and W. E. Wallace, Magnetic studies of $RCo_{12}B_6$ compounds (R=Y, Ce, Pr, Nd, Sm, Gd and Dy), *Journal of Magnetism and Magnetic Materials*, Vol. 67, 1987, pp. L1-L3.

[86] F. Bolzoni, F. Leccabue, O. Moze, L. Pareti, M. Solzi, Magnetocrystalline anisotropy of Ni and Mn substituted $Nd_2Fe_{14}B$ compounds, *Journal of Magnetism and Magnetic Materials*, Vol. 67, Issue 3, 1987, pp. 373-377.

[87] O. M. Ragg, I. R. Harris, A study of the effects of the addition of various amounts of Cu to sintered Nd-Fe-B magnets, *Journal of Alloys and Compounds*, Vol. 256, Issue 1, 1997, pp. 252-257.

[88] H. C. Ku and L. S. Yen, Magnetic properties of the new permanent magnet compounds $Nd_2(Fe_{0.9}M_{0.1})_{14}B$ (M = Sc, Ti, V, Cr, Mn, Co, Ni), *Journal of Less Common Materials,* Vol. 127, 1987, pp. 43–48.

[89] B. Podmiljsak, J. H. Kim, P. J. McGuiness, S. Kobe, Influence of Ni on the magnetocaloric effect in nanoperm-type soft-magnetic amorphous alloys, *Journal of Alloys and Compounds*, Vol. 591, No. 5 2014, pp. 29-33.

[90] M. Shimotomai, Y. Fukuda, A. Fujita and Y. Ozaki, Corrosion-resistance Nd-TM-B magnet, IEEE Transactions on Magnetics, Vol. 26, Issue 5, 1990, pp. 1939-1941.

[91] Y. Fukuda, A. Fujita and M. Shimotomai, Magnetic properties of monocrystalline Nd_2(Fe, Co, Ni)$_{14}$B, *Journal of Alloys and Compounds*, No. 193, 1993, pp. 256-258.

[92] W. Tang, Y. Zhang and G. C. Hadjipanayis, Effect of Ni substitution on the microstructure and coercivity of $Sm(Co_{bal}Fe_{0.1}Ni_yZr_{0.04})_{8.5}$ magnets, *Journal of Applied Physics*, Vol. 91, No. 10, 2002, pp. 7896-7898.

[93] A. S. Kim and F. E. Camp, High performance NdFeB magnets (Invited), *Journal of Applied Physics*, Vol. 79, Issue 8, 1996, pp. 5035-5039.
[94] H. Okamoto, Phase Diagram of Binary Iron Alloys, ASM International, Materials Park, OH, 1993, pp. 131-137.
[95] M. Palumbo, S. Curiotto, L. Battezzati, Thermodynamic analysis of the stable and metstable Co-Cu and Co-Cu-Fe phase diagrams *Calphad*, Vol. 30, 2006, pp. 171–178.
[96] T. Wang, D. Kevorkov, A. Mostafa, and M. Medraj, Experimental investigation of the phase equilibria in the Al-Mn-Zn system at 400°C, *Journal of Materials*, Vol. 2014, 2014, pp. 1-13.
[97] X'Pert HighScore Plus, PANalytical B.V. Almelo, the Netherlands, Version: 2.2b (2.2.2), 2006.
[98] Y. Liu, Magnetic dissipation force microscopy, PhD thesis, McGill University, Canada, 1997.
[99] P. Grütter, H. J. Mamin and D. Rugar, *Magnetic Force Microscopy*, Scanning Tunneling Microscopy II, Vol. 28, Springer, Berlin, 1992.
[100] U. Hartmann, Magnetic force microscopy. Annual Review of Materials Science. Vol. 29, 1999, pp. 53–87.
[101] U. Hartmann, Magnetic force microscopy: Some remarks from the micromagnetic point of view, *Journal of Applied Physics*, Vol. 64, 1988, pp. 1561-1564.
[102] D. Rugar, H. J. Mamin, P. Guethner, S. E. Lambert, J. E. Stern, I. McFadyen and T. Yogi, Magnetic force microscopy: General principles and application to longitudinal recording media, *Journal of Applied Physics*, Vol. 68, No. 3, 1990, pp. 1169-1183.
[103] J. Fidler, J. Bernardi, T. Schrefl, Permanent magnets - New microstructural aspects, *Scripta Materialia*, Vol. 33, Issues 10–11, 1995, pp. 1781-1791.
[104] T. Wang, D. Kevorkov and M. Medraj, Phase Equilibria and Magnetic Phases in the Ce-Fe-Co-B System, *Materials*, Vol. 10, No. 1, 2017, pp. 16-42.
[105] G. Asti and S. Rinaldi, Nationaliticity of the magnetization curve: Application to the measurement of anisotropy in polycrystalline samples, *Physical Review Letters*, Vol. 28, No. 24, 1972, pp. 1584–1586.
[106] G. Asti and S. Rinaldi. Singular points in the magnetization curve of a polycrystalline ferromagnet, *Journal of Applied Physics*, Vol. 45, No. 8, 1974, pp. 3600–3610.

[107] X. Liu, D. H. Ryan, M. Wang, Q. Lu, and H. Zhang, Experimental and first-principles determination of the magnetocrystalline anisotropy in Mn_xGa. *AIP Advances*, Vol. 7, 2017, pp. 56216-56221.

[108] R. Skomski, G. C. Hadjipanayis, and D. J. Sellmyer, Effective demagnetizing factors of complicated particle mixtures, *IEEE Transactions on Magnetics*, Vol. 43, No. 6, 2007, pp. 2956–2958.

[109] L. Yang, K. Dayal, Effect of lattice orientation, surface modulation, and applied fields on free-surface domain microstructure in ferroelectrics, *Acta Materialia*, Vol. 59, Issue 17, 2011, pp. 6594-6603.

[110] A. R. Denton, N. W. Ashcroft, Vegard's Law. *Physical Review A*. Vol. 43, 1991, pp. 3161–3164.

[111] K. Maaz, A. Mumtaz, S.K. Hasanain, A. Ceylan, Synthesis and magnetic properties of cobalt ferrite ($CoFe_2O_4$) nanoparticles prepared by wet chemical route, *Journal of Magnetism and Magnetic Materials*, Vol. 308, 2007, pp. 289-295.

[112] K. Orimoloye, D.H. Ryan, F. E. Pinkerton and M. Medraj, Intrinsic Magnetic Properties of $Ce_2Fe_{14}B$ Modified by Al, Ni, or Si, *Applied Sciences*, Vol. 8, 2018, Article No. 205.

[113] T. Wang, M. Medraj, Magnetic force microscopic study of $Ce_2(Fe, Co)_{14}B$, and its modifications by Ni and Cu, *Journal of Magnetism and Magnetic Materials*, Vol. 460, 2018, pp. 95-103.

[114] R. Grössinger, X. K. Sun, R. Eibler, K. H. J. Buschow, and H. R. Kirchmayr, The temperature dependence of the anisotropy field in $R_2Fe_{14}B$ compounds (R = Y, La, Ce, Pr, Nd, Gd, Ho, Lu), *Journal de Physique Colloques*, Vol. 46, No. C6, 1985, pp. 221-224.

[115] R. Grössinger, X. K. Sun, R. Eibler, K. H. J. Buschow, and H. R. Kirchmayr, Temperature dependence of anisotropy fields and initial susceptibilities in $R_2Fe_{14}B$ compounds, *Journal of Magnetism and Magnetic Materials,* Vol. 58, No. 1-2, 1986, pp. 55-60.

[116] M. Q. Huang, E. B. Boltich and W. E. Wallace, Magnetic characteristics of $R_2(Fe, Co)_{14}B$ systems (R=Y, Nd and Gd), *Journal of Magnetism and Magnetic Materials*, Vol. 60, 1986, pp. 270-274.

[117] N. M. Hong, N. P. Thuy and T. D. Hien, Anomalous anisotropy in the RCo_4B compounds, *Journal of Applied Physics*, Vol. 73, No. 10, 1993, pp. 5917-5919.

[118] J. F. Herbst, W. B. Yelon, Preferential site occupation and magnetic structure of $Nd_2(Co_xFe_{1-x})_{14}B$ systems, *Journal of Applied Physics*, Vol. 60, No. 12, 1986, pp. 4224-4229.

[119] V. L. Dominguez, J. M. Hernàndez, J. Tejada, and R. F. Ziolo, Colossal reduction in Curie temperature due to finite-size effects in $CoFe_2O_4$ nanoparticles, *Chemistry of Materials*, Vol. 25, No. 1, 2013, pp. 6-11.

[120] L. X. Liao, A. Altounian and D. H. Ryan, Co site preferences in iron rare-earth-based compounds, *Physical Review B*, Vol. 47, No. 17, 1993, pp. 11230-11241.

[121] S. V. Vonsovski, Magnetism, Nauka, Moscow, 1971.

[122] A. A. Lukin, S. Szymura, A. A. Zhuravlyev, S. M. Margaryan, Y. M. Rabinovich, The effect of less additives on magnetic properties and microstructure of sintered Nd-(Fe, Ti, Al)-B magnets, *Materials Chemistry and Physics*, Vol. 69, 2001, pp. 284-287.

[123] J. F. Herbst, J. J. Croat, F. E. Pinkerton and W. B. Yelon, Relationships between crystal structure and magnetic properties in $Nd_2Fe_{14}B$, *Physical Review B*, Vol. 29, No. 7, 1984, pp. 4176-4178.

[124] X. Fan, Y. Tang, Z. Shi, M. Jiang and B. Shen, The effect of Ni addition on microstructure and soft magnetic properties of FeCoZrBCu nanocrystalline alloys, *AIP Advances*, Vol. 7, 2017, pp. 056107-056114.

[125] S. Dai, A.H. Morrish and X.Z. Zhou, Mössbauer study of the permanent magnet material $Nd_2(Fe_{1-x}Ni_x)_{14}B$, *Journal of Applied Physics,* Vol. 63, 1988, pp. 3722–3724.

[126] A. R. Miedema, F. R. de Boer and R. Boom, Model predictions for the enthalpy of formation of transition metal alloys, *Calphad*, Vol. 1, 1977, pp. 341-359.

[127] M. Shimizu, J. Inoue and S. Nakagawa, Electronic structure and magnetic properties of Y-Ni intermetallic compounds, *Journal of Physics F: Metal Physics*, Vol. 14, 1984, pp. 2673-2687.

[128] B. D. Cullity, C. D. Graham, Introduction to magnetic materials, John Wiley & Sons, 2005.

[129] J. F. Herbst, C. D. Fuerst, R. K. Mishra, C. B. Murphy and D. J. Van Wingerden, Coercivity enhancement of melt-spun Nd-Fe-B ribbons using low-level Cu additions, *Journal of Applied Physics*, Vol. 69, No. 8, 1991, pp. 5823-5825.

[130] J. J. Wyslocki, F. Bolzoni, Magnetic domain structure and domain-wall energy in $Y_2Fe_{13}MnB$ and $Y_2Fe_{12}Mn_3B$ compounds, *Journal of Magnetism and Magnetic Materials*, Vol. 83, Issue 1, 1990, pp. 239-240.

[131] A. Hubert and R. Schafer: *Magnetic domains: The analysis of magnetic microstructures*, Springer-Verlag Berlin Heidelberg, Germany, 1998, pp. 201-315.

[132] L. Folks and R. C. Woodward, The use of MFM for investigating domain structures in modern permanent magnet materials, *Journal of Magnetism and Magnetic Materials*, Vol. 190, Issues 1–2, 1998, pp. 28-41.

[133] L. Batista, U. Rabe, S. Hirsekorn, Determination of the easy axes of small ferromagnetic precipitates in a bulk material by combined magnetic force microscopy and electron backscatter diffraction techniques, *Ultramicroscopy*, Vol. 146, 2014, pp. 17-46.

[134] B. Sun, G. Q. Li, W. X. Zhao, Z. Shen, Y. H. Liu and P. Chen, Perpendicular coercive force of thick CoFeB thin films grown on silicon substrate, *Materials Letters*, Vol. 123, 2014, pp. 221–223.

[135] C. Zhang, M. Yamanouchi, H. Sato, S. Fukami, S. Ikeda, F. Matsukura, and H. Ohno, Magnetization reversal induced by in-plane current in Ta/CoFeB/MgO structures with perpendicular magnetic easy axis, *Journal of Applied Physics,* Vol. 115, 2014, Article No. 17C714.

[136] R. D. Gomez, E. R. Bruke, I. D. Mayergoyz, Magnetic imaging in the presence of external fields: Technique and applications (invited), *Journal of Applied Physics*, Vol. 79, No. 8, 1996, pp. 6441-6446.

[137] X. A. Lin, C. J. Wei, T. L. Niu, W. F. Lin, Y. Zheng and H. B. Shan, Magnetic force microscopy study of alternate sputtered (001) oriented $L1_0$ phase FePt films, *Chinese Physics Letters*, Vol. 24, No. 1, 2007, pp. 222-225.

[138] Nanoscope Analysis, Bruker. Billerica, USA, Version: 1.4, 2011.

[139] I. Manke, N. Kardjilov, R. Schäfer, A. Hilger, M. Strobl, M. Dawson, C. Grünzweig, G. Behr, M. Hentschel, C. David, A. Kupsch, A. Lange and J. Banhart, Three-dimensional imaging of magnetic domains, *Nature Communications*, Vol. 1, 2010, Article No. 125.

[140] T. Wang, and M. Medraj, Intrinsic magnetic properties of $Ce_2(Fe, Co)_{14}B$ and modifications by Ni and Cu, *Journal of Alloys and Compounds*, submitted.

[141] N. León-Brito, E. D. Bauer, F. Ronning, J. D. Thompson, and R. Movshovich, Magnetic microstructure and magnetic properties of uniaxial itinerant ferromagnet Fe_3GeTe_2, *Journal of Applied Physics*, Vol. 120, 2016, pp. 080903-080908.

[142] W. Szmaja, Developments in the imaging of magnetic domains, *Advances in Imaging and Electron Physics*, Vol. 141, 2006, pp. 175-256.

[143] M. A. Al-Khafaji, W. M. Rainforth, M. R. J. Gibbs, J. E. L. Bishop, and H. A. Davies, The effect of tip type and scan height on magnetic domain images obtained by MFM, *IEEE Transactions on Magnetics*, Vol. 32, No. 5, 1996, pp. 4138–4140.
[144] M. M. Yazid, S. H. Olsen and G. J. Atkinson, MFM study of a sintered Nd-Fe-B magnet: Analyzing domain structure and measuring defect size in 3D view, *IEEE Transactions on Magnetics*, Vol. 52, No. 6, 2017, pp. 1-10.
[145] W. Szmaja, Investigations of the domain structure of anisotropic sintered Nd-Fe-B-based permanent magnets, *Journal of Magnetism and Magnetic Materials*, Vol. 301, 2006, pp. 546-561.
[146] R. Bodenberger and A. Hubert, Zur bestimmung der blochwandenergie von einachsigen ferromagneten, *Physica Status Solidi A*, Vol. 44, No. 1, 1977, pp. K7–K11.